S1-Global Report

Version 2012.08.15 (English proofreading done)

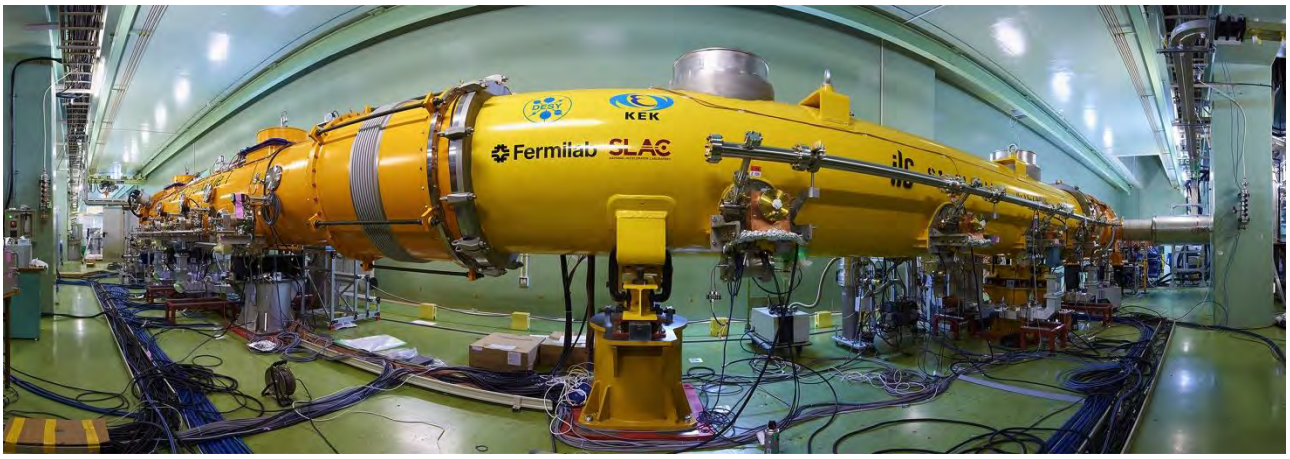

Authors

M. Akemoto, S. Fukuda, K. Hara, H. Hayano, N. Higashi, E. Kako, H. Katagiri, Y. Kojima, Y. Kondo, T. Matsumoto, S. Michizono, T. Miura, H. Nakai, H. Nakajima, K. Nakanishi, S. Noguchi, N. Ohuchi, T. Saeki, M. Satoh, T. Shidara, T. Shishido, T. Takenaka, A. Terashima, N. Toge, K. Tsuchiya, K. Watanabe, S. Yamaguchi, A. Yamamoto, Y. Yamamoto, K. Yokoya

KEK, Tsukuba, Japan

K. Jensch, D. Kostin, L. Lilje, A. Matheisen, W. -D. Moeller, M. Schmoekel, P. Schilling, N. Walker, H. Weise

DESY, Hamburg, Germany

T. Arkan, S. Barbanotti*, M. Battistoni, H. Carter, M. Champion, A. Hocker, R. Kephart, J. Kerby, D. Mitchell, Y. Pischalnikov, M. Ross, T. J. Peterson, W. Schappert, B. Smith

FNAL, Chicago, U.S.A

A. Bosotti, C. Pagani, R. Paparella, P. Pierini

INFN, Milano, Italy

C. Adolphsen, C. Nantista

SLAC, Menlo Park, U.S.A

* current affiliation: DESY

Contents

1 Preface

The S1-Global program was conceived in early 2008 with the aim of carrying out a string test of superconducting RF cavities during the Technical Design stage of the ILC (International Linear Collider) project. The proposal was to coordinate a collaboration involving various institutions around the world that would bring together eight 9-cell L-band cavities and associated hardware components, install them in common cryostat modules (cryomodules), and demonstrate their operation. This conceptual proposal received strong support from the GDE (Global Design Effort) and major laboratories throughout the world that partake in the GDE mission, and lead to the launch of a series of specific collaborative activities.

Two TESLA-type cavities with blade tuners were provided by Fermilab, two TESLA-type cavities with Saclay-tuners were provided by DESY, and four TESLA-like cavities with slide-jack tuners were provided by KEK. All of these cavities were industry-made by Zanon in Italy, ACCEL/RI in Germany, AES in the United States, and MHI in Japan. Prior to being brought together for assembly into cryomodules, each of these cavities had been individually cold-tested by the contributing laboratory.

The cryomodules were provided by KEK and INFN, who collaborated closely on all aspects of the design, engineering, and assembly. One-half of the cryomodule/cryostat was manufactured by Zanon and the other half by Hitachi in Japan.

Input-power couplers for the cavities were contributed by SLAC, DESY, and KEK. These were manufactured by CPI and Toshiba (Electron Tube). The RF waveguide components were provided by KEK and SLAC.

The S1-Global program was a world first in facilitating an international collaboration to build a segment of a superconducting linac system. The participating institutions contributed hardware and human resources equally and shared the experience of assembling a complex superconducting linac from components whose design and manufacture were coordinated remotely. While the S1-Global program did not involve beam operation, it involved all the essential steps required prior to beam acceleration in a superconducting linac. The program successfully addressed numerous critical issues such as the plug-compatibility of hardware components (i.e., that parts must be compatible but not necessarily identical), as well as single- and multiple-cavity operation with pulsed microwave power and associated LLRF controls.

We report here the progress of the S1-Global program and the results obtained thus far.

2 Introduction

GDE's R&D board, chaired by Bill Willis, launched an S-series task force in 2005 to assign the outstanding R&D tasks for the ILC [2-1]. The S1 program aims to complete one of the identified tasks, which is the demonstration of the RF operation of a cryomodule with an average accelerating gradient of 31.5 MV/m, as per the ILC specifications. The first cryomodule to fulfill the S1 aim was module-6 at DESY's FLASH. Eight cavities, which performed well in vertical tests, were selected for use in module-6. However, the performance of two out of the eight cavities degraded such that the accelerating gradient was limited to around 20 MV/m during the cryomodule test. In the meantime, CM-1 at FNAL and the Phase-1 half-cryostat at KEK's STF were under construction. These are the first attempts of the contributing laboratories to build cryomodules as a part of the global R&D for the ILC.

Concurrently to these efforts, the concept of plug-compatibility was discussed with regard to the construction of the ILC. In rough terms, plug-compatibility at the ILC means the enforcement of a set of sufficiently specific guidelines for mechanical, electrical, and other interface conditions for each of the components in the main linac systems for the ILC. However, these specifications do not reach the level of the design of the individual component or its manufacturing process. This is to encourage the participating institutions to pursue a cooperative yet creative and competitive development process for high-performance and cost-effective components, while ensuring fault-free integration of the components in the final assembly of the main linac systems.

The S1-Global cryomodule was conceptualized in this context to address two issues: first, the construction of a cryomodule that demonstrates ILC-grade performance, particularly in terms of the accelerating gradient, and second, to achieve this through an international collaboration whose members contribute hardware components and are coordinated remotely. Thus, the GDE's project managers submitted a formal proposal for the construction of the S1-Global cryomodules, and after some discussion, the proposal was approved as an international collaborative effort at the SC-RF technical meeting of the ILC GDE in Apr. 2008. The STF site at KEK was selected as the host site in order to take advantage of a one-year time slot that was found available between the phase-1 and phase-2 efforts at the STF. The eight cavities were contributed from FNAL, DESY, and KEK, and were installed in two "half-length cryomodules," which were each 6 m long. For this purpose, a new half-length cryomodule (Module-C) was designed and prepared by INFN, whereas the other half of the cryomodule (Module-A) was built by modifying an existing 6-m STF cryomodule at KEK.

The major contributions from the participating institutes in the S1-Global experiment are summarized as follows.

- INFN: Design and construction of Module-C and production of the INFN blade tuners for the FNAL cavities. Assembly work of tuners, magnetic shield, and testing of tuners.
- FNAL: Two TESLA-type cavities [5] and TTF-III power couplers. Integration and installation of the power couplers, cavity connection, INFN blade tuners, and the magnetic shields.
- DESY: Two TESLA-type cavities, together with Saclay-type tuners, and TTF-III power couplers. Integration and installation of the power couplers, cavity connection, and RF processing of the power couplers and cavities.
- SLAC: Two sets of variable tap-offs (VTOs) to use in the RF power distribution for Module-C, and RF processing of the FNAL couplers.

- KEK: Four TESLA-like cavities and power couplers, which were integrated with two types of slide-jack tuners, and the assembly of these components into Module-A [6]. The RF power distribution for Module-A. Infrastructure for the S1-Global experiment, in general. The remaining assembly work, cool-down, and various other RF testing activities were coordinated or conducted by KEK.

A biweekly WebEx meeting was organized for discussion of the specific technical details and activity schedule for the S1-Global experiment. The meeting was chaired by Norihito Ohuchi from 2008 to 2010 and by Hitoshi Hayano in 2011. In addition, several face-to-face meetings were held, and these were typically arranged in order to take advantage of opportunities around the biannual meetings of the GDE and the TESLA Technology Collaboration (TTC).

Table 2-1: Chronology of S1-Global experiment.

Date	Event
4 Dec, 2009	Delivery of two DESY cavities at KEK.
25 Dec, 2009	Delivery of two FNAL cavities at KEK.
8 Jan, 2010	
Jan–Mar, 2010	Cavity stringing of DESY and FNAL cavities by members of the groups at DESY, FNAL, and INFN for Cryomodule C.
Mar, 2010	Installation of Cryomodule C into the STF tunnel.
Mar–May, 2010	Cavity stringing of KEK cavities by members of the group at KEK for Cryomodule A.
May, 2010	Installation of Cryomodule A into the STF tunnel. Connection of Cryomodules A and C.
6 Jun–23 Jul, 2010	Performance of first cool-down test. Low power test of cavities, cold-test of tuners, and measurement of static heat load.
6 Sep–24 Dec, 2010	Performance of second cool-down test. High-power test of cavities. Test of compensation of Lorentz-force detuning (LFD). LLRF test of vector-sum field control. Measurement of dynamic heat load.
17 Jan–25 Feb, 2011	Testing of the distributed RF scheme (DRFS) with S1-Global cavities.
Late Apr, 2011	Commencement of disassembly of S1-Global cryomodules.
Jun, 2011	Removal of Cryomodules A and C from the STF tunnel.
	Disassembly of the cold mass for Cryomodule A.
Dec, 2011	Disassembly of the cold mass for Cryomodule C. Components were shipped back to their parent institutions (DESY and FNAL).

Table 2-1 summarizes the chronology of the S1-Global experiment. While the cool-down tests were all completed by the end of Feb. 2011, disassembly of the S1-Global cryomodules was delayed until the end of April due to the impact of the 2011 Tohoku earthquake. However, toward the end of 2011, most of the contributed cavity components had been returned to their parent institutions for post-mortem diagnosis studies.

3 Cavities

3.1 Introduction

The S1-Global Activity included eight TESLA-shape cavities. Four of these were from KEK, two were from DESY, and two were from FNAL. These were procured, processed, and cold-tested at each lab before the FNAL and DESY cavities were shipped to KEK in Nov. and Dec. of 2009 for assembly into Cryomodule-C. The four KEK cavities were tested from Dec. 2008 to Dec. 2009, and the assembly of Cryomodule-A was commenced in Mar. 2010. The location, responsible laboratory, manufacturer, serial number, and process or test location of each cavity in the assembly is listed in Table 3-1. The history of each cavity before assembly into S1-Global is described in the following sections.

Table 3-1: Summary of the eight cavities used for the S1-Global experiment.

S1-G Position	Responsible Laboratory	Serial Number	Manufacturer	Process/Test Laboratory
C1	FNAL	TB9AES004	AES	JLab/FNAL
C2	FNAL	TB9ACC011	Accel (RI)	JLab/FNAL
C3	DESY	Z108	Zanon	DESY
C4	DESY	Z109	Zanon	DESY
A1	KEK	MHI05	MHI	KEK
A2	KEK	MHI06	MHI	KEK
A3	KEK	MHI07	MHI	KEK
A4	KEK	MHI09	MHI	KEK

3.2 DESY Cavities

The S1-Global module contains two DESY cavities, i.e., C3 – Z108 and C4 – Z109. Both the cavities were manufactured by Zanon in 2005 using Tokyo Denkai niobium ingot N21. Further, both the cavities were processed using EP treatment at DESY and were previously installed in module 8 and tested on the CMTB at DESY. Before shipment to KEK, Z108 and Z109 underwent six HPR cycles and were tested in the DESY vertical cryostat. Full treatment and test histories of the cavities are presented below. The cavities are equipped with TTF-III-type main input couplers, made by CPI, and Saclay-type cavity tuners.

3.2.1 Cavity and Coupler Parts

The DESY cavities and coupler parts installed in the S1-Global module are listed in Table 3-2. A completed DESY 9-cell cavity is shown in Figure 3-1, and a 3D view of one DESY unit consisting of a cavity, a tuner, and an input coupler is shown in Figure 3-2. After the cavities were removed from module 8, new TTF-III input couplers were installed. One of the couplers, i.e., CP3C12, was pre-conditioned at DESY, while the other, CP3C70, was pre-conditioned at LAL-Orsay. No problems were encountered during the preconditioning. The Z108 and Z109 cavities contain Saclay-type tuners.

Table 3-2: Parts supplied by DESY for the S1-Global Module.

S1-Global Position	Cavity	Coupler: Cold	Coupler: Warm	Coupler: Wave Guide	Tuner Style
C3	Z108	CP3C70	CP3H61	CP3W61	Saclay
C4	Z109	CP3C12	CP3H60	CP3W59	Saclay

Figure 3-1: A DESY 9-cell cavity.

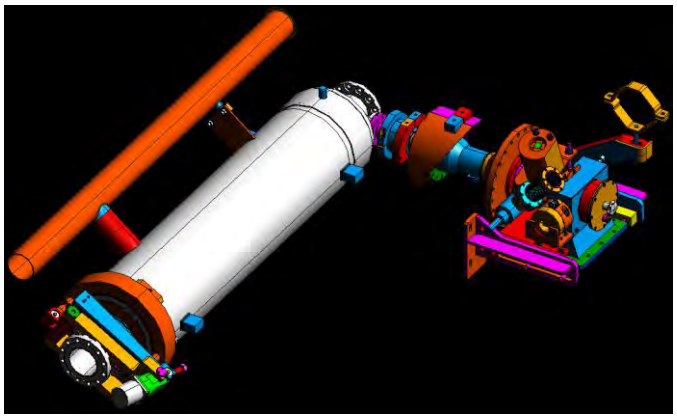

Figure 3-2: A single DESY unit consisting of a cavity, a tuner, and an input coupler.

3.2.2 History of DESY Cavities

The history of the Z108 and Z09 cavities is summarized in Tables 3-3 and 3-4, respectively, including dates, preparations, treatments, tests, and key results (see DESY TESLA Cavity Database for further details). Both the cavities were electropolished at DESY (144 μm removal), and heat treated at 800 °C for 2 h; however, the specific processes and number of vertical tests prior to installation in module 8 differed for each cavity. With reference to the last vertical test, the performance of both the cavities degraded in module 8 (see Figure 3-3). After removal from module 8, both the cavities received 6 HPR cycles, were vertically tested to confirm the restoration of performance, and received an additional six HPR cycles. No horizontal pulsed RF test (single cavity) was carried out on either cavity. The Z108 and Z109 cavities were sent to KEK, while placed in a horizontal position with the attached coupler in upper vertical during transport, for S1-Global module string assembly, with the input coupler's cold section mounted.

Table 3-3: History of Cavity Z108.

Date	Step/Treatment/Test
30.11.2005	Cavity production date, Zanon.
24.10.2006	144 μm EP at DESY
02.11.2006	Alcohol rinsing
07.11.2006	HT 800 C, 2 h.
07.12.2006	48 μm End-EP at DESY (after tuning)
13.12.2006	HPR, alcohol rinsing, 6×HPR
09.01.2007	VT: E_{acc} = 23.0 MV/m, $Q_0 = 1.6\times10^{10}$, no FE
18.01.2007	VT: E_{acc} = 23.2 MV/m, $Q_0 = 1.6\times10^{10}$, no FE
06.06.2007	48 μm End-EP at DESY (after tuning)
13.06.2007	HPR, alcohol rinsing, 6×HPR
22.06.2007	126 °C Baking, 48 h.
11.07.2007	VT: E_{acc} = 33.0 MV/m, $Q_0 = 1.2\times10^{10}$, no FE
18.07.2007	HPR
13.08.2007	EB welding of rings, tuning
12.09.2007	10×HPR
06.11.2007	Cavity is mounted in the module 8 string, pos.3
10.07.2008	Module 8 test on CMTB: E_{acc} = 25.7 MV/m
17.06.2009	6×HPR (after disassembly from module 8)
25.06.2009	VT: E_{acc} = 31.3 MV/m, $Q_0 = 1.1\times10^{10}$, no FE
08.07.2009	6×HPR (before transport to KEK)
04.12.2009	Cavity delivered to KEK
19.01.2010	S1-Global string assembly of cavity
30.09.2010	S1-Global module test at STF/KEK: E_{acc} = 19.5 MV/m

Table 3-4: History of Cavity Z109.

Date	Step/Treatment/Test
29.12.2005	Cavity production date, Zanon.
07.06.2006	144 μm EP at DESY
21.06.2006	HT 800 °C, 2 h.
03.07.2006	Flash BCP (Nb) 10 μm + HPR (after tuning)
13.07.2006	6×HPR
20.07.2006	VT: E_{acc} = 27.5 MV/m, $Q_0 = 5.5\times10^9$, FE
01.08.2006	120 °C Baking, 48 h.
11.08.2006	VT: E_{acc} = 26.7 MV/m, $Q_0 = 8.3\times10^9$, FE
21.08.2006	Alcohol rinsing (no End-EP)
22.08.2006	6×HPR
27.09.2006	Flash BCP (Nb) 5 μm
04.10.2006	6×HPR
13.10.2006	VT: E_{acc} = 29.2 MV/m, $Q_0 = 6.0\times10^9$, low FE
23.10.2006	120 °C Baking, 48 h.
15.11.2006	3×HPR (after leak in vertical test)
30.11.2006	VT: E_{acc} = 20.0 MV/m, $Q_0 = 1.7\times10^{10}$, FE
23.04.2007	48 μm End-EP at DESY (final EP)
25.04.2007	HPR, alcohol rinsing, 6×HPR
04.05.2007	122°C Baking, 48 h.
23.05.2007	VT: E_{acc} = 30.1 MV/m, $Q_0 = 1.2\times10^{10}$, no FE
04.06.2007	HPR
18.06.2007	EB welding of rings, tuning
04.07.2007	Tank welding
24.07.2007	6×HPR
06.11.2007	Cavity mounted in the module 8 string, pos.2
10.07.2008	Module 8 test on CMTB: E_{acc} = 21.8 MV/m
14.07.2009	6×HPR (after disassembly from module 8)
03.08.2009	VT: E_{acc} = 30.7 MV/m, $Q_0 = 1.3\times10^{10}$, low FE
05.11.2009	6×HPR (before transport to KEK)
04.12.2009	Cavity delivered to KEK
19.01.2010	S1-Global string assembly for cavity
01.10.2010	S1-Global module test at STF/KEK: E_{acc} = 29.5 MV/m

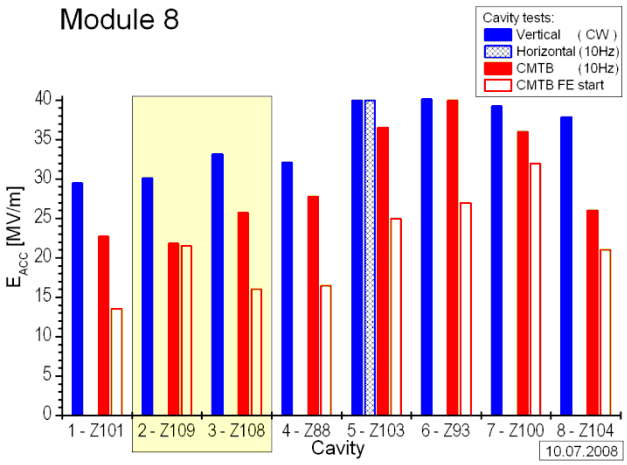

Figure 3-3: Maximum accelerating gradient obtained in Module 8.

3.2.3 Vertical Test Data

After being disassembled from module 8 and undergoing six HPR cycles, Z108 and Z109 were tested in the vertical cryostat at DESY and the results are shown in Figure 3-4. The data recorded during the CW tests showed second 7/9π mode generation for both the cavities.

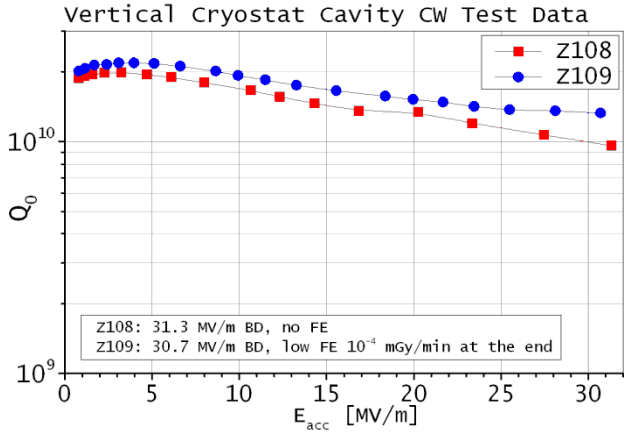

Figure 3-4: Last vertical test data for cavities Z108 and Z109.

3.3 FNAL Cavities

S1-Global Module-C contains two FNAL cavities, i.e., C1 – TB9AES004 and C2 – TB9ACC011. Cavity TB9AES004 was fabricated by Advanced Energy Systems (AES) in USA and cavity TB9ACC011 was fabricated by ACCEL (now Research Instruments) in Germany. TB9AES004 was last tested in a horizontal test stand at FNAL before shipment, and TB9ACC011 was last tested in a vertical test stand. The complete fabrication process and test history for each cavity is presented below. Both the cavities are equipped with TTF-III-type main input couplers, made by CPI, and INFN design blade tuners.

3.3.1 Cavity and Coupler Parts

The FNAL cavities and coupler parts installed in the S1-Global module are listed in Table 3-5. A completed FNAL 9-cell cavity is shown in Figure 3-5, and a 3D view of one FNAL unit consisting of a cavity, a tuner, and an input coupler is shown in Figure 3-6. Both the TTF-III input couplers were pre-conditioned at SLAC without any problems before assembly into the cavities. In addition to these main parts, FNAL supplied various interconnecting bellows, magnetic shielding bridge parts, and pipe adapters.

Table 3-5: Parts for S1-Global module provided by FNAL.

S1-Global Position	Cavity	Coupler: Cold	Coupler: Warm	Tuner Style
C1	TB9AES004	FC08	FH08	Blade-INFN
C2	TB9ACC011	FC02	FH10	Blade-INFN

Figure 3-5: FNAL 9-cell cavity.

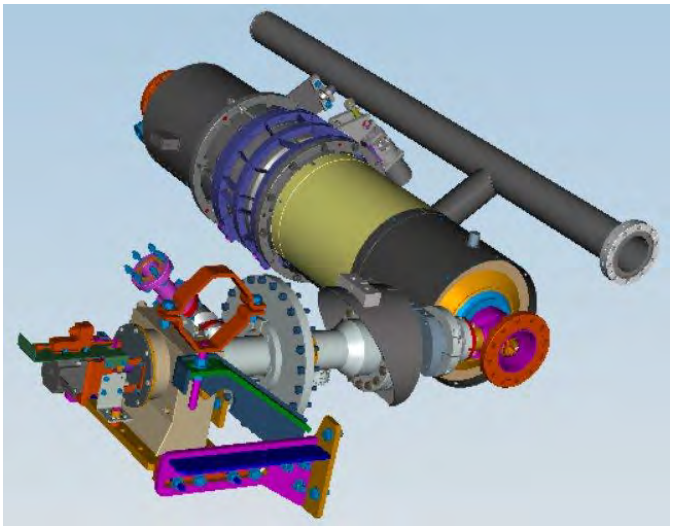

Figure 3-6: One FNAL unit consisting of a cavity, a tuner, and an input coupler.

3.3.2 History of FNAL Cavities

The histories of the TB9AES004 and TB9ACC011 cavities are presented with dates, preparatory activities, treatments, tests, and key results in Tables 3-6 and 3-7 (see FNAL Cavity Database for more details). The TB9AES004 cavity underwent several EP and vertical test cycles at JLAB before shipment to Fermilab, where it was the first cavity to be rinsed in the new HPR system at ANL, and it was in use during the commissioning of this ANL facility in 2008. In 2009, TB9AES004 was welded into the helium vessel and received a final HPR at ANL. It was successfully tested in the Fermilab Horizontal Test Facility, and then packaged and shipped to

KEK in Dec. 2009. TB9ACC011 was also initially processed at JLab, which involved a single EP and vertical test cycle before shipment to Fermilab. Upon receipt at Fermilab, the cavity was vertically tested, and the result showed a degradation in performance. After an HPR cycle at ANL, the cavity was restored to its original performance, as confirmed by a retest at Fermilab, and it was then shipped to KEK. Both the cavities were sent to KEK for the S1-Global module C string assembly with the input coupler cold part mounted; they were transported in a horizontal position with the attached coupler in upper vertical and the beam line was under vacuum.

Table 3-6: History of Cavity TB9AES004.

Date	Step/Treatment/Test
Mar. 2007	Cavity transported from AES to FNAL
	221 μm EP at JLAB
12.07.2007	VT: E_{acc} = 28.0 MV/m, FE limited, tested at JLAB
	257 μm (total) EP at JLAB
7.08.2007	VT: E_{acc} = 25.5 MV/m, cable limited with FE, tested at JLAB
	277 μm (total) EP at JLAB
21.08.2007	VT: E_{acc} = 19.5 MV/m, FE limited, tested at JLAB
	EP at JLAB
19.09.2007	VT: E_{acc} = 21.5 MV/m, cable limited with FE, tested at JLAB
25.03.2008	VT: E_{acc} = 27.0 MV/m, FE limited, tested at JLAB
24.11.2008	Cavity sent to FNAL from JLAB
3.12.2008	Cavity sent to ANL for HPR system commissioning
28.12.2008	Cavity returned to FNAL
Apr. 2009	RF measurements at FNAL
14.7.2009	Cavity welded with its helium vessel
15.10.2009	Cavity at ANL for post helium vessel welding HPR
19.12.2009	Horizontal test of cavity at HTS: 25-31 MV/m, quench limitation, FE observed
23.12.2009	Cavity is shipped to KEK
19.01.2010	S1-Global string assembly for cavity
30.09.2010	S1-Global module test at STF/KEK: E_{acc} = 27.0 MV/m

Table 3-7: History of Cavity TB9ACC011.

Date	Step/Treatment/Test
May 2008	Cavity transported from ACCEL to FNAL
Oct. 2008	Processing and vertical test at JLAB
21.10.2008	VT: E_{acc} = 38.0 MV/m, tested at JLAB
May 2009	Cavity is sent to FNAL from JLAB
15.10.2009	Cavity is welded with its helium vessel
28.10.2009	Cavity is transported to ANL for post helium vessel welding HPR
9.11.2009	Cavity is delivered to vertical test facility at FNAL
13.11.2009	VT: E_{acc} = 23.0 MV/m, tested at FNAL
16.11.2009	Cavity is transported to ANL for HPR
23.11.2009	Cavity is delivered to vertical test facility at FNAL
24.11.2009	VT: E_{acc} = 33.0 MV/m, FE induced quench limited, tested at FNAL
16.12.2009	Cavity shipped to KEK
19.01.2010	S1-Global string assembly for cavity
01.10.2010	S1-Global module test at STF/KEK: E_{acc} = 24 MV/m

3.3.3 Vertical Test Result

The last test of the TB9ACC011 cavity was performed by placing the cavity in a vertical test stand at FNAL, and the results of this test are shown in Figure 3-7.

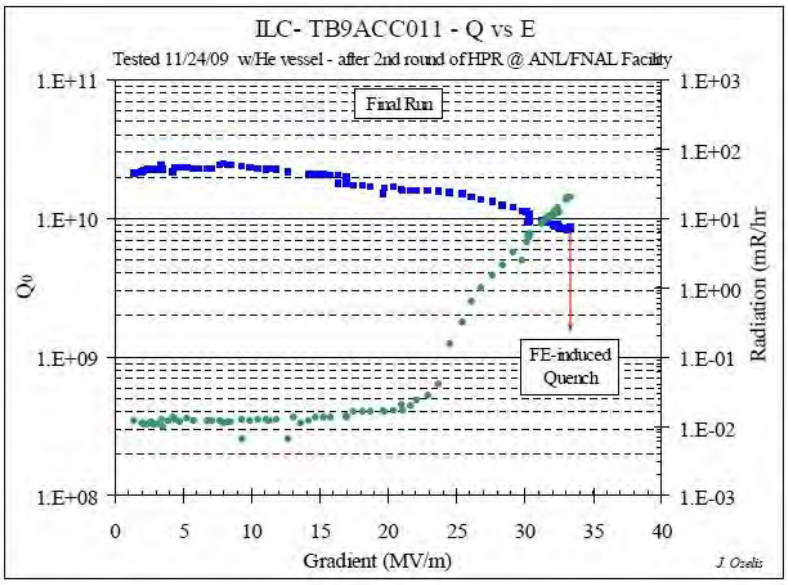

Figure 3-7: Last vertical test data for cavity TB9ACC-011. Blue squares show Q0 vs. gradient, and green dots show emitted radiation vs. gradient.

3.3.4 Horizontal Test Data

The last test of the TB9AES004 cavity was performed by placing the cavity in a horizontal test stand at FNAL, and the results of this test are presented below.

ILCTA_MDB HTS Test Report: TB9AES004

A. Hocker
15-JAN-2010

DATES:

Cavity installed in cryostat: **18-NOV-2009**
Cooldown begun: **24-NOV-2009**
Warmup begun: **17-DEC-2009**
Cavity removed from cryostat: **19-DEC-2009**

CAVITY PERFORMANCE:

Test temperature (pressure): **2 K (23 Torr)**
Test rep rate: **5 Hz**
Maximum accelerating gradient: **31 MV/m (see note 1)**
Gradient limitation (quench, FE, …): **quench**
Q_0 at maximum gradient: **N/A (see note 6)**

WARM COUPLER CONDITIONING:

Maximum klystron power: **265 kW**
Conditioning rep rate: **2 Hz**

Pulse length (μs)	Time (min)
20	1020
50	210
100	261
200	345
400	350
800	608
1300	210

3.4 KEK Cavities

The S1-Global Module A has four cavities supplied by KEK in the positions A1–A4. The cavities were fabricated by Mitsubishi Heavy Industries (MHI) and labeled as MHI05, MHI06, MHI07, and MHI09. Although these cavities are derived from the TESLA-type cavity shape, thick titanium endplates have been introduced into the design in order to increase the cavity stiffness, as shown in Figure 3-8. Compared to the cavities in Cryomodule C, these cavities also have an increased beam pipe diameter, an enlarged input port diameter, magnetic shielding inside the helium vessel as opposed to outside, a re-optimized cell shape that decreases the ratio of the surface peak magnetic field to the accelerating field, and an STF-2-type input coupler that exhibits overcoupling. The main cavity parameters of the TESLA cavity and the TESLA-like cavities are compared in Table 3-8. Each cavity was processed and tested at KEK as described below. Two types of tuners were utilized, i.e., central slide-jack tuners on MHI05 and MHI06, and lateral slide-jack tuners on MHI07 and MHI09. The couplers for each cavity were produced by Toshiba, and pre-conditioned at KEK for up to 1.0 MW with pulsed operation using a 1.5 ms pulse width at 5 Hz.

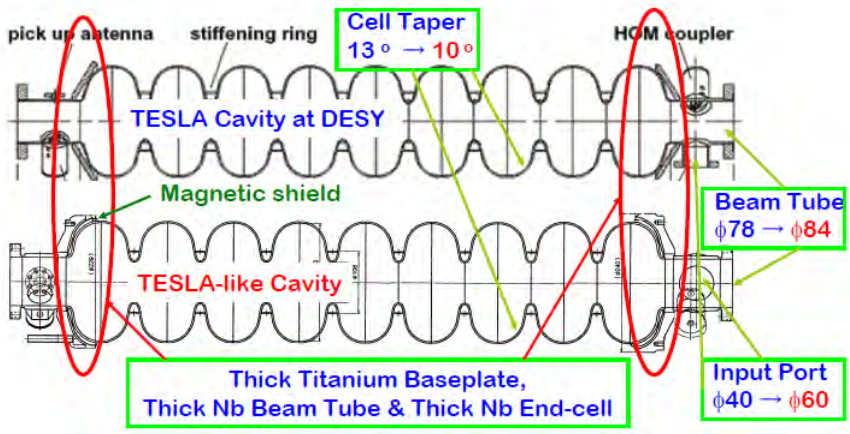

Figure 3-8: Comparison of the shape of the TESLA cavities developed at DESY and the TESLA-like cavities developed at KEK.

Table 3-8: Comparison of main cavity parameters.

Cavity Parameter	TESLA cavity from DESY	TESLA-like cavity from KEK
Cell Taper	76.7°	80.0°
Diameter of Beam Tube	78 mm	84 mm
Diameter of Input Port	40 mm	60 mm
Esp/Eacc	1.98	2.17
Hsp/Eacc	42.6 Oe/MV/m	41.0 Oe/MV/m
R/Q	1036 Ω	1016 Ω
Input Coupling	3.0×10^6	2.0×10^6
Stiffness of Support System	22 kN/mm	72 kN/mm
Estimated Lorentz Detuning at 31.5 MV/m	–500 Hz in a flat-top	–150 Hz in a flat-top

3.4.1 Cavity and Coupler Parts

The KEK cavity, coupler, and tuner parts installed in the S1-Global module are listed in Table 3-9. A completed 9-cell cavity from KEK is shown in Figure 3-9, and four of the cavities fabricated at KEK and covered with a titanium helium jacket are shown in Figure 3-10. In addition to these major parts, KEK supplied all interconnecting bellows, shielding, and assorted pieces of piping to complete the string assembly of cryomodule A.

Table 3-9: Parts for S1-Global module supplied by KEK.

S1-Global Position	Cavity	Coupler: Cold	Coupler: Warm	Tuner Style
A1	MHI05	TCO-4	TWA-8	Central slide-jack
A2	MHI06	TCO-3	TWA-7	Central slide-jack
A3	MHI07	TCO-2	TWA-6	Lateral slide-jack
A4	MHI09	TCO-1	TWA-5	Lateral slide-jack

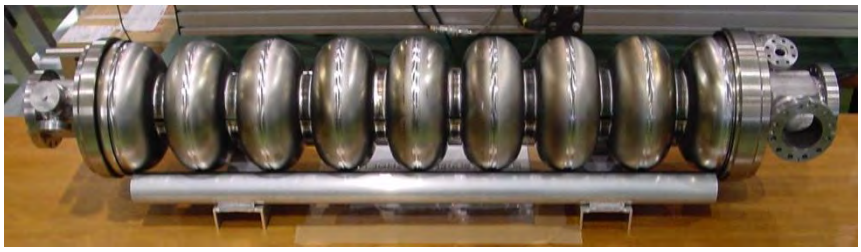

Figure 3-9: 9-cell cavity supplied by KEK.

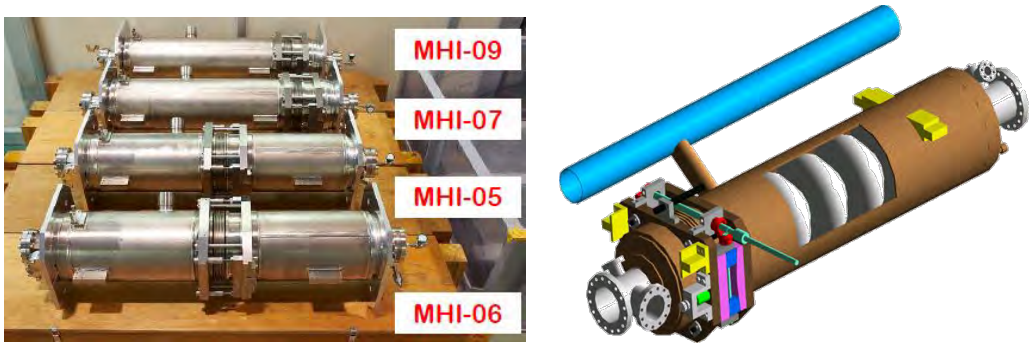

Figure 3-10: Four cavities supplied by KEK covered with a Ti-He jacket.

3.4.2 History of KEK Cavities

All processing and vertical test qualification tasks were carried out at KEK-STF. The facilities of STF were newly designed for SC cavity development activities. Typical surface treatments at STF used for vertical tests are summarized in Figure 3-11. The history of each cavity, including dates, preparations, treatments, tests, and key results is given in Tables 3-10, 3-11, 3-12, and 3-13 for cavities MHI-05, MHI-06, MHI-07, and MHI-09, respectively.

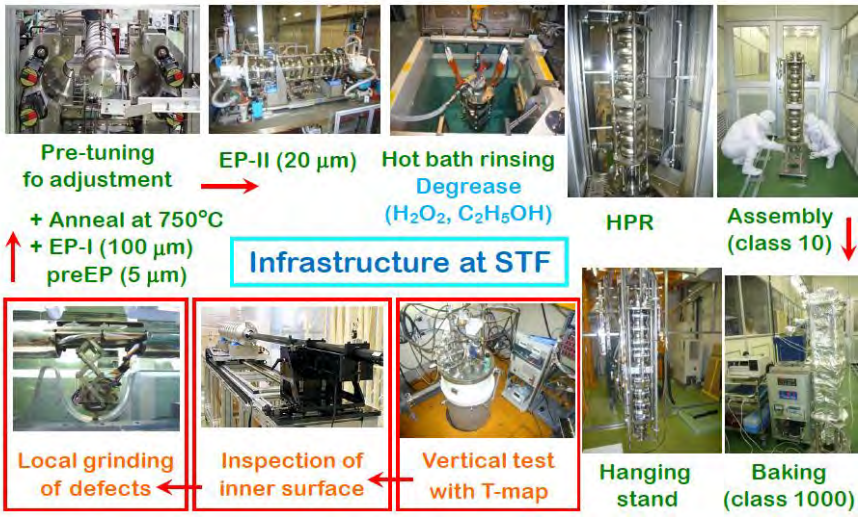

Figure 3-11: Surface preparation procedure used at STF for cavities supplied by KEK.

Table 3-10: History of Cavity MHI-05.

Date	Step/Treatment/Test
17.04.2008	Cavity production date, MHI.
12.06.2008	Acceptance test, f_o = 1298.3 MHz, flatness = 69%
27.08.2008	Pre-EP: 5 μm, EP-1: 100 μm
24.09.2008	Anneal at 750 ^oC for 3 h.
11.11.2008	Pre-tuning, f_o = 1297.4 MHz, flatness = 98%
26.11.2008	EP-2: 50 μm, H_2O_2 rinse, Hot rinse, HPR for 8.5 h.
30.11.2008	100 °C Baking, 64 h.
04.12.2008	1st VT: E_{acc} = 27.3 MV/m, $Q_0 = 3.7\times10^9$, Quench
14.01.2009	Pre-tuning, f_o = 1297.1 MHz, flatness = 98%
18.02.2009	EP-2: 50 μm, H_2O_2 rinse, Hot rinse, HPR for 9 h.
21.02.2009	100 °C Baking, 48 h.
26.02.2009	2nd VT: E_{acc} = 19.7 MV/m, $Q_0 = 1.2\times10^{10}$, Quench
01.04.2009	Pre-tuning, f_o = 1297.3 MHz, flatness = 97%
08.04.2009	EP-2: 20 μm, Ethanol rinse, Water rinse, HPR for 9 h.
11.04.2009	100 °C Baking, 48 h.
16.04.2009	3rd VT: E_{acc} = 27.1 MV/m, $Q_0 = 7.5\times10^9$, Quench
22.01.2010	He Jacket welding at MHI
16.02.2010	Cavity delivered to KEK
01.03.2010	S1-Global string assembly of cavity
19.10.2010	S1-Global module test at STF/KEK: E_{acc} = 28.5 MV/m

Table 3-11: History of Cavity MHI-06.

Date	Step/Treatment/Test
17.04.2008	Cavity production date, MHI.
12.06.2008	Acceptance test, f_o = 1298.5 MHz, flatness = 49%
29.08.2008	Pre-EP: 5 μm, EP-1: 100 μm
29.09.2008	Anneal at 750 ^{o}C for 3 h.
11.11.2008	Pre-tuning, f_o = 1297.3 MHz, flatness = 98%
10.12.2008	EP-2: 50 μm, H_2O_2 rinse, Hot rinse, HPR for 8.5 h.
13.12.2008	100 °C Baking, 42 h.
18.12.2008	1st VT: E_{acc} = 25.7 MV/m, $Q_0 = 4.6\times10^9$, Quench +FE
15.01.2009	Removal of cryostat magnetic shield, Mount of cavity magnetic shield
22.01.2009	2nd VT: E_{acc} = 24.6 MV/m, $Q_0 = 5.1\times10^9$, Quench +FE
02.02.2009	Installation of cryostat magnetic shield, Mount of cavity magnetic shield
05.02.2009	3 rd VT: E_{acc} = 25.9 MV/m, $Q_0 = 7.5\times10^9$, Quench +FE
25.02.2009	Pre-tuning, f_o = 1297.1 MHz, flatness = 98%
04.03.2009	EP-2: 50 μm, H_2O_2 rinse, Hot rinse, HPR for 9 h.
07.03.2009	100 °C Baking, 45 h.
12.03.2009	4th VT: E_{acc} = 19.6 MV/m, $Q_0 = 9.1\times10^9$, Quench
21.05.2009	Pre-tuning, f_o = 1297.4 MHz, flatness = 98%
29.05.2008	EP-2: 20 μm, Ethanol rinse, Hot rinse, HPR for 8 h.
30.05.2009	100 °C Baking, 48 h.
04.06.2009	5th VT: E_{acc} = 22.1 MV/m, $Q_0 = 8.3\times10^9$, FE
22.06.2009	Pre-tuning, f_o = 1297.2 MHz, flatness = 98%
09.09.2009	EP-2: 20 μm, Ethanol rinse, Hot rinse, HPR for 18 h.
12.09.2009	100 °C Baking, 48 h.
16.09.2009	6th VT: E_{acc} = 27.7 MV/m, $Q_0 = 5.0\times10^9$, Quench +FE
22.01.2010	He Jacket welding at MHI
16.02.2010	Cavity delivered to KEK
01.03.2010	S1-Global string assembly of cavity
13.10.2010	S1-Global module test at STF/KEK: E_{acc} = 37.7 MV/m

Table 3-12: History of Cavity MHI-07.

Date	Step/Treatment/Test
24.03.2009	Cavity production date, MHI.
07.04.2009	Acceptance test, f_o = 1296.3 MHz, flatness = 80%
16.04.2009	Pre-EP: 5 μm, EP-1: 100 μm
21.04.2009	Anneal at 750 ^{o}C for 3 h.
03.06.2009	Pre-tuning, f_o = 1297.4 MHz, flatness = 97%
10.06.2009	EP-2: 20 μm, Ethanol rinse, Hot rinse, HPR for 8 h.
13.06.2009	100 °C Baking, 48 h.
25.06.2009	1st VT: E_{acc} = 16.5 MV/m, $Q_0 = 2.4\times10^9$, FE
07.07.2009	Pre-tuning, f_o = 1297.2 MHz, flatness = 96%
07.10.2009	EP-2: 20 μm, FM20 degrease, Hot rinse, HPR for 9 h.
10.10.2009	100 °C Baking, 48 h.
15.10.2009	2nd VT: E_{acc} = 33.6 MV/m, $Q_0 = 4.8\times10^9$, Quench +FE
29.01.2010	He Jacket welding at MHI
16.02.2010	Cavity delivered to KEK
01.03.2010	S1-Global string assembly of cavity
15.10.2010	S1-Global module test at STF/KEK: E_{acc} = 31.8 MV/m

Table 3-13: History of Cavity MHI-09.

Date	Step/Treatment/Test
24.03.2009	Cavity production date, MHI.
08.04.2009	Acceptance test, f_o = 1295.8 MHz, flatness = 72%
30.04.2009	Pre-EP: 5 μm, EP-1: 100 μm
11.05.2009	Anneal at 750 ^{o}C for 3 h.
07.07.2009	Pre-tuning, f_o = 1297.3 MHz, flatness = 98%
26.08.2009	EP-2: 20 μm, Ethanol rinse, Hot rinse, HPR for 16 h.
29.08.2009	100 °C Baking, 48 h.
03.09.2009	1st VT: E_{acc} = 25.0 MV/m, $Q_0 = 6.5\times10^9$, Quench
21.10.2009	Pre-tuning, f_o = 1297.2 MHz, flatness = 98%
05.11.2009	EP-2: 20 μm, FM20 degrease, Hot rinse, HPR for 9 h.
08.11.2009	100 °C Baking, 48 h.
12.11.2009	2nd VT: E_{acc} = 15.9 MV/m, $Q_0 = 1.3\times10^{10}$, Quench
27.11.2009	Pre-tuning, f_o = 1297.3 MHz, flatness = 98%
09.12.2009	EP-2: 20 μm, FM20 degrease, Hot rinse, HPR for 9 h.
12.12.2009	100 °C Baking, 48 h.
16.04.2009	3rd VT: E_{acc} = 27.0 MV/m, $Q_0 = 4.0\times10^9$, Quench +FE
29.01.2010	He Jacket welding at MHI
16.02.2010	Cavity delivered to KEK
01.03.2010	S1-Global string assembly of cavity
20.10.2010	S1-Global module test at STF/KEK: E_{acc} = 23.5 MV/m

3.4.3 Vertical Test Results

A total of 14 vertical tests were carried out at STF for the four cavities supplied by KEK, and the maximum accelerating gradients (Eacc,max) obtained during the tests are summarized in Figure 3-12. The final performance of these four cavities, which were selected to be installed into the S1-Global cryomodule, is shown in Figure 3-13. The average Eacc,max achieved by the four cavities was 28.9 MV/m. The Q_o values at high field gradient (>20 MV/m) showed a steep drop due to field emission, and the radiation levels of X-rays were also strong, (The upper detection limitation of the X-ray sensor is 100 mSv/h). After the performance qualification, the four cavities were covered with a magnetic shield and joined with a titanium and helium jacket by TIG-welding (see Figure 3-10).

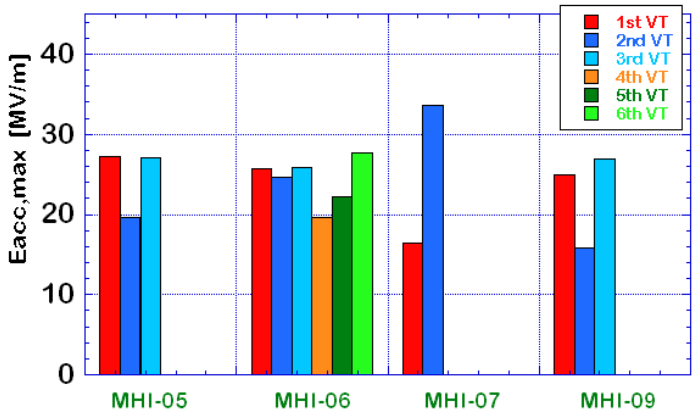

Figure 3-12: Summary of vertical test results of the four cavities supplied by KEK.

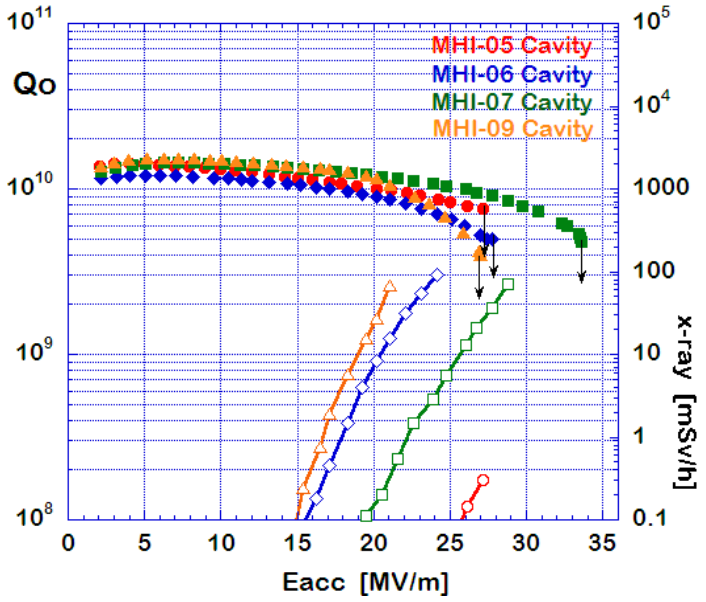

Figure 3-13: Final operating performance of the four cavities supplied by KEK.

4 Couplers

4.1 Introduction

Four TTF-III input couplers developed at DESY were installed in the two DESY and two FNAL cavities. Four STF-2 input couplers developed at KEK were installed in the four KEK cavities. Specifications of the input couplers are listed in Table 4-1. Both the TTF-III and STF-2 input couplers have a variable coupling to the 9-cell cavity.

Table 4-1: Main specifications of input couplers.

Frequency	1.3 GHz
Pulse width	1.5 ms
Repetition rate	5 Hz
Beam current	9 mA
Accelerating gradient	31.5 MV/m
Required RF power	350 kW
Range of external Q value	2 – 10. x 10^6 (TTF-III)
	2 - 4 x 10^6 (STF-2)

4.2 TTF-III Input Couplers

4.2.1 Coupler Design

Both the warm and cold RF windows consist of ceramic cylinders made of Al_2O_3. The vacuum surface of the ceramic windows was coated with a layer of titanium-nitride (a few nanometers thick) in order to prevent multipacting. The presence of bellows in the outer conductor allows antenna penetration into the cavity beam tube to be adjusted in order to vary the coupling to the cavity. The inner conductor of the coupler can be DC-biased in order to suppress multipacting. The input coupler has three electron current pick-up probes in order to measure the electron activity inside the coupler.

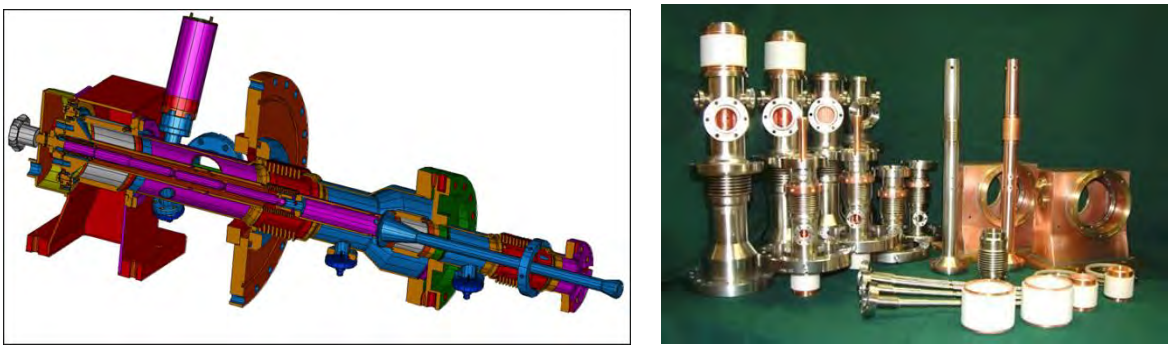

Figure 4-1: Schematic drawing of the TTF-III input coupler (left) and several components of the TTF-III input coupler (right).

4.2.2 Conditioning at Test Stand

One of the input couplers for the DESY cavities, i.e., CP3C12, was pre-conditioned at DESY, while the other, CP3C70, was pre-conditioned at LAL-Orsay. The high-power test stand for RF conditioning at LAL is shown in Figure 4-2. The typical conditioning results of the TTF-III input couplers are shown in Figure 4-3. Both the cavities were successfully conditioned without any difficulties. Two sets of input couplers for two FNAL

cavities were pre-conditioned at SLAC without any difficulties and were then delivered to FNAL to be assembled with the cavities.

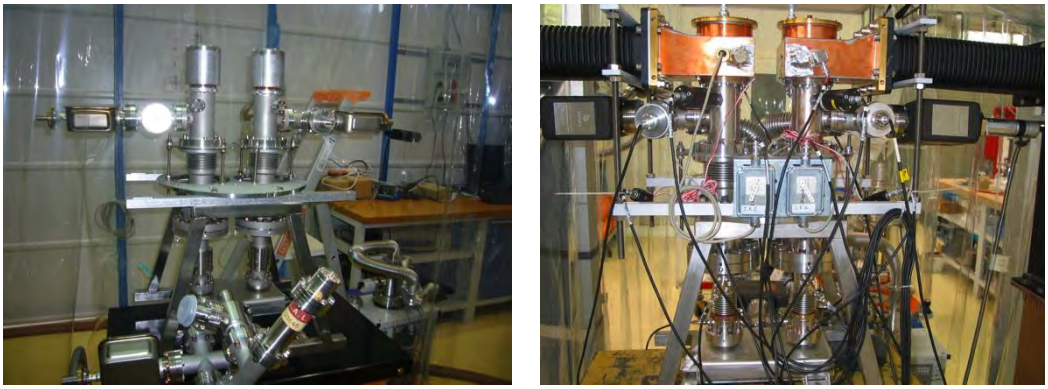

Figure 4-2: Experimental set-up of high-power test stand at LAL.

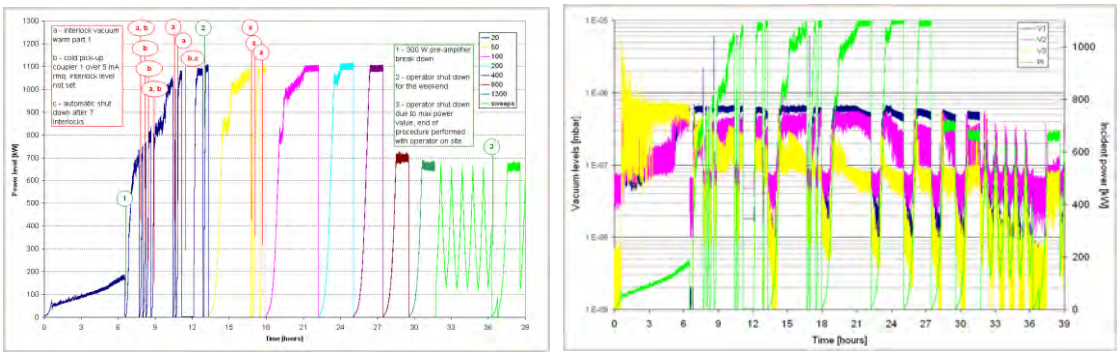

Figure 4-3: RF conditioning results of TTF-III input couplers (CP3C70 [cold] and CP3H61 [warm]) at LAL.

4.2.3 Conditioning in Cryomodule at Room Temperature

After the installation of Cryomodule-C into the STF tunnel, the connection of a warm coupler with a cold coupler and the assembly of waveguide transitions were carried out by a member of DESY. Figure 4-4 shows the arrangement used for the RF conditioning of the four TTF-III input couplers in the cryomodule by a high-power RF source with a 5 MW pulsed klystron. An electron activity monitoring system that included electron pick-up probes and an interlock system for coupler protection was supplied by DESY, and the system was attached to the TTF-III input couplers, as shown in Figure 4-5. The conditioning of the input couplers at room temperature before cooling was carried out at up to 500 kW with a pulse width of 0.5 ms and up to 200 kW with a pulse width of 1.5 ms under the condition of total reflection. The average conditioning time for the four TTF-III input couplers was about 21 h, as shown in Figure 4-6.

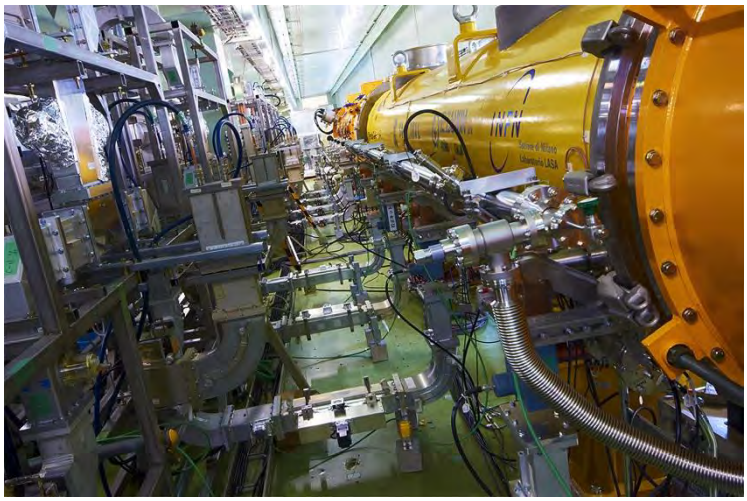

Figure 4-4: Experimental apparatus used for RF conditioning of the input couplers with a high-power RF source in Cryomodule-C.

Figure 4-5: Electron interlock system for coupler protection supplied by DESY.

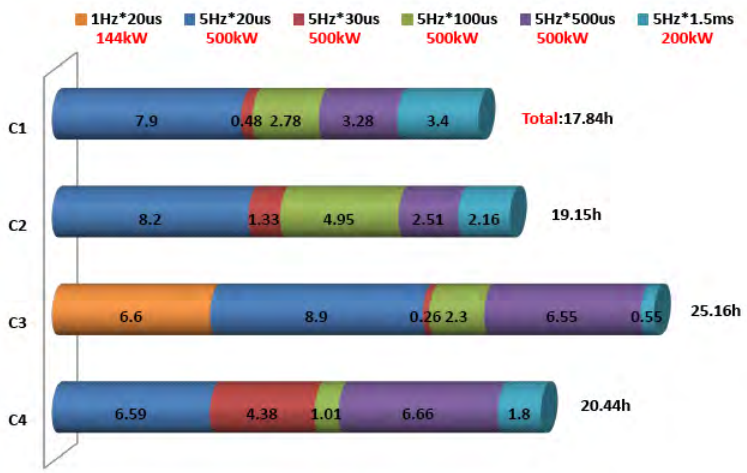

Figure 4-6: Conditioning results of the four TTF-III input couplers in Cryomodule-C at room temperature (the average conditioning time was 21 h, and the vacuum interlock level was set at 2×10^{-4} Pa).

4.3 STF-2 Input Couplers

4.3.1 Coupler Design

The input coupler, which consists of a cold and a warm coupler, has two TRISTAN-type coaxial disk RF windows, as shown in Figure 4-7. In particular, a bellows at the outer conductor in the 5 K part was eliminated in order to make the cavity assembly function better. The STF-1 input couplers used for the phase 1.0 of the STF had a simple structure and no variable coupling. Several improvements were included in the STF-2 input couplers for the S1-Global cryomodule. A schematic drawing and a photo of the completed STF-2 input couplers are shown in Figure 4-8. The main features of the STF-2 coupler are summarized as follows.

The bellows were attached at the antenna tip of the inner conductor so that a variable coupling of ±30% was available. The characteristic RF impedance was 41.5 Ω, because the diameter of the inner conductor was enlarged in order to insert a mechanism to enable variable coupling inside the inner conductor. Thermal anchors at 5 K and 80 K were improved to suppress heat losses more efficiently. The doorknob transition was modified to be more compact in order to reduce the total length for connection to a waveguide system.

Figure 4-7: TRISTAN-type coaxial ceramics disk (left) and RF windows after first brazing (right).

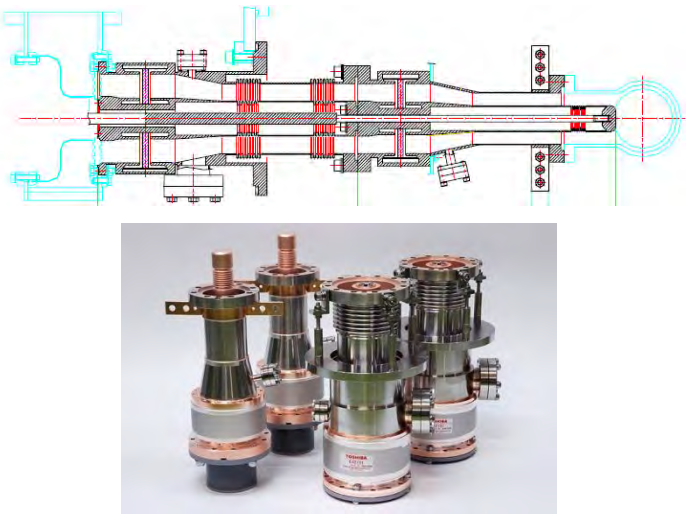

Figure 4-8: Schematic drawing of STF-2 input coupler (top) and two sets of completed STF-2 input couplers (bottom).

The calculated static and dynamic thermal losses at an input coupler are summarized in Table 4-2. The static loss of 1.1 W at 5 K is five times larger than the dynamic loss of 0.2 W at an input RF power of 350 kW. The elimination of the thin bellows at the outer conductor of the 5 K part may be one of the causes of the high static loss at 5 K.

Table 4-2: Calculated static and dynamic thermal losses at the input coupler.

	80 K	5 K	2 K
Static Loss [W]	5.0	1.1	0.05
Dynamic Loss [W]	3.0	0.2	0.03

(The outer conductor at the cold section consists of 1-mm thick stainless steel and 5-μm thick copper plating.)

4.3.2 Conditioning at Test Stand

Prior to the assembly of the 9-cell cavities, the input couplers were conditioned using a high-power test stand, as shown in Figure 4-9. The RF input power required for the conditioning in travelling wave mode at the test stand was determined to be four times higher than that in standing wave mode in the cryomodule. The conditioning began with short pulses of 0.01 ms or 0.1 ms, and the RF power level was increased very carefully. Finally, conditioning up to 1.0 MW using a pulsed operation with a 1.5 ms pulse width at 5 Hz was successfully performed on the four input couplers. The conditioning time at the test stand was approximately 60–120 h, as listed in Table 4-3.

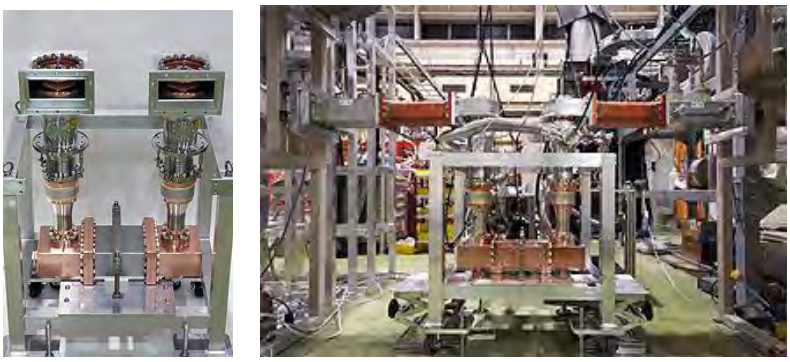

Figure 4-9: Experimental apparatus used for high-power test stand at KEK.

Table 4-3: RF conditioning of STF-2 input couplers.

Pulsed operation	Couplers #1 & #2 max. Prf, Time	Couplers #3 & #4 max. Prf, time
5 μs, 1–5 Hz	1500 kW, 33 h	--
10 μs, 1–5 Hz	1230 kW, 47 h	1080 kW, 33 h
20 μs, 5 Hz	--	1140 kW, 1 h
30 μs, 5 Hz	1010 kW, 5 h	1120 kW, 2 h
60 μs, 5 Hz	1060 kW, 4 h	--
0.1 ms, 5 Hz	950 kW, 6 h	1050 kW, 7 h
0.2 ms, 5 Hz	880 kW, 6 h	--
0.5 ms, 5 Hz	820 kW, 4 h	800 kW, 14 h
1.0 ms, 5 Hz	810 kW, 6 h	--
1.5 ms, 5 Hz	750 kW, 8 h	270 kW, 6 h
Total time	119 h	63 h

4.3.3 Conditioning in Cryomodule at Room Temperature

After the installation of the cryomodule into the STF tunnel, the connection of a warm coupler with a cold coupler was carried out in a work area covered with a special booth to maintain a clean environment. Figure 4-10 shows the apparatus used for RF conditioning in the cryomodule using a high-power RF source. In-situ baking of cold RF windows inside the cryomodule was carried out at 85 °C for 15 h. The baking of cold RF windows prior to conditioning was very effective for reducing the conditioning time. The conditioning of the input couplers at room temperature before cooling was carried out at up to 500 kW with a pulse width of 0.5 ms and up to 200 kW with a pulse width of 1.5 ms under the condition of total reflection. The average conditioning time of the four STF-2 input couplers was about 15 h, as shown in Figure 4-11. This was slightly shorter than that of the TTF-III input couplers.

Figure 4-10: Experimental apparatus used for RF conditioning with a high-power RF source in Cryomodule-A.

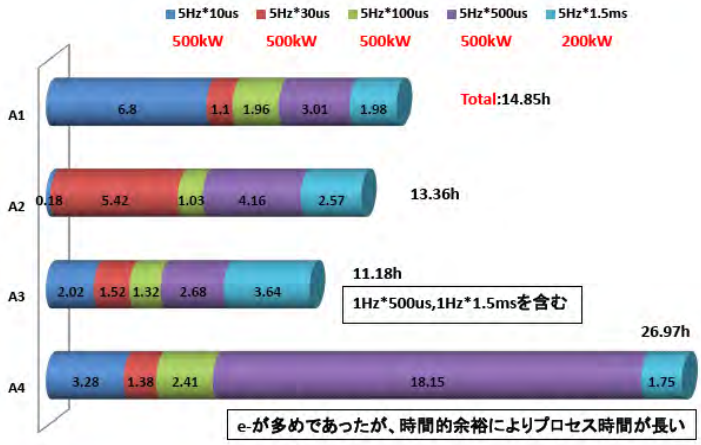

Figure 4-11: Conditioning results of four STF-2 input couplers in Cryomodule-A at room temperature (the average conditioning time was 15 h, and the vacuum interlock level was set at 2×10^{-4} Pa).

5 Tuners

5.1 Introduction

5.1.1 Technical Challenges of TESLA Cavity Tuning Systems

TESLA-type, as well as TESLA-like, cavities are characterized by a significant sensitivity to mechanical detuning, for instance, longitudinal sensitivity, in terms of hertz per micrometer strain, whose value is always comparable to the resonator bandwidth in pulsed operations. Several dynamic effects simultaneously influence the stability of the cavity frequency, and the most noticeable effects are from helium bath pressure fluctuations, radiation pressure at the cavity walls (the so-called Lorentz Force detuning or LFD), and external mechanical vibrations (microphonics).

In order to maximize the RF power efficiency of LLRF controls and to lower electric fields at the input coupler during operation in such a scenario, a fast tuner is required to compensate for the dynamic detuning as well as to provide basic, quasi-static cavity tuning functionalities.

Any candidate tuner system for ILC must withstand the challenging working environment, which is characterized by insulation vacuum, cryogenic temperatures, and virtually no possibility of in-situ repairs. Affordability is therefore a primary issue that should be addressed both by the use of reliable and experienced components as well as by their design, which should take into account alternative configurations where actuators are placed outside the vacuum vessel.

As a reference, the guidelines for the ILC cavity tuner have been expressed within the ILC RDR document. The tuner is expected to provide a maximum tuning range of 600 kHz (±300 kHz around the nominal frequency) with an effective resolution at the hertz level (i.e., on the order of hertz per step). The frequency tuning action, i.e., slow or fast, generated by the tuner by different means always results in a strain applied to the cavity in the longitudinal direction. As a reference, stretching the cavity from its mechanically neutral point always results in an increase in the resonant frequency value.

The amount of LFD to be compensated for is proportional to the square of the accelerating field, and it is expected to be approximately -600 Hz for a TESLA-type cavity during the flat-top RF pulse operation at the design gradient (31.5 MV/m) in the main linac. This value is strongly dependent upon the mechanical stiffness of the resonator and the cavity design, and its constraints could be optimized to lower the net LFD effect.

Each resonator must be close to the on-tune condition for almost the entire duration of the RF pulse in order to achieve the tight field stability level imposed by the beam quality: this corresponds to errors of up to 0.07% for amplitude and 0.35° for the phase. This can only be achieved for an ILC-sized cavity set by developing an adaptive, automated tuner control system that is capable of complete integration into higher levels of cavity controls.

From a more general point of view, a coaxial tuning solution should be considered as long as it has a positive impact on the final inter-cavity distance. Moreover, the tuning system should be compatible with large-scale production in terms of unit price as well as installation and operation requirements.

5.1.2 Tuners Installed at S1-Global

As shown in Figure 5-1, the S1-Global Cryomodule-C hosted four TESLA-type cavities. The first two units in the string, i.e., C1 and C2, have been procured by FNAL and equipped with an INFN coaxial Blade Tuner;

the other two cavities, i.e., C3 and C4, are supplied by DESY and are equipped with the latest lateral tuner designed by Saclay/DESY.

Cryomodule-A hosted four TESLA-like cavity units from KEK that were equipped with the coaxial slide-jack tuner, which were also developed by KEK. For the first two cavities in the string, i.e., A1 and A2, slide-jack tuners were installed between the tank pads, and for cavities A3 and A4, slide-jack tuners were installed outside the pads on the side of the couplers, because of which they acted as lateral tuners.
Each of the three tuning systems will be briefly described in the following sections.

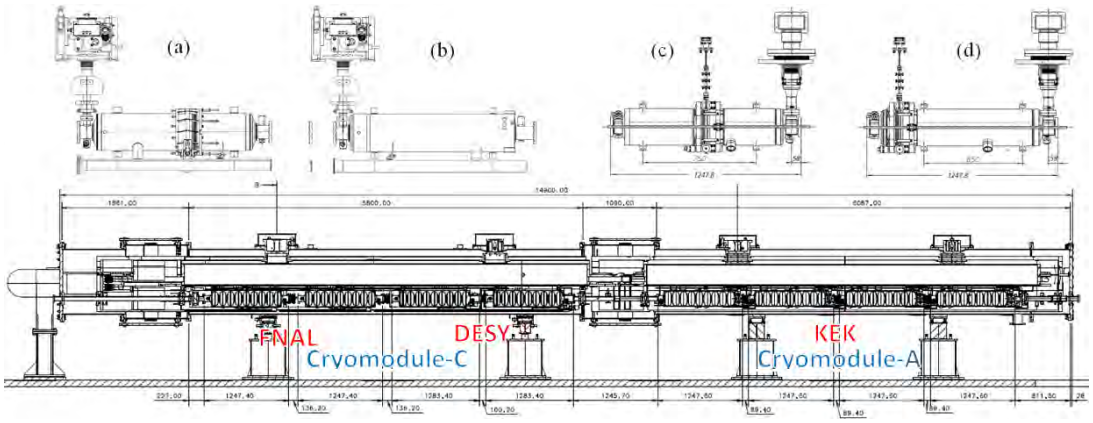

Figure 5-1: Tuner sequence in the S1-Global cavity string.

5.2 The Blade Tuner

The Blade Tuner was developed by INFN Milan as a coaxial and light tuning solution for TESLA-type cavities, and the original model was built for super-structure experiments at DESY. As shown in Figure 5-2, it features the concept of elastic blades capable of transforming an azimuthal movement of the central ring into a longitudinal cavity strain with zero backlash. The tuner mechanics as well as the blades are made from titanium owing to its mechanical strength and to minimize the differential thermal contraction.

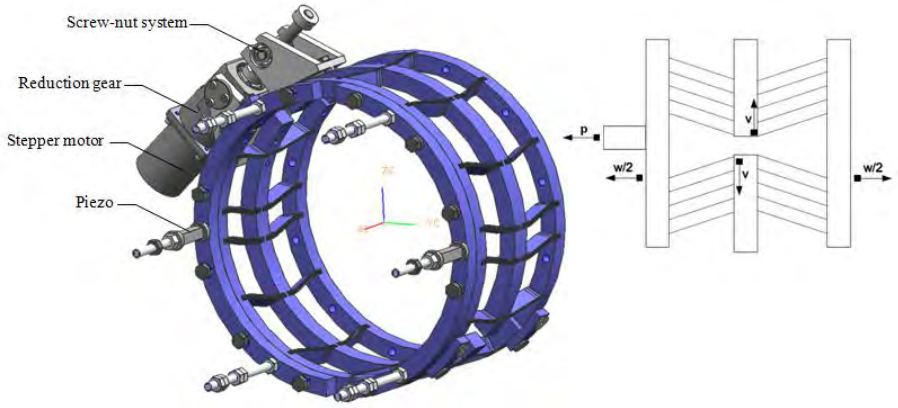

Figure 5-2: 3D view (left) and schematic view (right) of the Blade Tuner.

The slow tuning action is generated by a cold stepper-motor-based drive unit that is coupled to a mechanical reduction gear. A CuBe threaded shaft is used as a screw-nut system and this generates the azimuthal motion of the central rings. Fast tuning action is ensured by two piezoelectric ceramic actuators that are installed on the longitudinal plane on opposite sides of the helium tank; their action is in series to the tuner motion in order to achieve the highest possible efficiency during the transfer of their stroke to the

cavity. The entire mechanical load acting on the tuning system is generated by the cavity elasticity. Upon installation, an initial pre-load is set by calibrated stretching of the cavity length in order to achieve optimal working conditions for the piezo actuators. During operation, the mechanical load in the system varies in an increasing manner along the tuning range; the cavity elongation is always distant from its neutral point. Details of the tuner and the actuators installed are reported in Table 5-1.

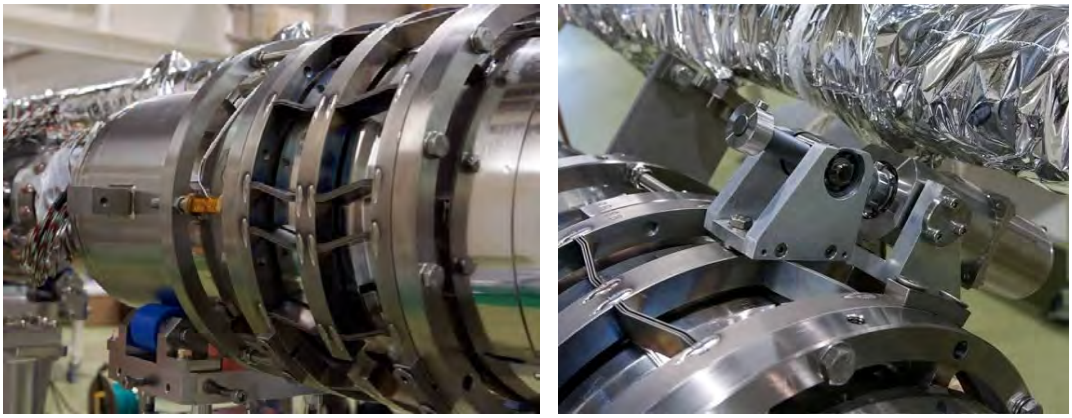

Figure 5-3: Blade Tuner installed at S1-Global (left) and a close-up view of the cold drive unit (right).

The Blade Tuner cavity unit, as shown in Figure 5-3, has been realized through a collaboration between FNAL and INFN for the production of CM-2 for the ILC_TA facility at Fermilab. The coaxial tuner is installed on a dedicated helium tank that is split in two halves by a bellow to allow for the tuning of the longitudinal strain. Moving the tuning bellow to the central position allowed for a simplification of the end cone regions compared to the original TTF design.

5.3 The Saclay/DESY Tuner

This tuner has been developed at DESY from the original Saclay design with the added benefits of a long operational experience, as the tuner has been in use, with minor modifications, since the TTF has been in operation. The units installed at S1-Global are two of the latest produced for the FLASH linac and the design of these are close to the final XFEL tuning solution.

As shown in Figure 5-4, the DESY/Saclay tuning mechanics consists of a compact double lever installed on the pick-up side of the titanium helium tank. The lever, designed for a 1:25 reduction ratio, transfers to the cavity ring, the tuning action generated by a cold stepper-motor-based drive unit equipped with a reduction gear and a screw-nut system. Two piezo actuators are installed to provide dynamic fast tuning capabilities; they are both contained by a single preloading frame mounted on one side that acts on the cavity through the same leverage mechanics.

The piezo frame provides the required mechanical load on the actuators almost independent of the load exerted by the cavity through its elasticity. The latest DESY/Saclay tuners, such as those installed at S1-Global, are indeed designed to stretch the cavity from its neutral point during tuning.

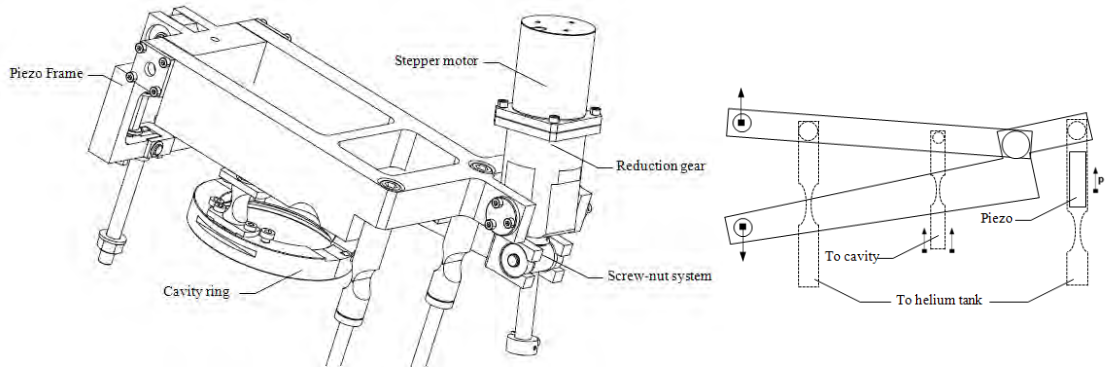

Figure 5-4: DESY/Saclay pictorial 3D view (left) and its schematic view (right).

The entire tuning system, as shown in Figure 5-5, is installed outside the helium tank body, and it therefore retains its structural integrity. A bellow with reduced radius is included at the side of the tank, in between the tuner joints, in order to enable strain tuning. The double piezo configuration, in this case, is selected mainly for redundancy reasons, and the parallel action of the two actuators does not lead to a doubling of the tuning effect. Moreover, the double piezo configuration, which is included in both the Blade and DESY/Saclay tuners, allows for the possibility of using a spare stack as a passive sensing element.

Details of the tuner and the actuators installed are reported in Table 5-1.

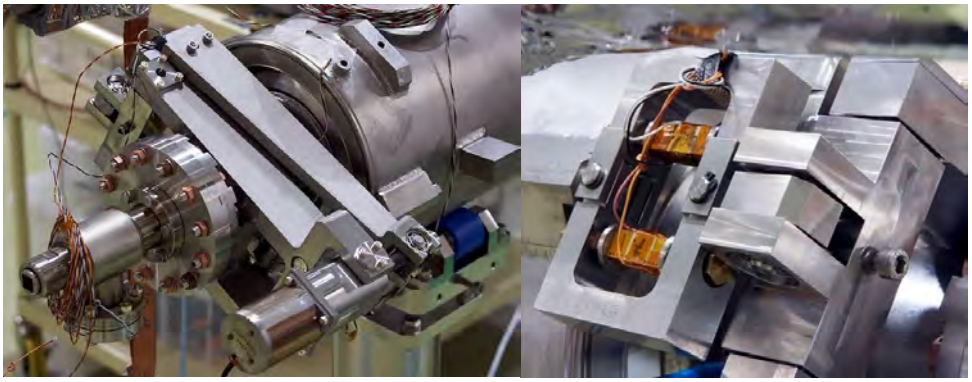

Figure 5-5: DESY/Saclay Tuner installed at S1-Global (left) and a close-up view of the piezo preloading frame (right).

5.4 The Slide-Jack Tuner

The slide-jack tuner has been specifically designed for the TESLA-like cavities developed by KEK for the STF project. A global strategy has been pursued at KEK regarding the mechanical design of these units that was devoted to the minimization of the sensitivity to LFD through a stiffer design of the cavity and its constraints. The geometry of the resonator and end cone regions has therefore been optimized, and this has resulted in a longitudinal spring constant significantly higher than in the original TESLA-type system. For this reason, a suitable coaxial tuning mechanism has been designed. The slow tuning action, as shown in Figure 5-6, is generated through rolling elements sliding on a sloping surface; this mechanism transforms the rotation of a driving shaft into a longitudinal cavity strain. In order to maximize reliability and ease of maintenance, no cold drive unit is included in the design. The main driving shaft passes through the cryomodule vacuum vessel and the drive unit is placed outside, as shown in Figure 5-7. Either a stepper motor or a manual driver can be used.

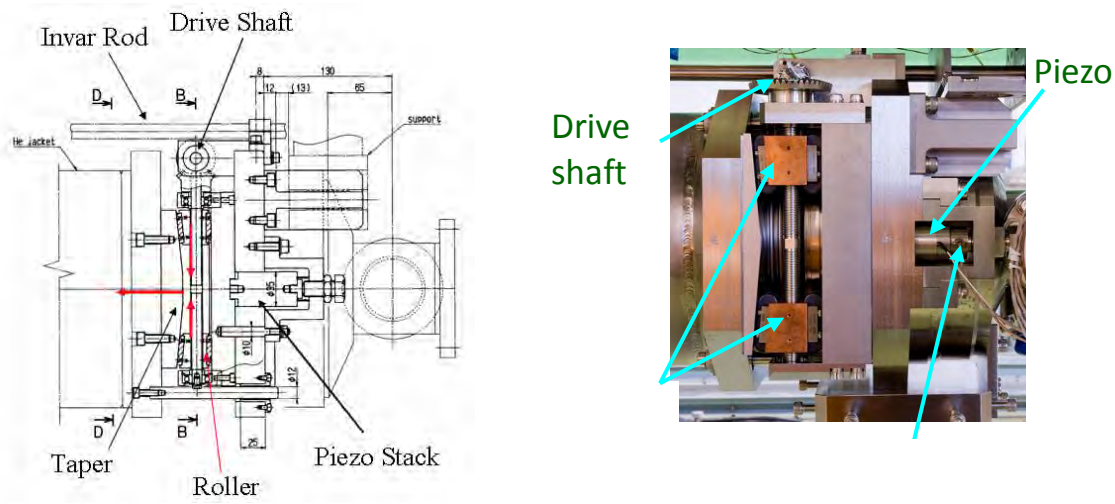

Figure 5-6: Schematic view (left) and photograph of slide-jack (right).

A single high-voltage, multiple-layer piezo actuator is installed at the coupler side of the tank to provide fast tuning capabilities. The absolute value of the LFD for comparable field values are expected to be much smaller than the RDR reference ones owing to the special stiff design, and the fast actuator has been dimensioned accordingly.

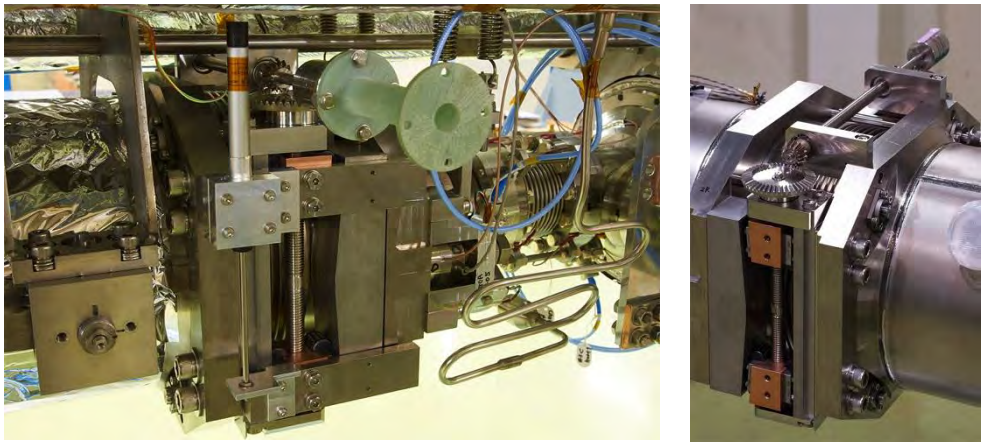

Figure 5-7: Slide-jack tuner at S1-Global.

In the baseline design of this coaxial tuner, the slide-jack mechanics are installed between the pads, and thus, it acts as a middle tuner. In this case, similarly to the Blade Tuner case, the helium tank is split into two halves by a bellow. This tuner geometry will be referred to as the central slide-jack in the following text. In addition, for comparing the effect of different geometries on the tuning system, a different cavity package has been developed that includes the same slide-jack coaxial mechanics installed outside the pad on the coupler side, whereby the tuner effectively acts as a lateral tuner. This latter solution will be referred to as the lateral slide-jack tuner.

5.5 S1-Global Tuner Overview

Table 5-1 summarizes and compares the values of the important parameters for each tuner and for the slow and fast actuators installed. Relevant parameters for the control of piezo actuators, such as the nominal stroke and capacitance, are also presented.

Table 5-2: Overview of S1-Global tuner parameters.

	Blade Tuner	DESY/Saclay Tuner	Slide-Jack Tuner
Type	Coaxial	Lateral – PU side	Coaxial/ lateral coupler side
Cavity	C1,C2; TESLA-type	C3, C4; TESLA-type	A1, A2; coaxial A3, A4; lateral KEK TESLA-like units
Design tuner stiffness	30 kN/mm	40 kN/mm	290 kN/mm
Drive unit	Inside vessel, Stepper motor + HD	Inside vessel, Stepper motor + HD	Outside vessel, both manual or stepper motor actuation
Nominal range	600 kHz	500 kHz	900 kHz
Nominal sensitivity	1.5 Hz/step	1 Hz/step	3 Hz/step
Piezo	2, thin-layer (0.1 mm) Dim. 10 × 10 × 40 mm	2, thin-layer (0.1 mm) Dim. 10 × 10 × 40 mm	1, thick-layer (2 mm) Dim. ϕ35 × 78 mm
Voltage	200 V	200 V	1000 V, operated at 500 V
Nominal piezo stroke at RT	55 μm	55 μm	40 μm
Nominal piezo capacitance at RT	8 μF	8 μF	0.9 μF

6 Cryomodules

6.1 Introduction

6.1.1 Layout of the Two S1-Global Modules

The S1-Global cryomodule consists of two 6-m cryomodules, i.e., Module-A and Module-C, which are shown in Figure 6-1. The total length of the S1-Global cryomodule is 14.9 m, in which the Module-A and Module-C are connected with a vacuum bellows. Module-C was designed to accommodate four cavities from FNAL and DESY, and Module-A was designed to accommodate four cavities developed by KEK and having two types of cavity jackets. In total, eight cavities were installed in the S1-Global cryomodule. The parameters of the two 6-m cryomodules are listed in Table 6-1. Figure 6-2 shows the 2 K cold box and the S1-Global cryomodule. Module-C is located upstream, and Module-A is located downstream of the cooling channel. Module-A and Module-C have differently sized cooling pipes and these cooling pipes were connected with a reduced number of pipe components by welding in the connection area. The pipe sizes are listed in Table 6-1 and shown in Figure 6-2. The outer diameters of the gas return pipes (GRPs) in Module-A and Module-C were 318.5 mm and 312.0 mm, respectively. As a result, the axes of the two pipes were 6.5 mm apart in the vertical direction, whereas the axes of the two-cavity string were coincident. At both ends of the GRPs, a closing flange with an extension pipe with ø = 76 mm was welded to allow the interconnection of the 2-module gas return pipes.

The four cavities in a string in each module were connected via their beam pipes. However, the two cavity strings were not joined to each other, and the outer ends of each string were closed with a valve.

6.2 Module-C

6.2.1 Module Components and Mechanical Configuration

The design of the Module-C cross-section is almost the same as the TTF-type III cryomodule, as shown in Figure 6-3. The main cryomodule components are the cavity-packages, input couplers, the gas return pipes (GRPs), magnetic shields, two sets of thermal shields, cooling pipes, and vacuum vessel. The cold mass is supported by two composite cylindrical posts from the vacuum vessel, and the distance of 3200 mm between the posts was selected so that the cold mass sag would not exceed 50 μm. The distance of 1383.6 mm between the input couplers, which is the same as in the TTF-type III and XFEL designs, was used for four cavities although the cavity-packages from FNAL and DESY have different lengths, i.e., 1247.4 mm and 1283.4 mm, respectively. This mismatch was resolved by the bellows pipes between the cavities. The designs of these two cavity jackets are different because of the different type of frequency tuner used, i.e., the blade tuner and Saclay-type tuner, as shown in Figure 6-1. However, for both the cavity packages, the cavity support lugs are all separated by 750 mm along their axis, and located at a fixed distance of 197.5 mm from the input coupler axis, and as a result, the cavity package supports to the GRPs are identical, i.e., they are “plug compatible.”

The frequency tuners of these cavities were driven by the cold motor and the piezo element. The cold motors were installed inside the 5 K shield.

The DESY and FNAL cavities were designed to be enclosed by the magnetic shields. These cavities are shown in Figs. 6-5 and 6-6 before and after assembly of the magnetic shields, respectively.

6.2.2 Thermal Configuration

The cold mass at 2 K was enclosed with two thermal shields at 5 K and 80 K, which were cooled with liquid helium (LHe) and liquid nitrogen (LN2), respectively, as shown in Figs. 6-8 and 6-9. Each thermal shield consisted of six pieces of Al plate, i.e., four pieces in the bottom components and two pieces for the upper components, as shown in Figure 6-8 and 6-9. These pieces were mechanically and thermally connected by welding. The 5 K and 80 K shields were covered with 10 and 30 layers of multi-layer insulation system, respectively. The cooling pipe in forward flow was welded to the shield while the return pipe was not welded and was located inside the shield. When the shields were cooled to 5 K or 80 K, the thermal contractions of the shields were tolerated by sliding along the flange of the movable support post. Therefore, while the shields were bolted to the flanges of the fixed post, which creates sufficient thermal contact, they were thermally connected to the flanges of the movable post by two Cu braid cables.

6.3 Module-A

6.3.1 Module Components and Mechanical Configuration

Module-A was used for the cold tests in STF phase-1. The thermal and mechanical designs of Module-A were based on the TTF-type III cryomodule, as shown in Figure 6-4. However, the components in Module-A have different dimensions to those in Module-C, as listed in Table 6-1. The cold mass is supported from the vacuum vessel by two composite cylindrical posts separated by a distance of 3153 mm. The cold mass sag is within 50 μm as it is for Module-C. The KEK cavities for Module-A were of two different designs with the frequency tuner in different locations, as shown in Figure 6-1. The type A cavity-package has the tuner located at the center of the helium jacket. The distance between the support lugs along the cavity axis is designed to be 750 mm, i.e., the same distance as in the FNAL and DESY cavities. The type B cavity package has the tuner placed at the opposite end of the jacket with respect to the input coupler. With this configuration, the distance between the support lugs is changed to 650 mm and the tuning action does not require the cavity to slide at the support pads. Because the KEK tuners have a driving motor outside the vacuum vessel, the ports for the shafts were welded onto the vacuum vessel.

The frequency tuners of these cavities were driven by the warm motor and the piezo element. The warm motors were placed outside the vacuum vessel, and the motor and the tuner were connected to the driving shaft. Therefore, the vacuum vessel and two shield plates required holes and a port for the shafts.

Figure 6-7 shows the KEK cavities under the GRPs. The magnetic shields were assembled inside the cavity jackets, and the magnetic shields are not shown in the photos.

6.3.2 Thermal Configuration

The thermal shields were divided into four pieces, i.e., two in the axial direction, and two in upper and lower parts in the vertical direction, as shown in Figs. 6-10 and 6-11. The shields were bolted to the flanges of the fixed and movable support posts. The forward and return cooling pipes were connected to the shields with screws. This cooling scheme was only applied to this shorter length cryomodule. For the actual ILC thermal design, the thermal design of Module-C is preferable. The movement of the movable post and the shields by thermal contraction of the GRP was resolved with the bellows in the cooling pipes between two shield components.

The two thermal shields at 5 K and 80 K were covered with 10 and 30 layers of the multi-layer insulation system, respectively, as in Module-C.

Table 6-1: S1-Global cryomodule parameters.

	Module-A	Module-C
Vacuum vessel length	6087 mm	5800 mm
Vacuum vessel O.D.	ϕ965.2 mm	ϕ965.2 mm
Gas return pipe length	5830 mm	6000 mm
Gas return pipe O.D.	ϕ318.5 mm	ϕ312.0 mm
2 K LHe supply pipe O.D.	ϕ76.3 mm	ϕ76.1 mm
5 K shield pipe O.D. [F/R]	ϕ30/ϕ30 mm	ϕ60/ϕ60.3 mm
80 K shield pipe O.D. [F/R]	ϕ30/ϕ30 mm	ϕ60/ϕ60.3 mm
Cool-down pipe O.D.	ϕ27.2 mm	ϕ42.2 mm
Distance between couplers	1337.0 mm	1383.6 mm
Cavity package	KEK-a/KEK-b	FNAL/DESY
Cavity type	TESLA-like	TESLA-type
Tuner type	Slide jack	Blade/Saclay
Input coupler type	STF-2	TTF-III
Magnetic shield	Inside jacket	Outside jacket
Package length	1247.6 mm	1247.4/1283.4 mm

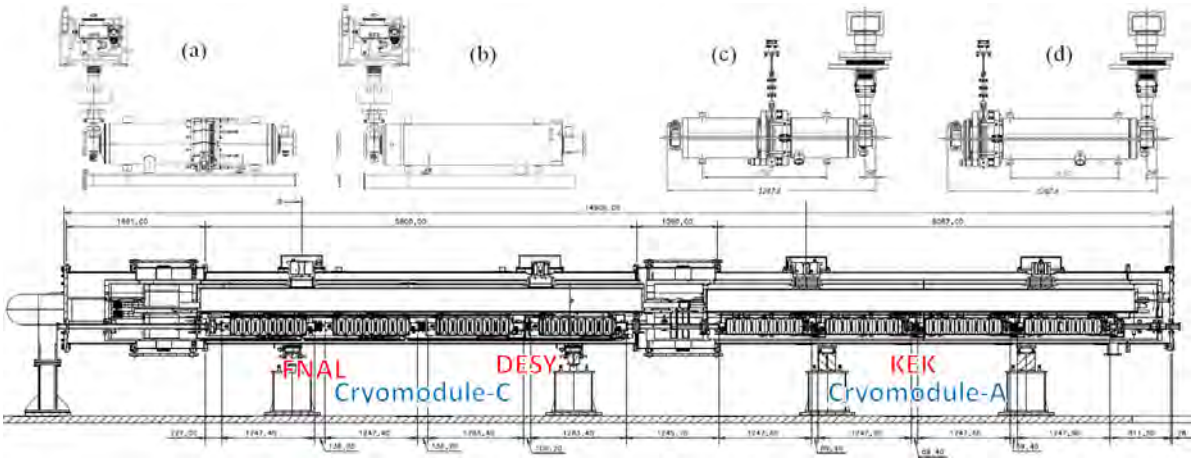

Figure 6-1: Cross-section view of the S1-Global cryomodule and the cavity package developed by each laboratory. (a) FNAL cavity with blade tuner, (b) DESY cavity with Saclay-type tuner, (c) KEK A-type cavity with slide-jack tuner in the center, and (d) KEK B-type cavity with slide-jack tuner in the end.

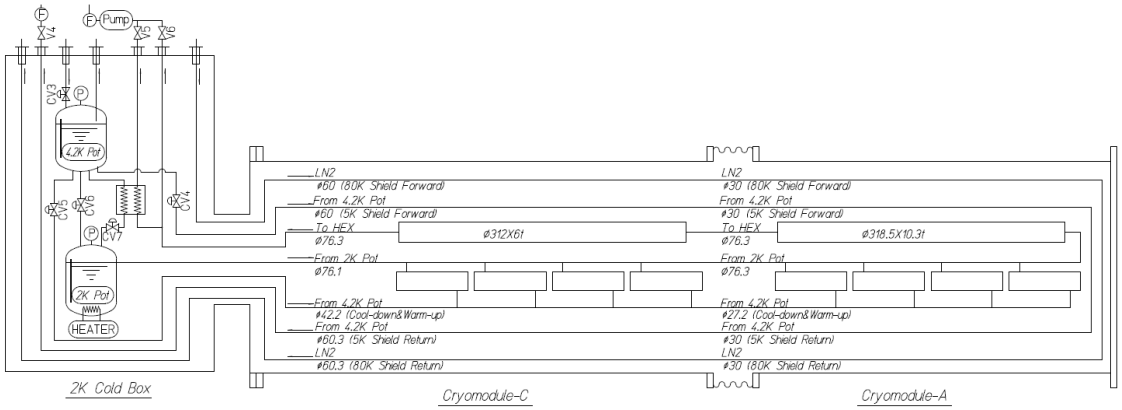

Figure 6-2: Cooling scheme for the S1-Global cryomodule. Module-C is located upstream of the cooling channel.

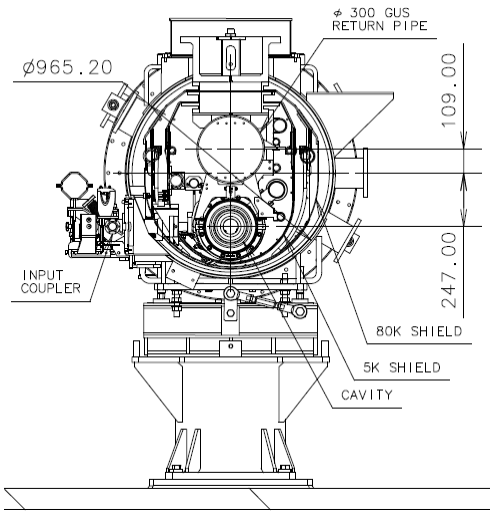

Figure 6-3: Cross-section view of Module-C, which was designed to hold two FNAL cavities.

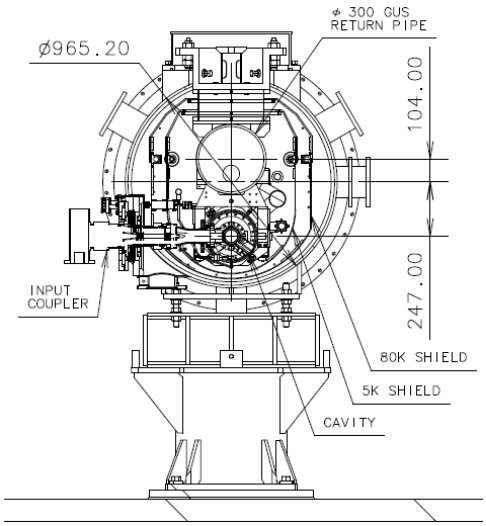

Figure 6-4: Cross-section view of Module-A designed to hold the KEK cavities.

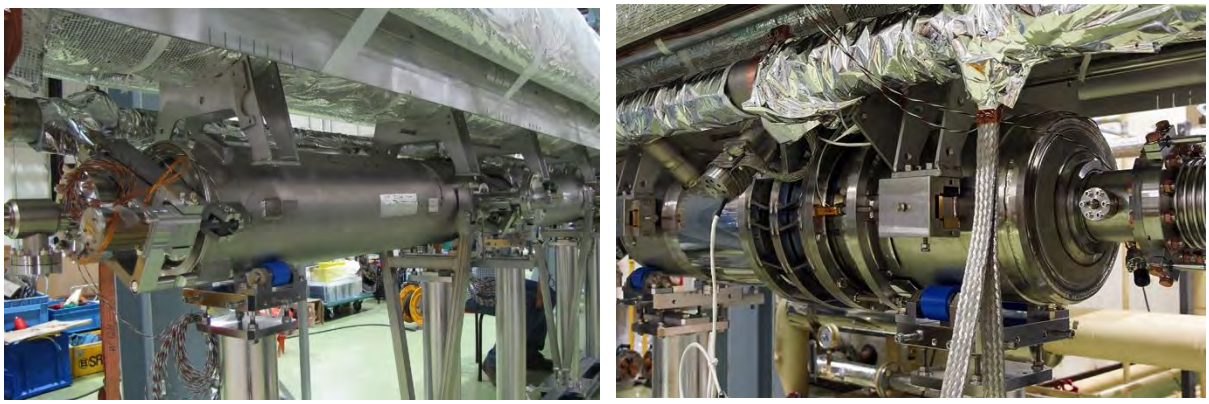

Figure 6-5: DESY (left) and FNAL (right) cavities assembled under the GRP.

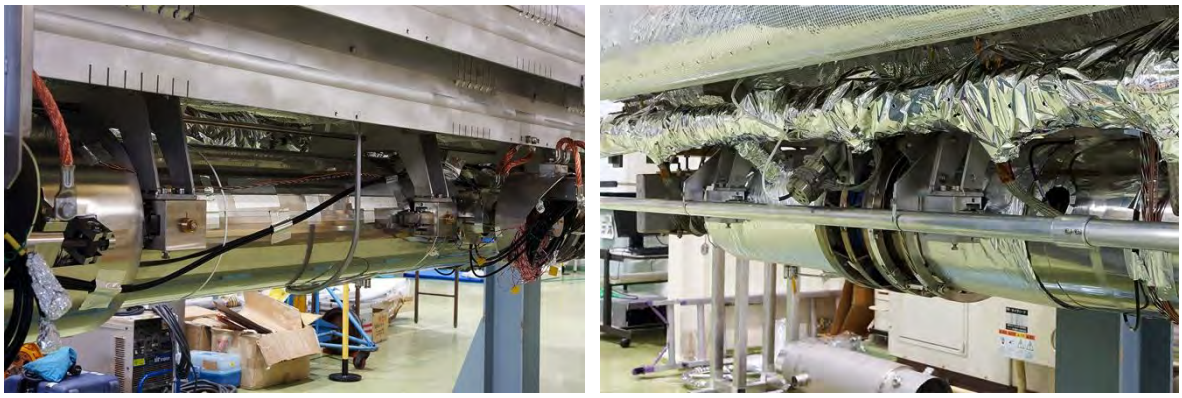

Figure 6-6: Magnetically shielded DESY (left) and FNAL (right) cavities.

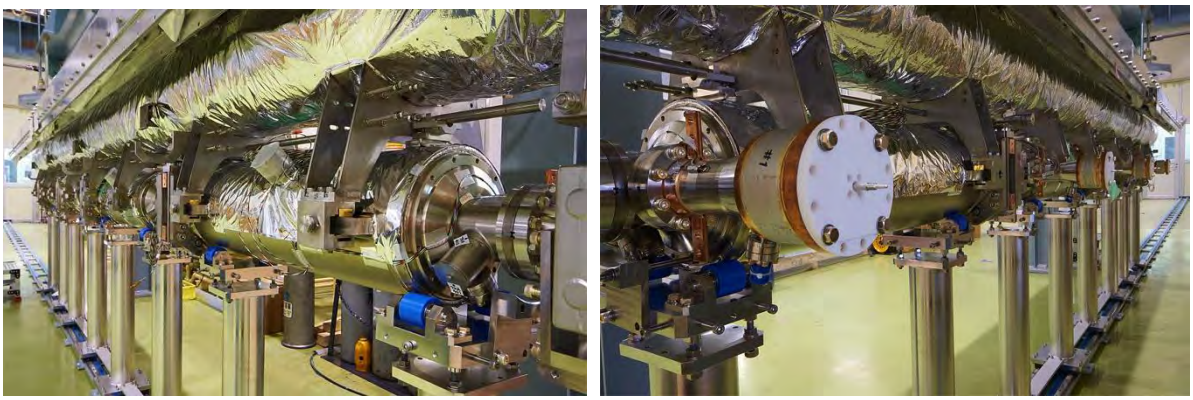

Figure 6-7: KEK cavities, viewed from the left and right with respect to the cavity axis.

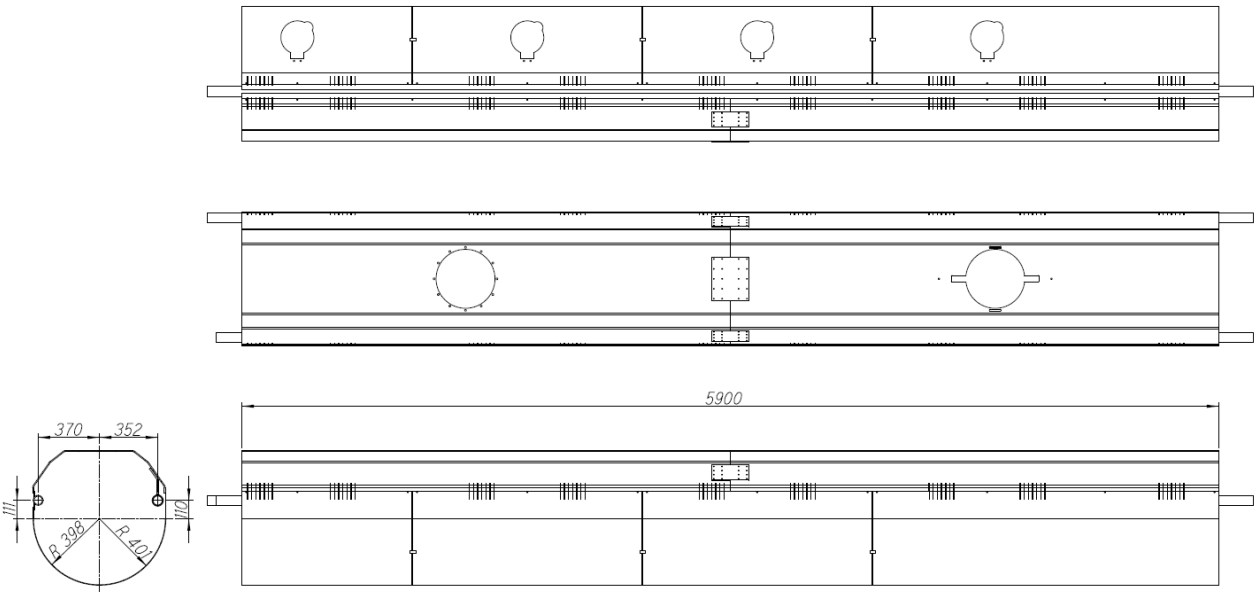

Figure 6-8: 80 K thermal shield for Module-C.

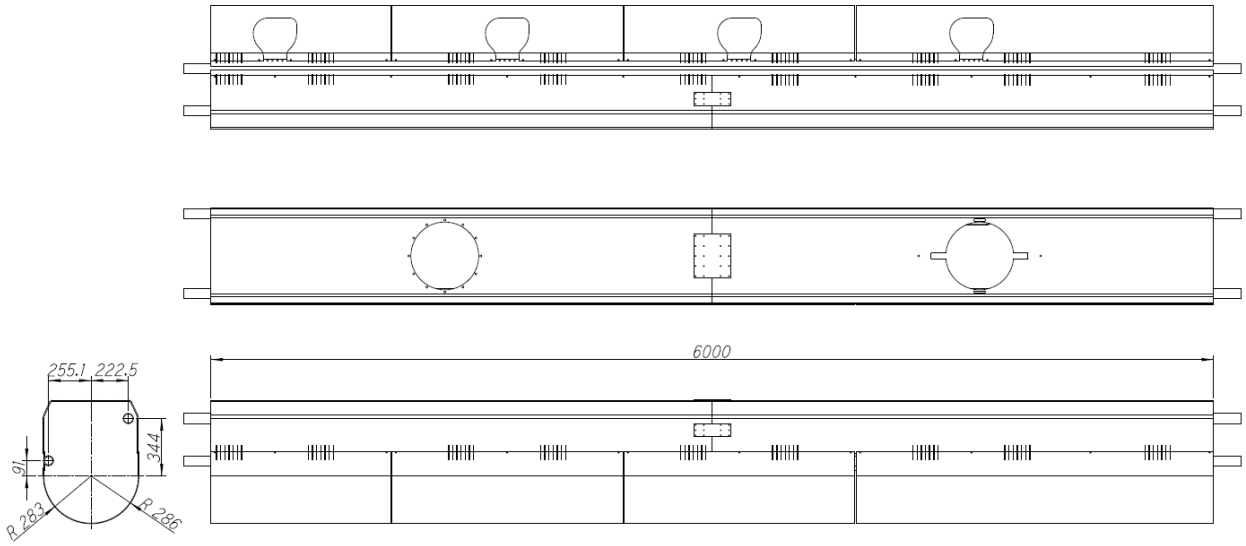

Figure 6-9: 5 K thermal shield for Module-C.

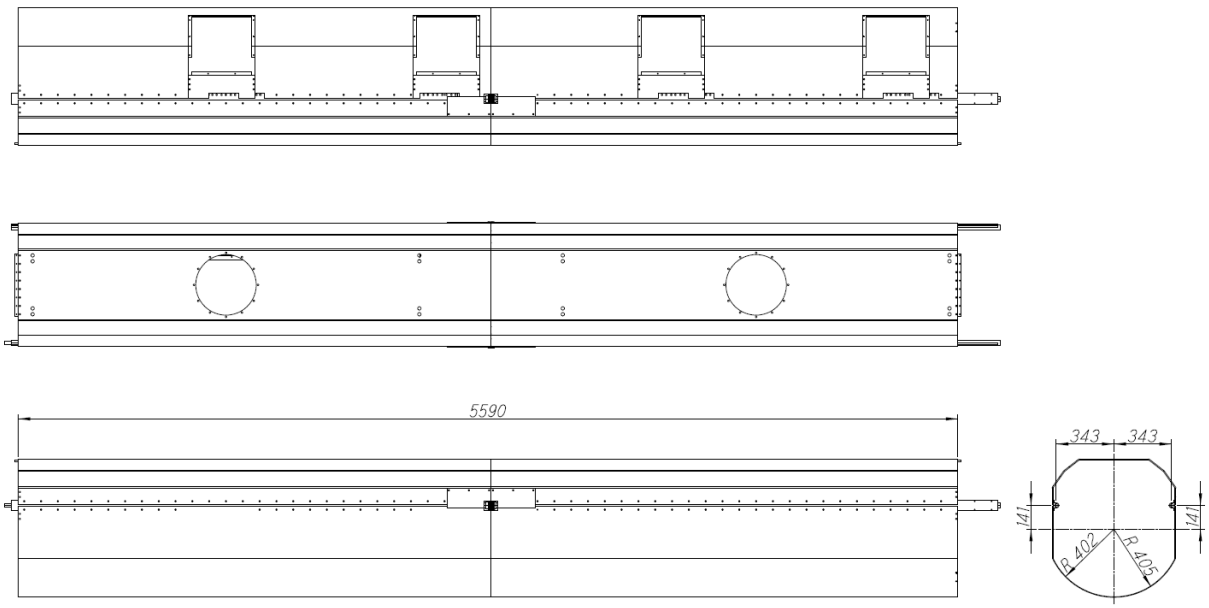

Figure 6-10: 80 K thermal shield for Module-A.

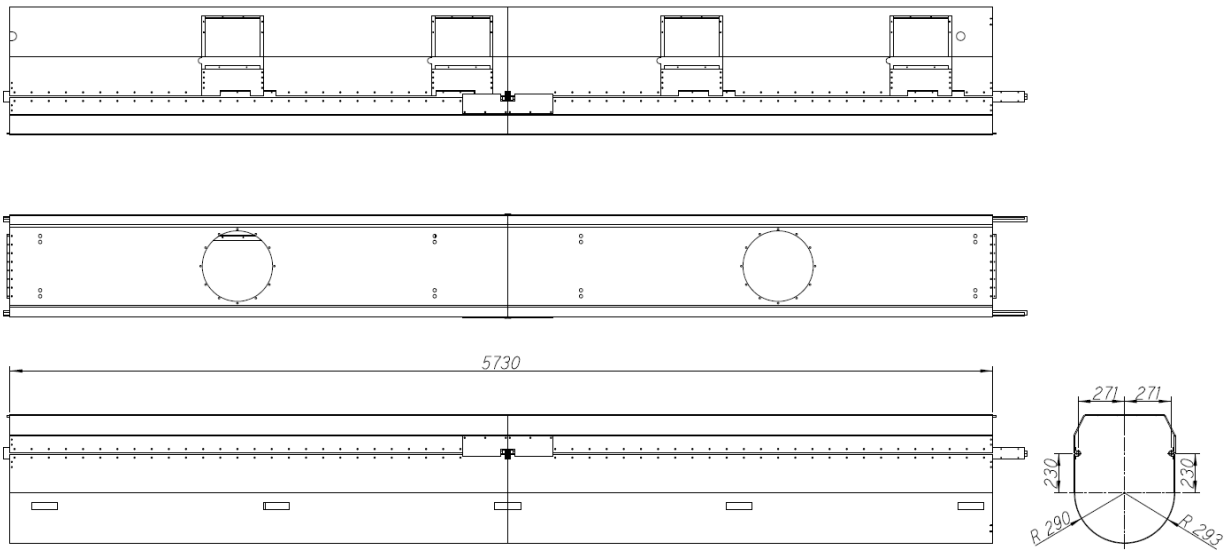

Figure 6-11: 5 K thermal shield for Module-A.

7 Cold Mass Assembly

7.1 Assembly Process Overview

Details of the S1-Global cryomodule are shown in Figure 7-1. Most of the assembly for both Module-C and Module-A can be divided into two processes: the cavity string assembly in a class-10 clean room (CR), and the cold mass assembly outside the CR. For the cavity assembly in a clean room, two weeks was scheduled for each module. For the cold mass assembly, two months for Module-C and one month for Module-A were scheduled. The Module-C assembly was scheduled first to ease the final assembly of the two modules into the STF tunnel. The complete schedule for the assembly of the S1-Global cryomodule is shown in Figure 7-2. In the table shown as Figure 7-2, the total number of days of human effort required is shown at the bottom of each column. For module assembly outside of the clean room, company, and KEK personnel are indicated by C and K, respectively. For the assembly of cavities, tuners, couplers, and magnetic shields, the collaborators from the FNAL, DESY, INFN, and KEK are listed individually.

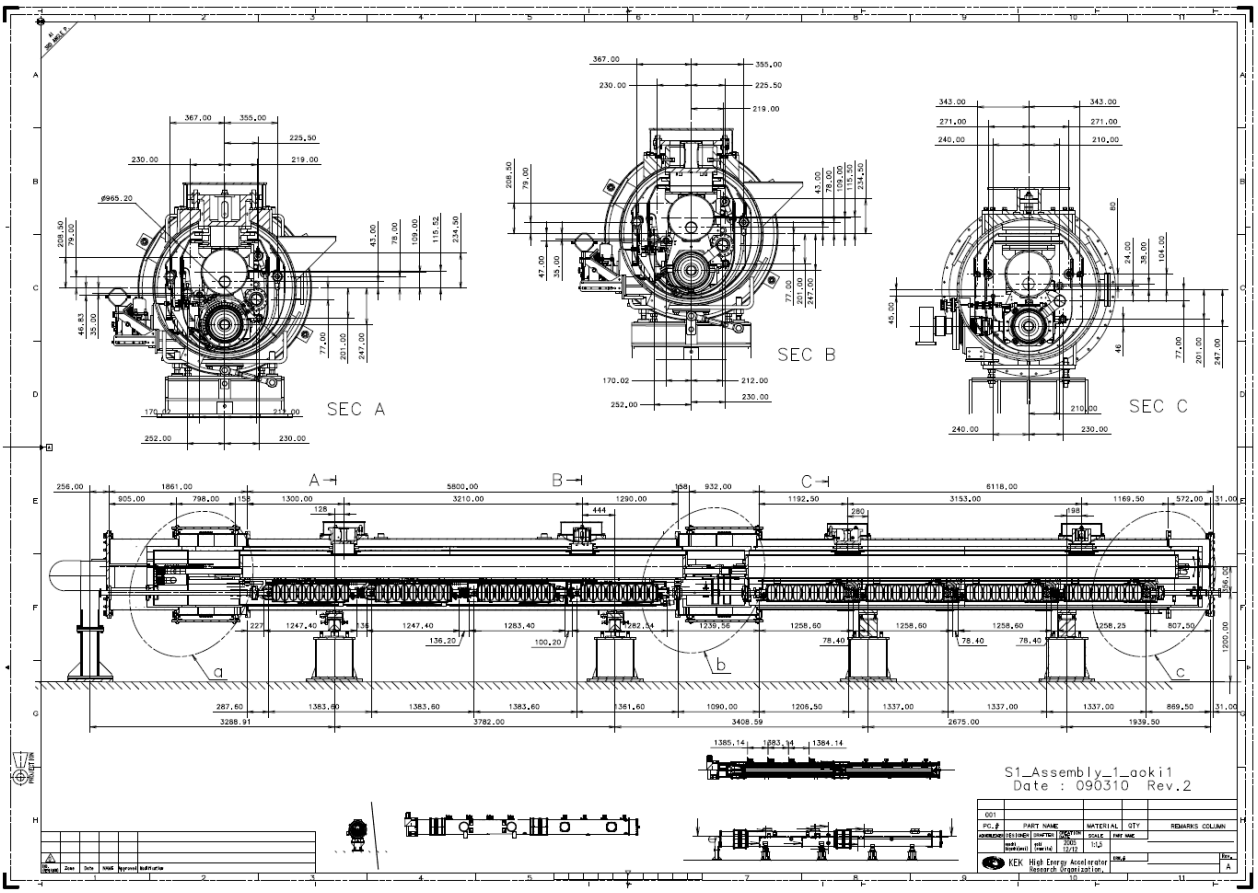

Figure 7-1: Details of the S1-Global cryomodule.

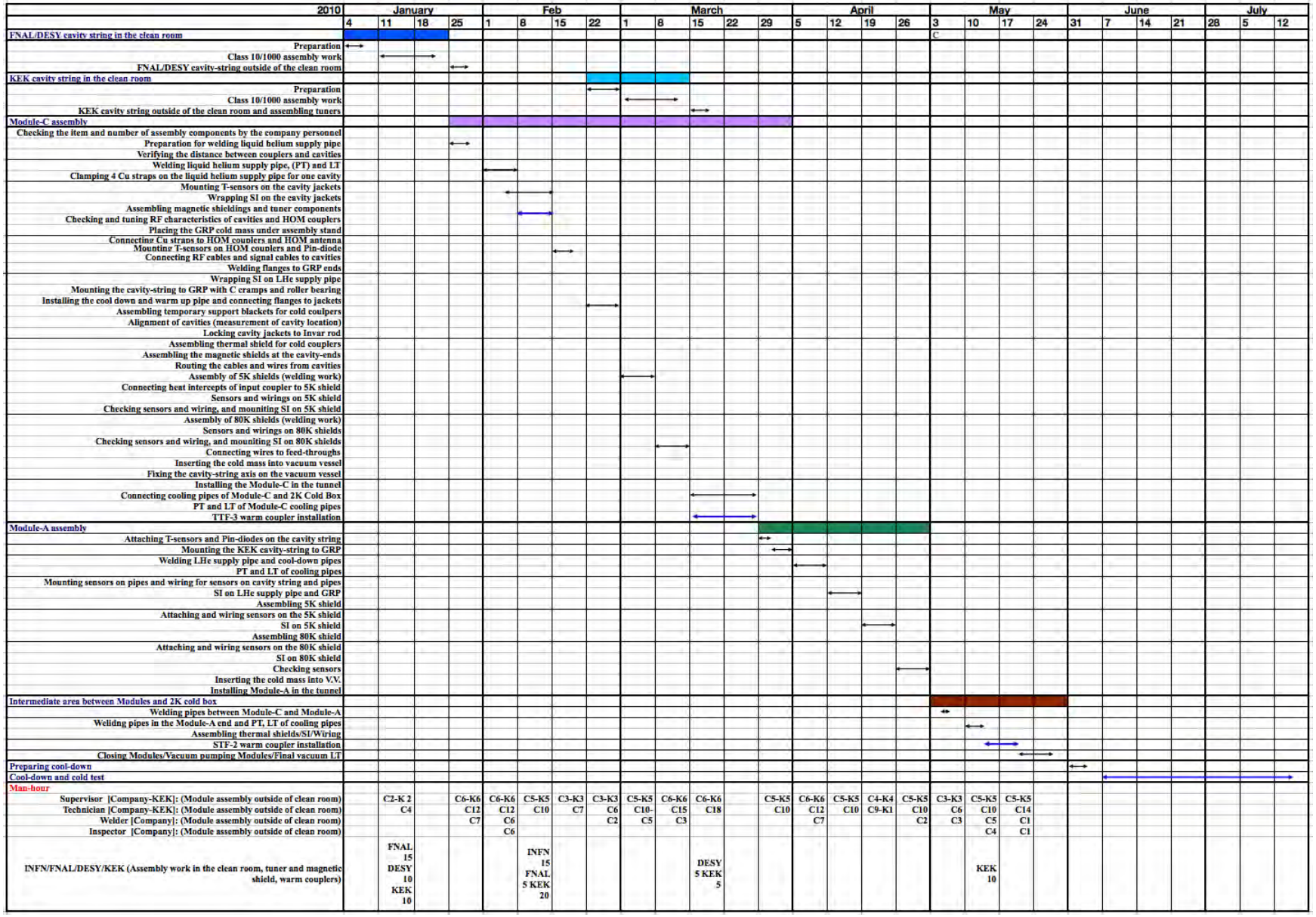

Figure 7-2: S1-Global cryomodule assembly schedule.

7.2 Cavity-string Assembly

7.2.1 Four Cavities for Module-C

The four-cavity string of the Module C was assembled by FNAL and DESY clean room technicians. The assembly was performed in a KEK STF clean room between 15 Jan and 20 Jan, 2010. FNAL and DESY clean room groups sent all the necessary components, hardware, and auxiliary fixtures needed for assembly to KEK. All of these parts were cleaned and bagged to Class 10 clean room standards at the respective laboratory clean rooms.

7.2.1.1 Pre-Assembly Observations

Before the FNAL and DESY assembly teams arrived at KEK, KEK colleagues completed the following tasks. The two FNAL and two DESY dressed cavities were staged on the clean room post fixtures in the Class-1000 area. The cavity exterior surfaces were wiped clean to Class 1000 cleanliness level. The cavities were roughly aligned (for rotational angle & X-Y positions). The necessary clean room assembly fixtures were fabricated and were present in the Class 1000 area.

During the initial review, it was observed that the cavity longitudinal orientation was offset by 180° compared to that of the NML and TTF beam line (this is coming from a requirement at STF). Figure 7-3 shows the KEK colleagues working on the FNAL and DESY cavities in the Class 1000 clean room prior to the arrival of the FNAL and DESY teams at KEK.

Figure 7-3 Preparation of cavities in Class 1000 clean room at KEK.

7.2.1.2 Cavity String Assembly steps

Step1: Gate Valve sub-assembly
Right angle valve and zero length reducer flange (non-cavity side)
Blank Flange (cavity side)
Step 2: Connection of DESY Z109 to Z108 cavity assembly
Step 3: Connection of FNAL TB9ACC011 to Step 2 assembly
Step 4: Connection of FNAL TB9AES004 to Step 3 assembly
Step 5: Connection of gate-valve sub-assembly to Step 4 assembly
String Assembly Complete

7.2.1.3 Assembly

15 Jan, 2010

The FNAL team moved the assembly components, tools, and hardware sent by FNAL into the Class 10 clean room. The FNAL team also assembled the pumping station lines so that the pumps could remain in the Class 1000 area and components could be pumped down in the Class 10 area during assembly. The DESY and FNAL teams began to move the gate valve and four cavities into the Class 10 area.

Workflow:
-Blow with ionized air/nitrogen & monitor the particle count (exterior surfaces)
-Gate valve was moved into the Class 10 clean room.
-Step-1 assembly was conducted
-The cavities were moved one at a time into the Class 10 clean room. This involved the following steps.
  -pump down
  -leak checks
  -backfilling with argon gas
  -movement of the cavity into position
  -cavity alignment

The gate valve transition piece was received in the afternoon; the KEK group cleaned and prepared it for entry into the Class 1000 area. Figure 7-4 shows some of the tasks completed on Jan. 15, 2010.

Figure 7-4a: DESY & FNAL clean room team at the KEK class 10 clean room preparing for string assembly.

Figure 7-4b: DESY clean room technician cleaning the gate valve with ionized nitrogen.

Figure 7-4c: FNAL clean room technician performing a pre-string assembly leak check on a cavity.

<u>16 Jan, 2010</u>
-The assembly team leak checked the Step-1 assembly (i.e., the gate valve sub-assembly).

-The transition piece, which was cleaned and brought into the clean room, was checked for pre-string assembly leaks.
-The DESY and FNAL clean room group continued to move the cavities into the Class 10 area.
-Due to the cavity valve configuration in the string caused by the longitudinal requirements of the cavities at STF, an auxiliary flange/valve needed to be at the downstream end of the string for purging during assembly. This part was sent from DESY to KEK via overnight delivery (a special thanks to Axel Matheisen for facilitating this). Figure 7-5 shows the tasks completed on Jan. 15, 2010.

Figure 7-5a: Gate valve sub-assembly (step-1) leak check.

Figure 7-5b: Transition piece leak check.

Figure 7-5c: Cavity moved into Class 10 area for string assembly.

<u>17 Jan, 2010</u>
Step 2 Assembly:

- The blind flange was removed from Z109 cavity (position #4) and the new flange/valve assembly sent by DESY was assembled.
- -The Z109 cavity was connected to the Z108 cavity (at position #3) with standard length interconnecting bellows.

Figure 7-6 shows the tasks completed on 17 Jan, 2010.

Figure 7-6a: Cavity Z109 assembled with the new flange/valve assembly at the beam pipe flange at the non coupler end of the string.

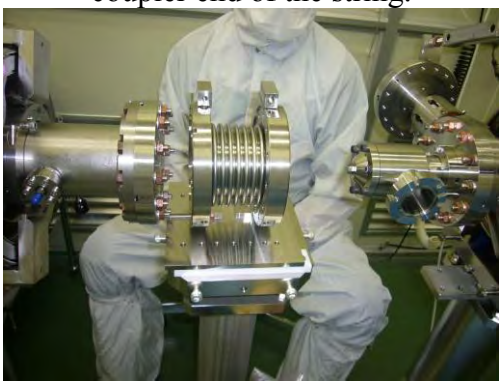

Figure 7-6b: 2 DESY cavities assembled into a string with interconnecting bellows.

Figure 7-6c: Assembly hardware and bellows cleaned and ready for assembly.

Figure 7-6d: DESY cavities aligned with the interconnecting bellows for string assembly.

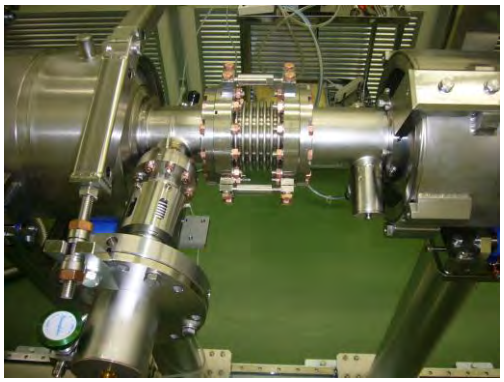

Figure 7-6e: 2 DESY cavities interconnected with bellows.

18 Jan, 2010

Step 3 Assembly:

-The TB9ACC011 cavity (position #2) was connected to the Step 2 assembly with interconnecting bellows (long length).

Step 4 Assembly:

-The TB9AES004 cavity (position #1) was connected to the Step 3 assembly with interconnecting bellows (standard length).

Figure 7-7 shows some of the tasks completed on Jan. 18, 2010.

Figure 7-7: FNAL Cavity TB9ACC011 assembled with DESY cavity Z109 with long interconnecting bellows.

19 Jan, 2010

Step 5 Assembly:

-The Step 1 assembly was connected to the Step 4 assembly, and the Gate Valve sub-assembly was connected to the already interconnected four cavities via a transition piece.

-Check coupler to coupler position.

-Vacuum pump down the string.

-A rough helium leak check was conducted.

-Active pumping was left to continue overnight.

Figure 7-8 shows some of the tasks completed on 19 Jan, 2010.

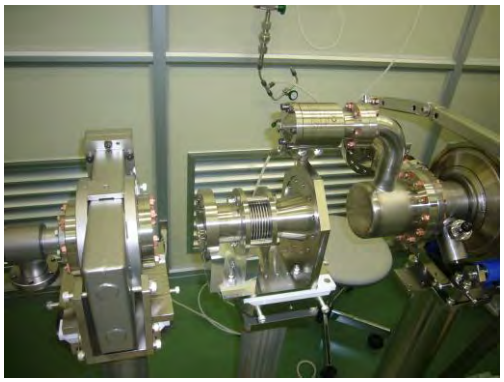

Figure 7-8a: Step-1 to Step-4 assembly with transition piece.

Figure 7-8b: Gate valve assembled with FNAL TB9AES-004 cavity via the transition piece.

20 Jan, 2010

The string was checked for helium leaks and backfilled to atmospheric pressure. This involved the following steps.

-Bag the bellows, cavity beam pipes, and couplers; fill with helium for fine leak check.

-A fine leak check was conducted.

-The string was backfilled with Argon gas (99.9999% from a cylinder, filtered) at a flow rate of 0.5 liter per minute.

Figure 7-9 shows the tasks completed on this day.

Figure 7-9: Fine leak checking of the assembled Module-C string.

7.2.1.4 Summary

The string assembly, as shown in Figure 7-10, proceeded as planned without any major problems**.** The FNAL & DESY clean room technicians are thanked for their excellent work. The KEK colleagues are also thanked for their support and help throughout the assembly process.

Figure 7-10: Completed S1-Global Module-C cavity string outside the clean room.

7.2.2 Four cavities for module-A

7.2.2.1 Cleaning Cavities and Support Posts

It is very important to clean the cavities before bringing them into a clean room. As shown in Figure 7-11, the outer surface of the cavities was rinsed with ultra-pure water at a high pressure of 8 MPa in a cleaning booth at the clean room entrance. Then, the outer surface of the cavity was carefully wiped with dust-free papers and alcohol inside the clean room. The cavity support-posts and input couplers were also cleaned using the same procedure used for the cavities. The support-posts were lined up in a row on the rails, as shown in Figure 7-12. Four cavities were placed on the support-posts for a rough cavity alignment in the class-1000 clean room. Final cleaning by ionized gasses was carried out and particle counter measurements performed prior to the equipment entering the class-10 clean room.

Figure 7-11: Cleaning booth at the entrance to the clean room (left) and cleaned cavity on a carrying cart inside the clean room (right).

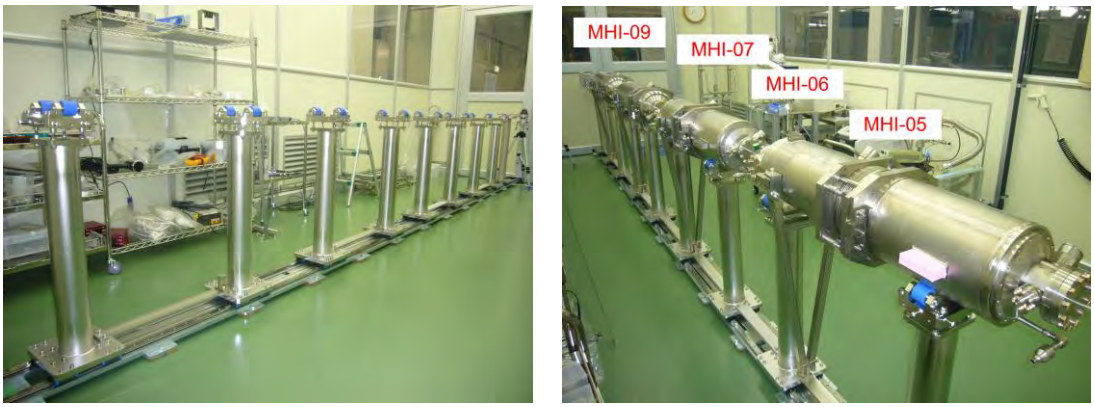

Figure 7-12: Preparation of cavity string assembly in the class-1000 clean room.

7.2.2.2 String Assembly in Class-10 Clean Room

Four cavities and four input couplers were set up in the class-10 clean room, as shown in Figure 7-13. The vacuum parts, such as the HOM feed-through, bellows for connecting between two cavities, beam tubes, and gate valves, were cleaned by rinsing with ultra-pure water and ultrasonic agitation. They were dried in the class-10 clean room. An input coupler with a cold window and two HOM feed-throughs with an RF antenna made of niobium are shown in Figure 7-14. The four cavity string assembly was carried out as follows.

- Feed-through with an antenna for HOM were installed by replacement from blank-off flanges.
- Four input couplers were installed in the cavities (see Figure 7-15).
- Two cavities were connected with a bellows beam tube (see Figure 7-15 and 7-16).
- A gate valve with a pumping duct was attached at one end (see Figure 7-16).
- After the completion of the cavity string (see Figure 7-17), pumping, leak checking, and filling of the cavities with Ar gas were carried out.

Figure 7-13: Preparation of cavity string assembly in class-10 clean room; four KEK cavities and four input couplers (left) and vacuum parts (right).

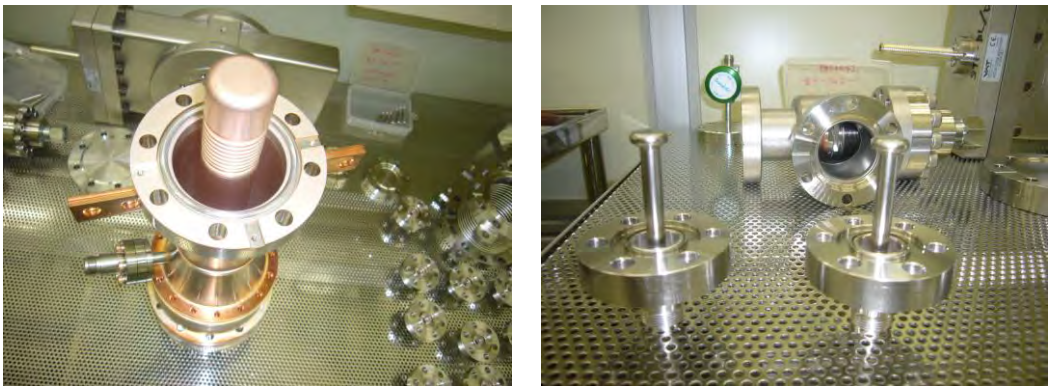

Figure 7-14: Input coupler with a cold window (left) and two HOM feed-throughs with an RF antenna (right).

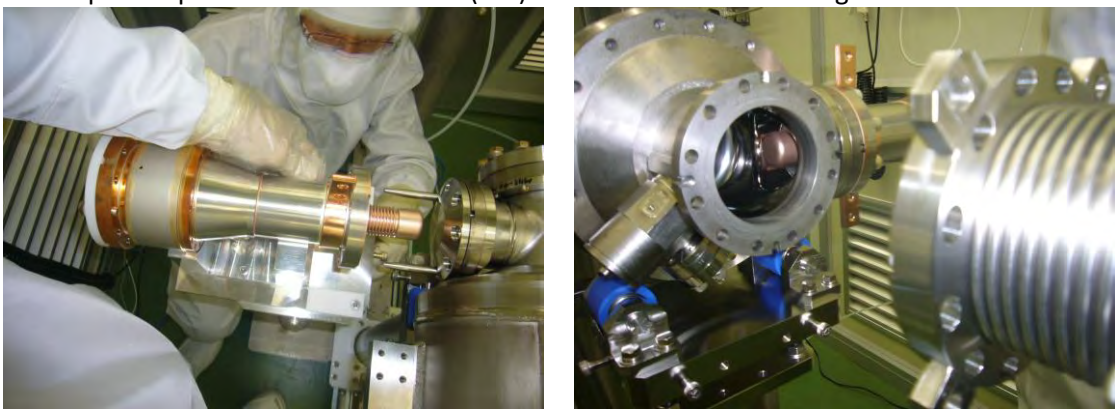

Figure 7-15: Installation of an input coupler (left) and connection of two cavities with a bellows beam tube (right).

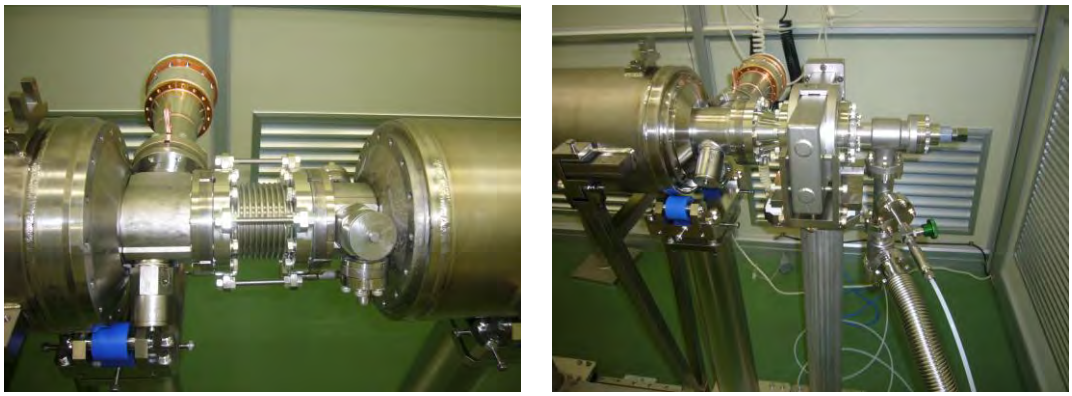

Figure 7-16: Two connected cavities (left) and an attached gate valve (right).

Figure 7-17: Completed string assembly of four KEK cavities in class-10 clean room.

7.2.2.3 Tuner Assembly and HOM Adjustment outside Clean Room

The four string cavities were moved outside the clean room, and a memorial photograph was taken that is shown in Figure 7-18. Two types of slide-jack tuner systems were mounted in the cavities: one was located in the center of the cavity and another at the end of the cavity (see Figure 7-19). RF measurements of parameters such as the cavity resonant frequency, the loaded Q value of an input coupler, and the external Q value of a monitor coupler were performed to confirm the cavity characteristics. The frequency shift caused by rotation of the tuner drive shaft was measured to check the tuning performance at room temperature. The notch frequencies of the HOM couplers to reject an accelerating mode were adjusted using a special tool.

Figure 7-18: Memorial photo of the four-cavity string and the STF staff.

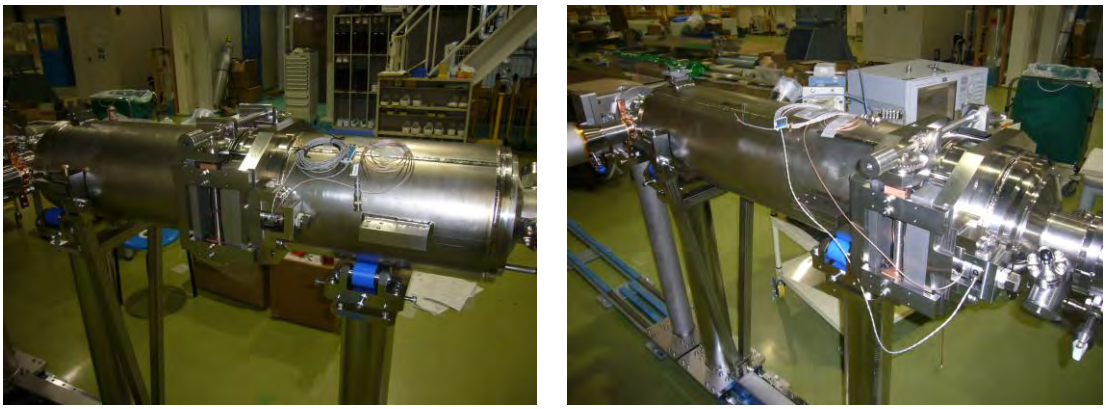

Figure 7-19: Slide-jack tuner system attachment to the cavity string (at the center and right of the left and right figures, respectively).

7.2.2.4 Suspending String Cavities under a He-GRP

The four-cavity string was moved under a He-GRP made of stainless steel, as shown in Figure 7-20. Four supporting tubs in each cavity were connected to the bars under the GRP for suspending the cavities, as shown in Figure7-21. The cavity support-posts were then removed, and the string cavities were completely suspended from the He-GRP.

Figure 7-20: Placement of string cavities under the He-GRP.

Figure 7-21: Attachment of movable supporting tubs for suspending the four cavities.

7.3 Cold Mass Assembly of Module-C

After moving the cavity-string out of the clean room, the cold mass was assembled from 25 Jan to 19 Mar, 2010. The main tasks completed during this period are described below.

1. Company personnel manually welded the Ti liquid helium (LHe) supply pipes between the cavity jackets with pipe reducers to accommodate the different supply pipe diameters of the DESY and FNAL jackets, which were 76.1 mm and 73.02 mm, respectively. To connect the Ti LHe supply pipes to the stainless steel cooling pipes from the 2 K cold box and Module-A, Ti-SUS junctions were welded at both ends of the LHe supply pipes, as shown in Figure 7-22. In the S1-Global cryomodule, we used Ti-SUS junctions that were manufactured by the hot iso-static pressing (HIP) method to reduce the risk of helium leakage at the flange connections. All junctions passed leak check tests in 2 K liquid helium before they were assembled into the cryomodule.

2. INFN and FNAL colleagues mounted the blade and Saclay tuners and magnetic shields from 9 Feb to 12 Feb. The cavity frequencies were tuned at atmospheric pressure to 1297.400 MHz $\pm$ 10 kHz for TB9AES004 and TB9ACC011, 1297.346 MHz $\pm$ 10 kHz for Z108, and 1297.349 MHz $\pm$ 10 kHz for Z109. Assembly of the magnetic shield on the FNAL cavity jacket is shown in Figure 7-23.

3. The FNAL/DESY cavity string was attached to the gas return pipe with C-clamps, as shown in Figure 7-24. The springs in the C-clamps were compressed with a torque to 6 Nm minus 1/4 turn back in the vertical screws, and to 6 N m minus 3/4 turns back in the horizontal screws. The turn back process was required to accommodate the different thermal contraction of the Ti jackets and the stainless steel components, such as the gas return pipe and the C-clamps. After mounting the cavity-string under the gas return pipe, the magnetic shields were assembled to bridge the cavities, as shown in Figure 7-25.

4. The cool-down pipe was installed and connected to the branch pipes of the cavity jackets. After connecting the four pipes, the FNAL/DESY cavity jackets were locked to the Invar rod.

5. While the upper sections of the 5 K thermal radiation shield had been connected to the gas return pipe and the support posts in Italy before delivery to KEK, the next step at STF involved the assembly and welding of the lower shield parts to the upper sections followed by the wrapping of 10 layers of super insulation (SI) around the shield. The welding process of the 5 K shield is shown in Figure 7-26.

6. The 80 K thermal radiation shields were assembled and welded, and surrounded by 30 layers of SI.

7. The cold mass was inserted into the vacuum vessel while being supported by two movable stands, i.e., one at each end of the gas return pipe, as shown in Figure 7-27. After the process, the cylindrical support posts were assembled on the gas return pipe, and the cold mass was aligned with the axis of the vacuum vessel. The alignment was performed using both a level scope and a theodolite scope to a tolerance of ±0.2 mm.

8. After lowering Module-C down into the STF tunnel, four TTF-III warm couplers were assembled by a DESY colleague from Mar. 16 and 19 in the local clean room.

9. Finally, 106 thermal sensors, 5 wire position monitors, 24 strain gauges, and 24 pin diodes were installed in Module-C.

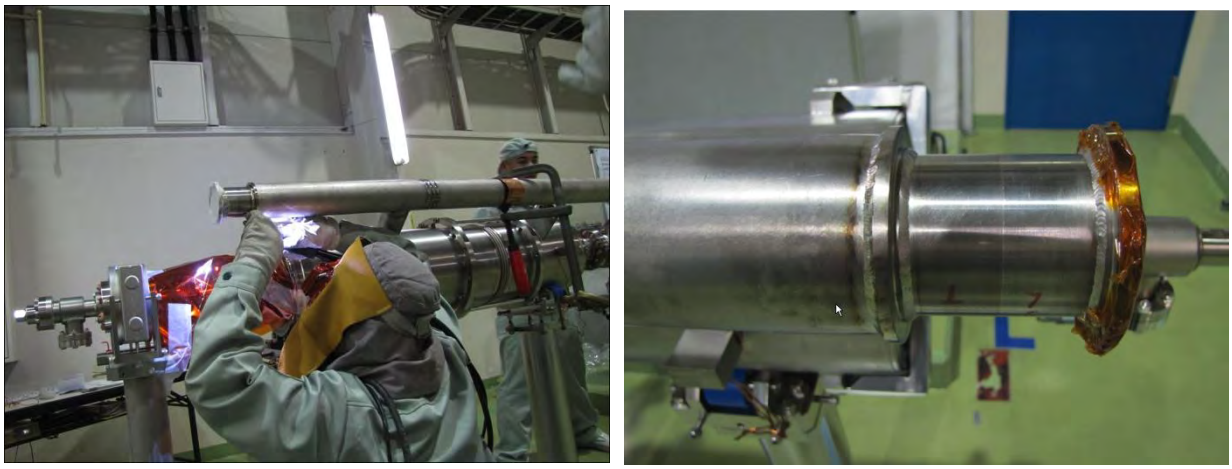

Figure 7-22: Staff member welding a Ti-SUS junction to the 2 K LHe supply pipe (left) and a Ti-SUS junction (right).

Figure7-23: Staff member assembling the magnetic shield on the FNAL cavity jacket.

Figure 7-24: Attachment of the cavity-string to the GRP.

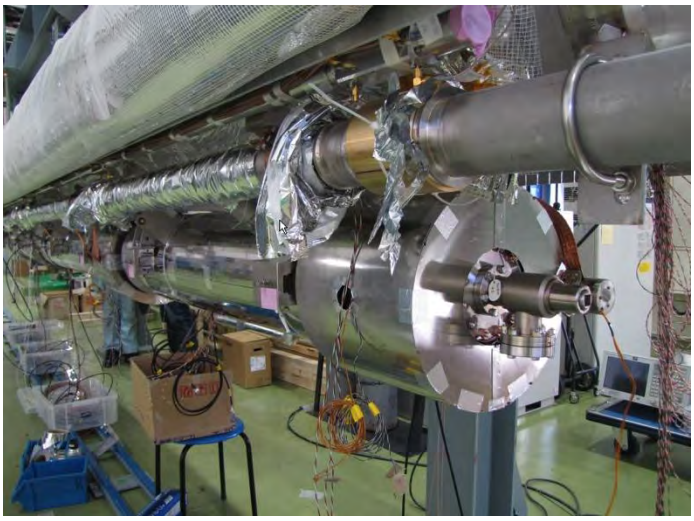

Figure 7-25: Completed magnetic shield on the FNAL/DESY cavities.

Figure 7-26: Staff member welding the lower 5 K shield to the upper shield.

Figure 7-27: Staff member inserting the Module-C cold mass into the cryostat.

7.4 Cold Mass Assembly of Module-A

The cold mass assembly of Module-A followed the same procedure as Module-C, except for the following changes that were driven by design differences.

1. The magnetic shields of the KEK cavities are located inside the cavity jackets, and hence, this assembly step was not needed. Five layers of SI were wrapped around the four cavity jackets.

2. The LHe supply pipes for the KEK cavities were welded into a pipe, but this assembly was not welded to the cross connect pipes of the cavity jackets when the cavity string was mounted under the gas return pipe. Instead, Ti-SUS junctions were used to connect the cavity jacket and the LHe supply pipe, as shown in Figure 7-28. The welding of the Ti-SUS junctions was performed after a rough alignment of the four cavities.

3. The upper and lower Al sections of the 5 K and 80 K thermal radiation shields were thermally linked with screws, as shown in Figure 7-29.

4. 103 thermal sensors, 13 wire position monitors, 24 strain gauges, and 24 pin diodes were installed in Module-A.

Figure 7-28: The cross connect pipe between the KEK cavity jacket and LHe supply pipe. A Ti-SUS junction pipe was used as the cross connect pipe. The two stainless steel bellow pipes were connected to this pipe.

Figure 7-29: Connection of the lower and upper thermal shield components with screws.

7.5 Completing the S1-Global Cryomodule and Installing it into the STF Tunnel

Transportation of the two cryomodules down to the STF tunnel was completed on 28 Apr, as shown in Figure 7-30. Because the sizes of the cooling pipes in the two modules are different, pipe reducers were made for the connections. The aluminum pipes between the thermal shields of two modules were designed in a snake pattern, as shown in Figure 7-31, in order to accommodate thermal shrinkage. The connection

pipes for the gas return pipes and the LHe supply pipes had stainless steel bellows to allow for the thermal contraction of these pipes.

The connection methods used for the vacuum flanges of Module-C and Module-A were different. Claw clamps were used for Module-C, and bolts and nuts for Module-A, as shown in Figure 7-32. For the interconnection, a short pipe with a flange of each type was prepared.

The actual man-days spent on the assembly of the two cryomodules are described in Figure 7-2. It required 293 man-days to assemble Module-C, and 191 to assemble Module-A.

Figure 7-30: Placing Module-C and Module-A into the KEK-STF tunnel.

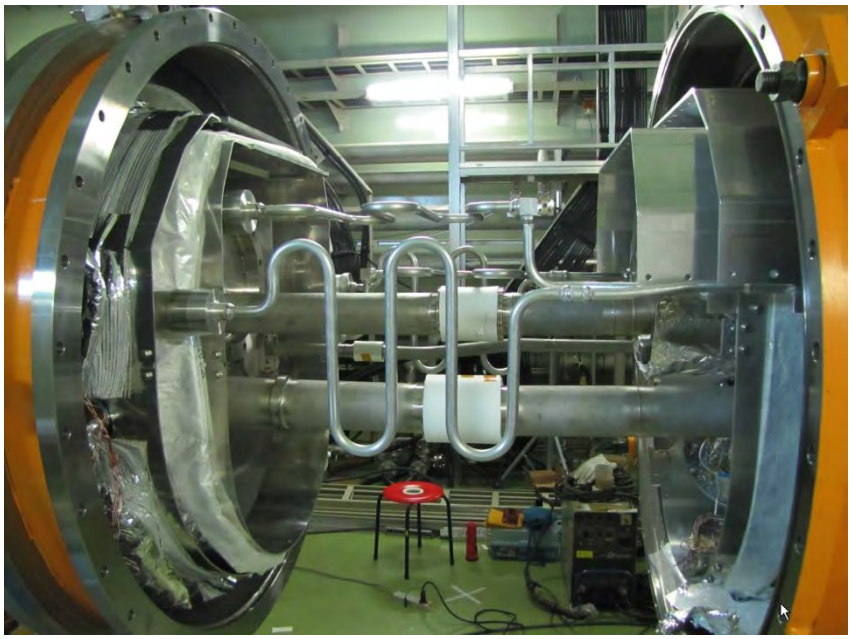

Figure 7-31: Connection between the cooling pipes of Module-C and Module-A.

Figure 7-32: Connection of Module-C to Module-A.

8 Thermal performance of Cryogenic System and Cryomodules

8.1 Two-Kelvin (2 K) Cryogenic System at STF

The operating temperature of the superconducting RF cavities for the ILC is 2 K. The simplest way to produce the temperature of 2 K is to evacuate the liquid helium, using a method called "forced-flow boiling." Figure 8-1 shows the phase diagram of helium. Helium has two liquid phases. The first is an ordinary liquid phase, which is designated as He I. The second is a superfluid liquid phase, which is designated as He II. The He I domain is located at the higher temperature side of the liquid phase, as shown in Figure 8-1, while the He II domain is located at the lower temperature side. These two liquid phases are separated by the "λ-line" (a green line in the figure). This λ-line meets the saturated vapor pressure curve (saturation curve) at 2.17 K. This point in the phase diagram is called the "(lower) λ-point." Generally speaking, liquid helium is transferred from a liquefied helium storage vessel to cryostats of superconducting RF cavities by a pressure difference. If the pressure difference is 0.03 MPa, the saturation temperature of helium is 4.5 K (with an absolute pressure of 0.13 MPa in this case). If this liquid helium is evacuated with any type of vacuum pumps, the thermodynamic state of helium varies along the saturation curve (a red curve in the figure), as shown by the blue arrow in the Figure 8-1. If the evacuation capacity of the vacuum pumps is sufficient, superfluid helium can be achieved at 2 K or lower.

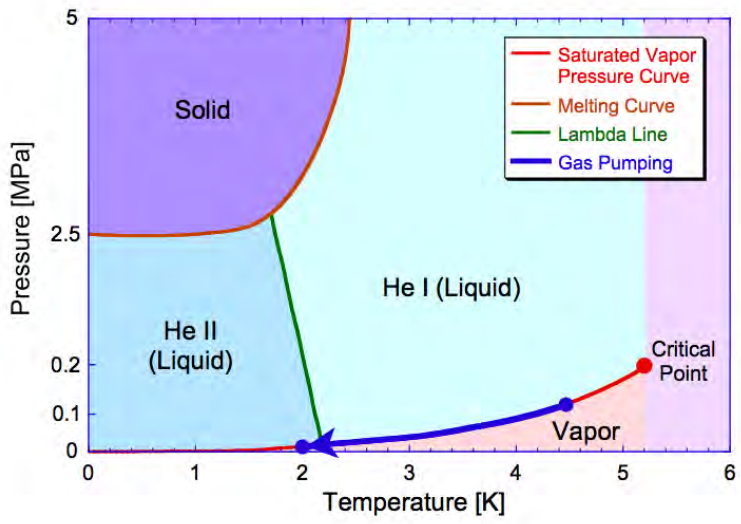

Figure 8-1: Phase diagram of helium.

A 2 K cryogenic system for the S1-Global is schematically illustrated in Figure 8-2. The system consists of various devices: a helium liquefier/refrigerator, a liquefied helium storage vessel, a 2 K refrigerator cold box, a superconducting RF cavity cryomodule, a helium gas pumping system, and high-performance transfer lines. Liquid helium is produced with a helium liquefier/refrigerator and is then stored in a liquefied helium storage vessel. The 2 K refrigerator cold box contains a He I pot, a He II pot, a heat exchanger, and a Joule-Thomson (J-T) valve. Liquid helium is transferred from the storage vessel to the He I pot of the 2 K refrigerator cold box through the high-performance transfer lines. These transfer lines are designed and fabricated to reduce the heat load from the room-temperature environment as much as possible, and their

cross-section is shown in Figure 8-3. Because the main transfer line is employed to transfer not only liquid helium but also cold helium return gas and liquid nitrogen, the transfer line is also called a “multi-channel transfer line.” Liquid helium in the He I pot of the 2 K refrigerator cold box is transferred and distributed into the He II pot, precooling line of the superconducting cavity, and the 5 K thermal shield of the cryomodule. As there are no valves in the cryomodules, the liquid helium level in the cryomodules is the same as in the He II pot of the 2 K refrigerator cold box. After filling up the He II pot and the cryomodules with liquid helium, we start to evacuate gradually through a gas return pipe (GRP) and the heat exchanger with several oil rotary vacuum pumps and mechanical booster pumps until 3.2 kPa, which is the saturation pressure of helium at 2 K. After 2 K superfluid helium is produced in the He II pot and the cryomodule, liquid helium in the He I pot is sent to the He II pot through the heat exchanger and the liquid helium is then cooled by the helium gas evaporated from the 2 K superfluid helium. The cooled liquid helium is then expanded through the Joule-Thomson valve and is later converted into superfluid helium at 2 K.

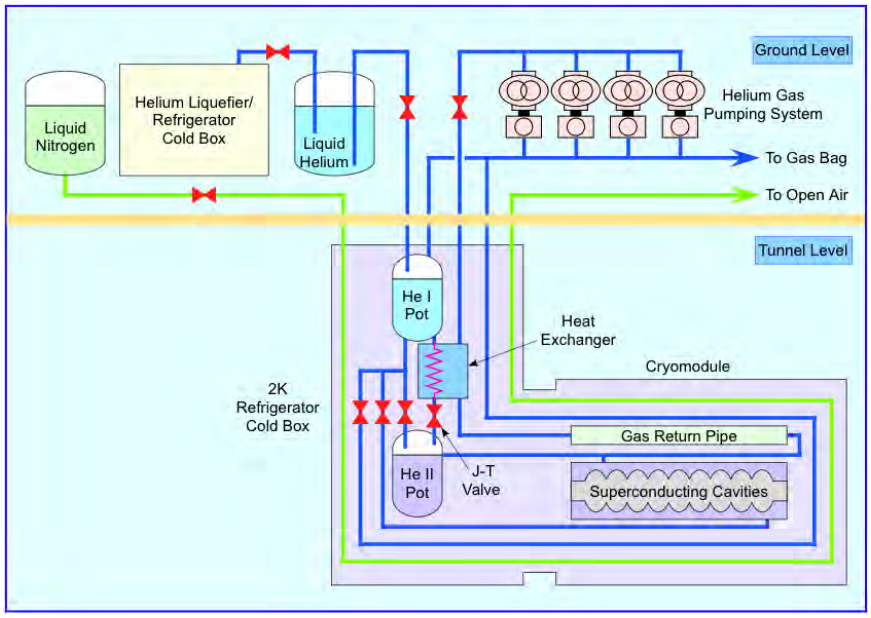

Figure 8-2: Schematic diagram of 2 K cryogenic system for S1-Global.

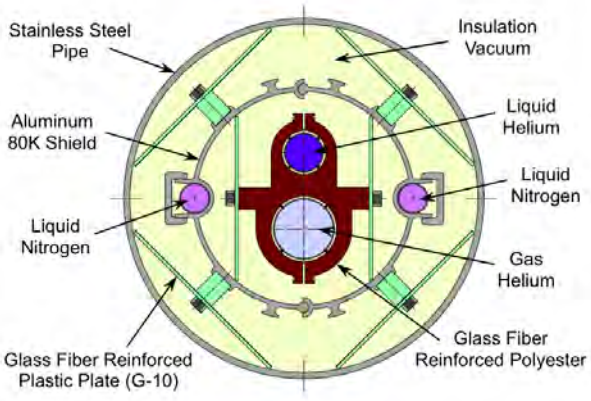

Figure 8-3: Cross-section of high-performance transfer line (MLI not shown).

A helium liquefier/refrigerator had been moved to the STF to supply liquid helium and liquid nitrogen to the superconducting RF cavity and cryomodules. Prototypes of a 2 K refrigerator cold box and high-performance transfer lines were designed and fabricated for tests of cavity and cryomodules for the ILC some years ago at the STF. Figure 8-4 shows the layout of the cryogenic system at the STF. The STF building has two stories, i.e., the ground level and the tunnel level, which is 10m below the ground level. The helium liquefier/refrigerator, liquefied helium storage vessel, and helium gas pumping system (oil rotary vacuum pumps and mechanical booster pumps) are located on the ground level. The 2 K refrigerator cold box and cryomodules are on the tunnel level. The multi-channel high-performance transfer line is installed from the ground level to the tunnel level through a shaft between the two levels.

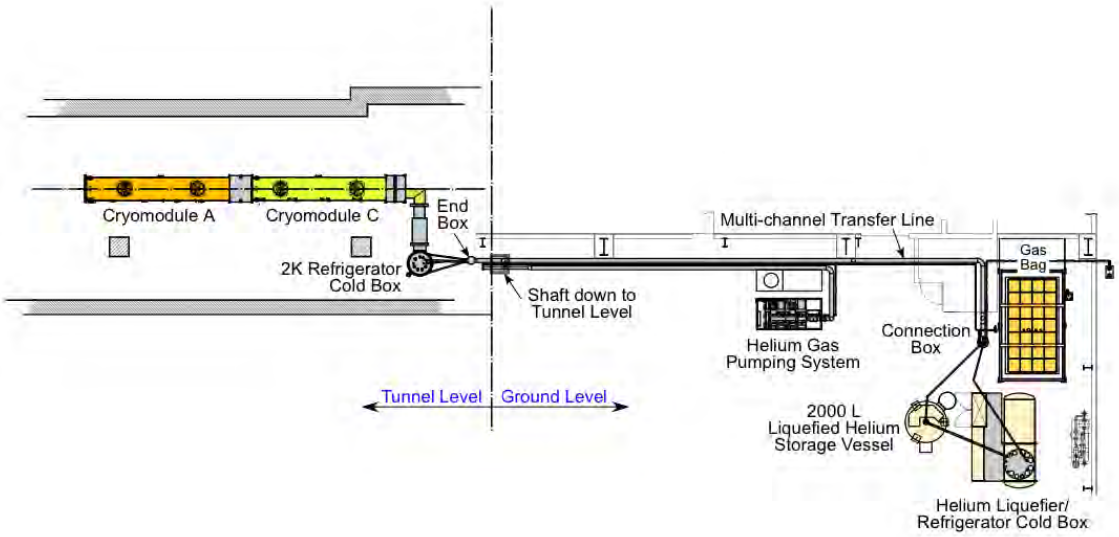

Figure 8-4: Cryogenic system at STF.

8.2 Upgrade of Cryogenic System for S1-Global

The S1-Global configuration consisted of eight cavities in two cryomodules, i.e., four cavities in each cryomodule. This was a larger number of cavities than previously tested. Although the 2 K cryogenic system was designed to produce 30 W cooling capacity at 2 K, the stable operation of the cryogenic system depended on the static heat load from the cryomodules and on the dynamic heat load from the superconducting RF cavities. To prepare for an increase in heat load due to the further addition of cavities, we employed additional vacuum pumps to increase the cooling capacity of the cryogenic system. A PC-aided small-scale control and data acquisition system was introduced into the cryogenic system before the S1-Global tests to assist with the long-term operation of the cryogenic system. This control and data acquisition system can control valve openings in the helium gas pumping system in response to signals from pressure transducers to facilitate the stable operation of the cryogenic system, i.e., the maintenance of a constant temperature superfluid helium and the acquisition of temperatures, pressures, and liquid helium levels in the cryogenic system. The acquired data are sent to the main PC of the STF through the Ethernet for data storage. This system consists of commercially available devices: a data-logger unit, various terminal units, a control valve, and a laptop PC. Because there are no special devices in this system, we can easily extend, replace, and modify this control and data acquisition system in response to modifications to the cryogenic system.

8.3 Operation of Cryogenic System

Because the production and consumption of liquefied gas (such as liquid helium and liquid nitrogen) are subject to the High Pressure Gas Safety Act in Japan, a supervisory safety worker that has an authorized license (a high pressure gas production safety management certificate) should be on duty whenever the cryogenic system is in operation (in particular the helium circulation compressors). The S1-Global test was not a full-scale operation of the accelerator as defined in the High Pressure Gas Safety Act (i.e., it was a short term test or experiment of scientific instrumentation in an open cryogenic system). The operation of the cryogenic system was therefore restricted on a day-by-day basis, not continuous full operation. We began to cool down the cryomodules each morning and stopped in the evening. On Saturdays and Sundays the cryogenic system was not operated. A supply of liquefied nitrogen to the 80 K thermal shields is part of the allowed operation of the cryogenic system. However, this was not allowed in the absence of a supervisory safety worker during nights and weekends.

The principal cold mass of the cryomodule is the GRPs, and not the superconducting RF cavities. This is because the pipe is made of stainless steel and has thick walls, is long, and has a large diameter. The cavities could be cooled down easily, because they are in direct contact with the liquid helium and superfluid helium, while the GRPs could only be cooled down with cold helium gas from the helium vessels of the superconducting RF cavities. During nights and weekends when the cool-down was suspended, the cavities and their helium vessels were gradually warmed up, while the GRPs cooled down. The opposite phenomenon was observed when the cryomodules warmed up after testing.

Because a rapid cool-down may cause vacuum leaks in the superconducting RF cavities and/or excess deformation of the cryomodule structure, the cool-down was intentionally carried out slowly. It was estimated that it would take almost 2 weeks (10 working days) to complete the cool-down of the eight superconducting RF cavities from room temperature to 2 K. To cool from room temperature to about 200 K, we supplied cold helium gas, which was cooled with liquid nitrogen, to the precooling line, the 2 K line, and to the 5 K thermal shield line. The 80 K thermal shield line was supplied with liquid nitrogen. It required three workdays for the temperature of the helium vessels of the cavities to reach about 200 K. Beginning on the 4^{th} workday, liquid helium was supplied to the 2 K line and the 5 K thermal shield line. Liquid nitrogen was supplied to the 80 K thermal shield line. On the 9^{th} workday liquid helium filled the helium vessel of the first cryomodule, and all helium vessels were filled with liquid helium on the 10^{th} workday. On the 10^{th} day, the helium gas pumping system was activated for a number of hours to decrease the temperature of the GRPs and the cavities. On the subsequent Monday, we resupplied liquid helium to the 2 K refrigerator cold box and the cryomodules and evacuated it until the temperature decreased to 2 K.

A typical temperature evolution of the eight helium vessels of the cavities in the two cryomodules during cool-down is shown in Figure 8-5, and that of the two GRPs is shown in Figure 8-6. The gray strips in these figures indicate weekends. Because the C-1 cavity (and therefore, the helium vessel of C-1) was located the furthest upstream, that is, the closest to the 2 K refrigerator cold box, its temperature reduced first. The temperatures of the individual helium vessels decreased according to their respective positions from the 2 K refrigerator cold box. Because of the day-by-day operation of the cryogenic system, the temperature evolution in the figure follows a zigzag pattern. After the cryomodules were cooled down to 2 K, their temperature increased slightly during the nights and significantly more during weekends. Hence, on Mondays it required almost one day to resupply liquid helium to each of the helium vessels and to evacuate the liquid helium in the vessels until the temperature reached 2 K. On other weekdays the superconducting cavities became stable at 2 K by noon, and tests on the cavities and RF systems could be carried out in the

afternoons. Cold helium gas flowed from the downstream end of the GRP of cryomodule A (CM-A) to the upstream end of the GRP of cryomodule C (CM-C), because the 2 K helium supply line was connected to the downstream end of the GRP of CM-A. Hence, the downstream end of the GRP of CM-A was cooled down first, as shown in Figure 8-6.

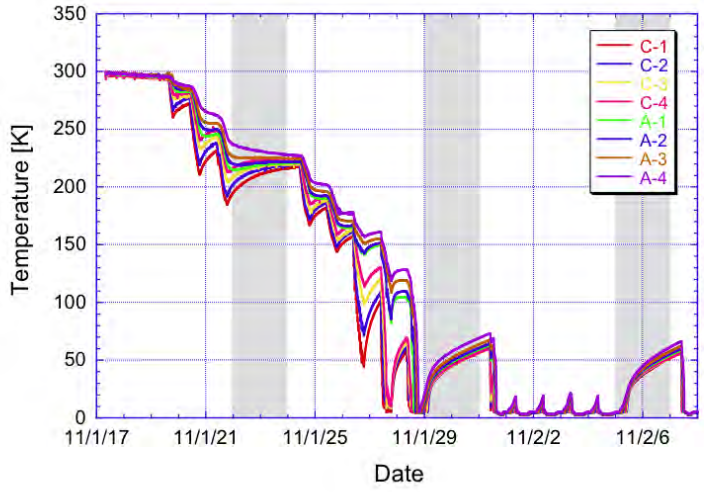

Figure 8-5: Temperature evolution of the eight liquid helium vessels of S1-Global during cool-down. The dates along the x-axis are in the form year/month/day.

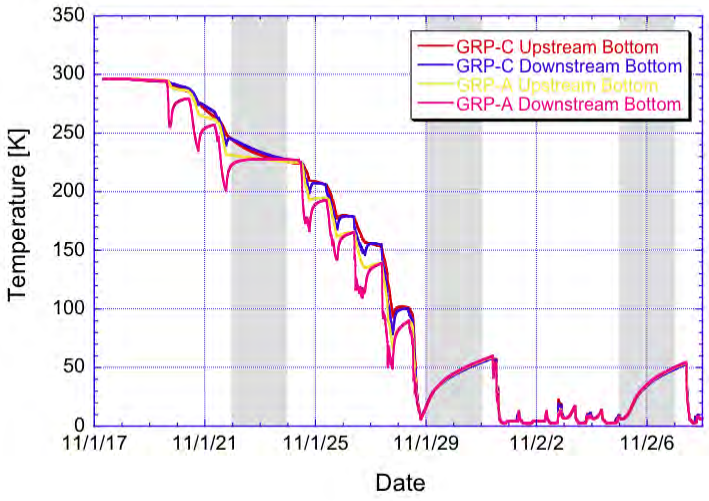

Figure 8-6: Temperature evolution of the two gas return pipes (GRPs) of S1-Global during cool-down. The dates along the x-axis are in the form year/month/day.

The temperature evolution during the unattended warming up of the helium vessels is shown in Figure 8-7. In contrast to the cool-down process, the temperature evolution of helium vessels during heating is not simple. In CM-A the A-4 helium vessel, which was located the furthest downstream, was the first to begin warming up. Then A-3, A-2, and A-1 followed in order of their respective positions in the module. However,

in CM-C, C-1, which was the furthest upstream, warmed up first, followed by C-2, C-3, and C-4 in the order of their respective positions in the module. This means that there are two heat flow paths to the superconducting RF cavities and their helium vessels, i.e., heat flows into the cavity string from both ends of the string. The temperature evolution of the GRPs, shown in Figure 8-8, is rather uniform during the free warming up. This is because the GRPs are the largest cold mass in the cryomodules and their heat capacity is therefore large.

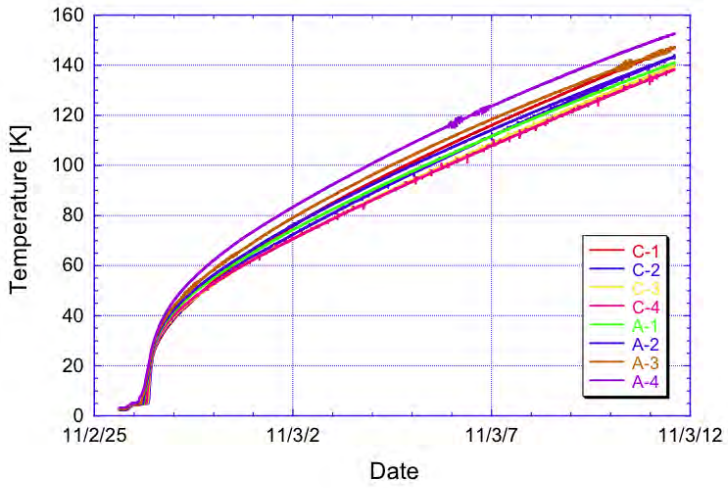

Figure 8-7: Temperature evolution of the eight liquid helium vessels of S1-Global during warming. The dates along the x-axis are in the form year/month/day.

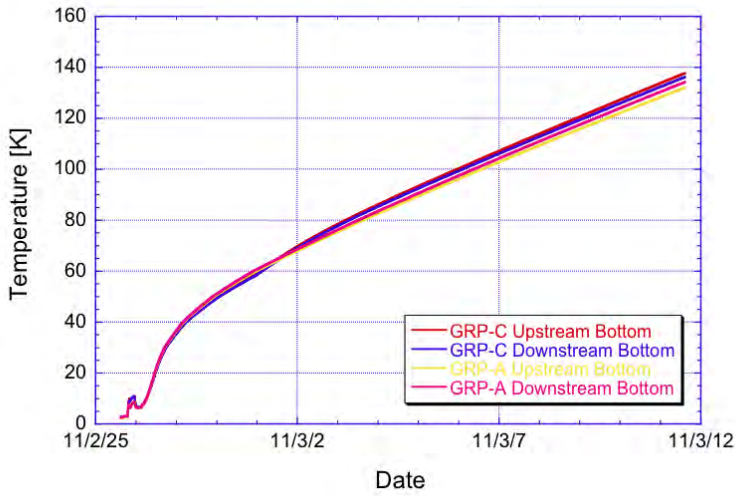

Figure 8-8: Temperature evolution of the two gas return pipes (GRPs) of S1-Global during warming. The dates along the x-axis are in the form year/month/day.

8.4 Summary of Cryogenics Operation

From Jun. 2010 to Feb. 2011, cryogenic tests of the S1-Global superconducting RF cavities were carried out intermittently. The 2 K cryogenic system worked well and stably with the help of the small-scale, PC-aided control and data acquisition system. It required two weeks (10 working days) to cool the eight superconducting RF cavities in the two cryomodules down to 2 K, as the cool-down was planned to occur gradually. It was confirmed that the cooling capacity of the cryogenic system with the build-up helium gas pumping system met the specification of maintaining the eight cavities in a superconducting state at 2 K.

8.5 Thermal Performance of the Cryomodule

The S1-Global cryomodule [8-1, 8-2] consists of two 6-m cryomodules. One module was designed by INFN, and it contained two cavities designed by FNAL and two cavities designed by DESY. Most of the associated components, such as the input couplers and RF cables, were the same as those used in the TTF-III cryomodule [8-3]. The other module was designed by KEK, and contains four cavities also designed by KEK. As one of the important studies of the S1-Global program, measurements and comparisons of the thermal performances of these cold components had been proposed. The static heat load and the temperature profiles of the cold components were measured and they were evaluated with respect to the designed values. The dynamic losses of the DESY, FNAL, and two KEK cavities at their maximum operative gradients were obtained by the evaporation of liquid helium (LHe) at 2 K and the Q_0 values were evaluated. The dynamic losses of input couplers were measured at the same power level corresponding to the resonant operation at the ILC nominal gradient of 32 MV/m when the cavities were detuned. These measured data will become important references for the ILC cryomodule and cryogenic design.

8.5.1 Thermal Design of Cryomodule

The parameters of Module-A and Module-C in the S1-Global cryomodule are listed in Table 8-1. The total length of the S1-Global cryomodule including the end cans was 14.9 m. The design of the Module-A and C cross-sections was based on the TTF- III cryomodule.

The calculated static heat loads of the components are listed in Table 8-2. The cold components were thermally intercepted with two thermal shields at 5 K and 80 K. The heat loads are calculated using the temperature profiles. In Table 8-2, the STF-2 input coupler has a larger static loss than the TTF-III coupler at each temperature level. This is due to the design of the STF-2 coupler, which was altered in order to simplify its assembly and therefore has no bellows between the thermal intercepts at 5 K and 70 K.

Table 8-1: S1-Global cryomodule thermal parameters.

	Module-A by KEK	Module-C by INFN
Vacuum vessel length	6087 mm	5800 mm
Vacuum vessel O.D.	ϕ 965.2 mm	ϕ 965.2 mm
5 K shield cold mass [Al]	185 kg	167 kg
80 K shield cold mass [Al]	210 kg	182 kg
Gas return pipe O.D.	ϕ 318.5 mm	ϕ 312.0 mm
Cavity package	KEK-a/KEK-b	FNAL/DESY
Input coupler	STF-2 type	TTF-III type

Table 8-2: Designed Static Head Load of Module-A and Module-C.

	Cold component	Module-A, [W]	Module-C, [W]
2 K	Thermal radiation	~0.0	~0.0
	4 input couplers	0.29	0.08
	HOM RF, piezo cables	2.1	0.71
	4 tuner driving shafts	0.48	NA
	Temp. sensor wires	0.18	0.18
	WPM, Pin diodes wires	1.72	0.82
	WPM connection pipe	0.17	~0.0
	2 support posts	0.25	0.25
	Beam pipe	0.02	<0.01
	Total	5.2	2.1
5 K	Thermal radiation	0.66	0.68
	4 input couplers	4.00	0.92
	2 support posts	1.54	1.54
	Beam pipe	0.1	0.05
	Sensor wires	0.9	0.9
	Total	7.2	4.1
80 K	Thermal radiation	16.6	15.9
	4 input couplers	9.60	7.28
	2 support posts	10.78	10.78
	RF cables	6.88	1.30
	Beam pipe	0.37	0.10
	Sensor wires	0.08	0.08
	Total	44.3	35.3

8.5.2 Static Thermal Measurement

The static heat loads at 2 K, 5 K, and 80 K were measured by calorimetric methods. The heat load at 2 K was evaluated by measuring the flow rate of evaporated LHe in the eight cavity vessels. The flow rate was measured at the outlet of the pump unit at room temperature. The heat loads at 5 K and 80 K were calculated by measuring the temperature rises of the thermal shield plates by stopping the LHe and LN_2 flow.

Figure 8-9 shows the thermal conditions of the static heat load measurements at 2 K. The flow rate of evaporated LHe was 6.87 m^3/h, which corresponds to 0.314 g/s. The helium pressure was controlled to be 3.14 kPa, and the latent heat of LHe was 23.045 J/g. Therefore, the heat load of the eight vessels was calculated to be 7.2 W. This measured heat load is in good agreement with the estimate given in Table 8-2, which corresponds to 6.8 W if we exclude the contribution of the support posts. The direct heat load from the support posts to the vessels via the gas return pipe is negligible, and its effect is to increase the enthalpy of the evaporated gas rather than to induce additional LHe losses.

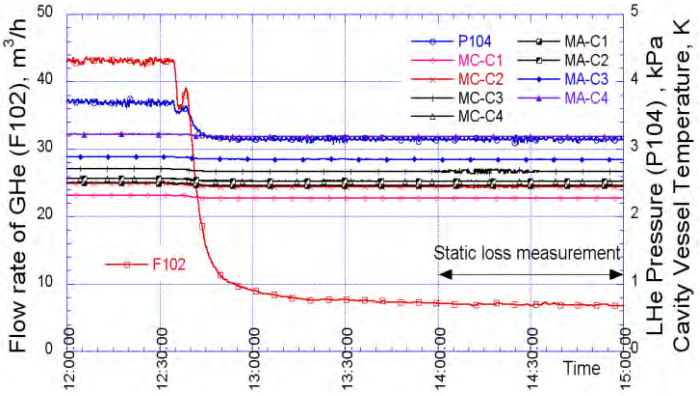

Figure 8-9: Static loss measurements: flow rate of He (F102), pressure of 2 K He (P104), and temperatures of the cavity vessels (MC-C1 to C4, MA-C1 to C4). Temperature sensors were attached to the vessel surfaces.

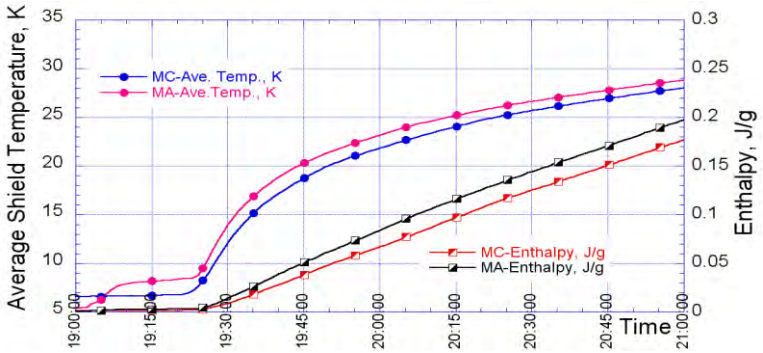

Figure 8-10: Temperature and enthalpy changes of 5 K shields of Module-A (MA) and Module-C (MC).

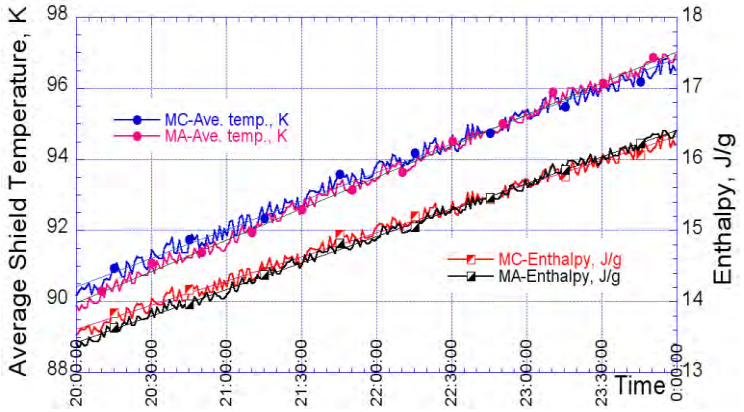

Figure 8-11: Temperature and enthalpy changes of 80 K shields of Module-A (MA) and Module-C (MC).

Figs. 8-9 and 8-11 show the temperature and enthalpy changes of the 5 K and 80 K shields with time. The temperature profiles of the 5 K and 80 K shields were measured by 15 PtCo thermometers and 13 Type-T thermocouples, respectively, for each Module. The plotted temperatures are the average of the measured values. The enthalpies of the shields were calculated from the average temperatures. The heat loads were calculated from the enthalpy increases of the shields, and the measured heat loads are listed in Table 8-3. The values in parentheses in Table 8-2 are calculated values. The measured and calculated values show good agreement.

Table 8-3: Measured static heat load.

	Module-A		Module-C	
2 K	7.2 W		[6.8 W]	
5 K	7.3 W	[7.2 W]	5.3 W	[4.1 W]
80 K	48.7 W	[44.3 W]	34.4 W	[35.3 W]

8.5.3 Dynamic Thermal Measurement

8.5.3.1 Dynamic Loss of a Single Cavity

In order to evaluate the dynamic loss and the Q_0 value at a single cavity, a sequence of four measurements was performed. They were measurements of the heat loss with a RF operation, i.e., Q_{D1}, the corresponding static loss, i.e., Q_{S1}, the heat loss at the same power level as the case of resonant operation in the detuned cavity, i.e., Q_{D2}, and the corresponding static heat loss, i.e., Q_{S2}. The dynamic losses at the RF operation and the detuned condition, Q_D and $Q_{D\text{-}det}$, were calculated as follows: $Q_D = Q_{D1} - Q_{S1}$ and $Q_{D\text{-}det} = Q_{D2} - Q_{S2}$. The heat loss of Q_D includes the dynamic losses at the cavities and couplers. $Q_{D\text{-}det}$ corresponds to the heat loss at the input couplers. The dynamic loss at the cavity can be calculated by $Q_{D\text{-}cav} = Q_D - Q_{D\text{-}det}$.

The dynamic loss measurement for the DESY cavity (Z109) is shown in Figure 8-12. The cavity was operated at a field gradient of 28 MV/m. The measured Q_D and $Q_{D\text{-}det}$ were 0.84 W and 0.09 W, respectively, which were calculated from the flow rate of evaporated LHe. The dynamic loss at the cavity, $Q_{D\text{-}cav}$, was calculated to be 0.75 W, which corresponds to a Q_0 value of 8.8×10^9. The measured values for the other cavities are listed in Table 8-4.

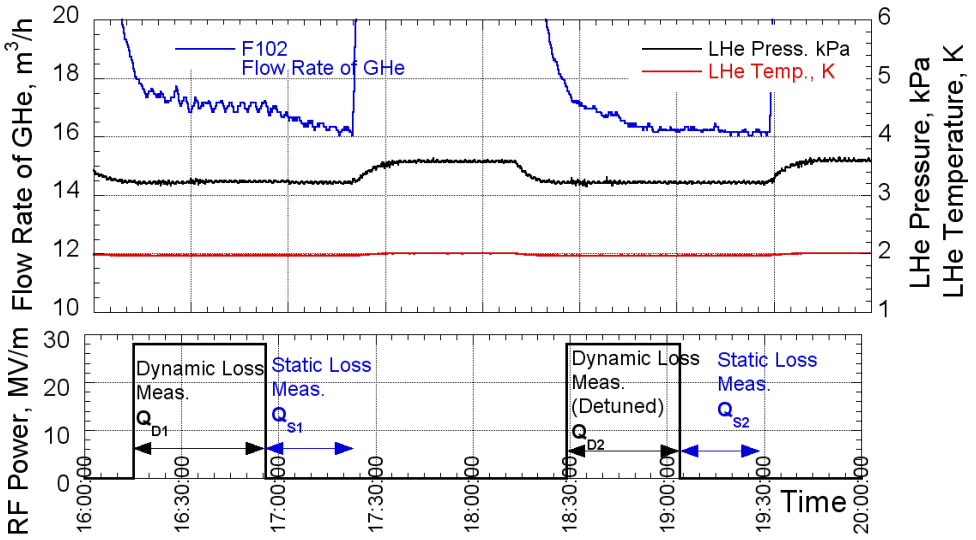

Figure 8-12: Thermal conditions of the dynamic loss measurement.

Table 8-4: Measured dynamic loss of single cavities.

	MC-4 Z109	MC-1 TB9AES004	MA-3 MHI07	MA-2 MHI06	MA-2 MHI06
G, [MV/m]	28	25.2	32.3	38	32
Q_D, [W]	0.84	1.4	2.8	4.8	2.6
$Q_{D\text{-}det}$, [W]	0.09	0.18	0.7	1.8	1.2
$Q_{D\text{-}cav}$, [W]	0.75	1.3	2.0	2.9	1.3
Q_0	8.8×10^9	4.3×10^9	4.3×10^9	4.2×10^9	6.5×10^9

8.5.3.2 Dynamic Loss of Four and Seven Cavities

Dynamic loss measurements were performed with a string of four and seven cavities. The measured losses and the average field gradient of the cavities, G_{ave}, are listed in Table 8-5. Four cavities in Module-C and Module-A were operated at G_{ave} =20 MV/m and 26.0 MV/m, respectively, and the losses of $Q_{D\text{-}cav}$ were 2.5 W and 4.4 W. Because there were difficulties with the frequency tuner in one of the Module-C cavities, the eight cavities could not be operated simultaneously. The dynamic loss with seven cavities operating was measured to be G_{ave} =25.4 MV/m, and $Q_{D\text{-}cav}$ was found to be 7.0 W.

In order to estimate the heat loss of the input couplers at the ILC nominal gradient, four cavities in each module were detuned and operated at a power level of 32 MV/m. The losses of $Q_{D\text{-}det}$ of Module-C and A were 0.5 W and 4.6 W, respectively. The design of one TTF-III coupler is 0.06 W [8-4], and the measured loss of 0.5 W for four couplers is consistent with this estimation. The loss of the STF-2 couplers [8-5] was found to be 4.6 W, and this loss was consistent with the single cavity measurement of MHI06. From the

temperature measurements, temperature rises were found at the connection flanges between the STF-2 couplers and the cavity beam pipes, as shown in Figure 8-13. The temperature rises of the STF-2 couplers were approximately 10 K while those of the TTF-III couplers were less than 1 K. This temperature rise is considered to be due to heat generation at the 3 μm Cu layer on the inner surface of the outer conductor. The Cu layer of the STF-2 coupler will be studied and improved in the next model.

Table 8-5: Dynamic loss of four and seven cavities.

	MC 4 cav.	MC 4 cav.	MA 4 cav.	MA 4 cav.	MC-MA 7 cav.
G_{ave} [MV/m]	20 (average)	32 (detune)	26.9 (average)	32 (detune)	25.4 (average)
Q_D, [W]	2.7	NA	6.9	NA	9.6
$Q_{D\text{-}det}$, [W]	0.2	0.5	2.5	4.6	2.6
$Q_{D\text{-}cav}$, [W]	2.5	NA	4.4	NA	7.0

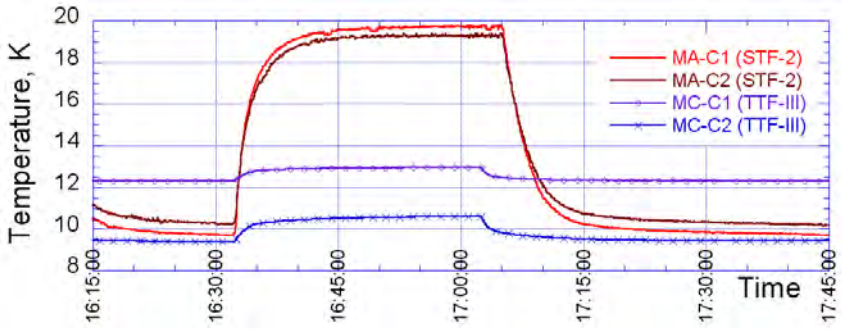

Figure 8-13: Temperature changes of the connection flanges of the input couplers at a detuning of 32 MV/m.

9 High-Level RF System

9.1 Summary of HLRF development for S1-Global

The HLRF system satisfies two of the aims of the S1-Global project. The first is to supply the required microwave power to the super-conducting cavities (SC), and the second is to demonstrate a complete and feasible HLRF system, which will be considered for the ILC. At KEK, a HLRF system based on the RDR has been under development since 2005, and includes two possible power distribution systems (PDS). Another new HLRF system has been proposed for mating single tunnels and was based on distributed RF systems (DRFS). This new HLRF system was introduced and developed at KEK. In S1-Global, these two HLRF schemes are evaluated, and this report describes the test results.

9.2 RDR-type Configuration of HLRF

9.2.1 RDR-type Configuration of HLRF

The HLRF system has been described in detail in the RDR [9-1], so we describe it here briefly. A 10 MW klystron provides power to 26 SC cavities through a suitable PDS. A high-voltage, 1.5 ms width pulse for the klystron is provided by the modulator, which contains a bouncer circuit to compensate the droop of the pulse top. In KEK, two HLRF systems were used for S1-Global, which are referred to as the No. 1 station and the No. 2 station, and these systems were essentially the same as those used during the STF-1 tests conducted in early 2010. Both the stations employ 5 MW klystrons. One of the modulators had previously been used, and was transferred from the Power Reactor and Nuclear Fuel Development Corp. (PNC) and modified by adding the bouncer circuit. Another modulator was newly manufactured in 2005 to meet the ILC RDR specifications. In the PDS in the RDR, two types of PDS were proposed, i.e., a linear PDS and a tree-type PDS that uses 3 dB power dividers. Both the systems were evaluated during the S1-Global tests [9-3].

Table 9-1 : Specification of Modulator and Klystron

Item	Unit			
Modulator No		No.1 PS	No.2 PS	
Klystron		TH2104A	TH2104C	MBK
Klystron applied voltage	kV	140	130	115
Klystron beam current	A	107	96	132
Pulse width(70%-70%)	ms	1700	1700	1700
Rise time	ms	200	200	200
Pulse flat top(90%-90%)	ms	1370	1370	1370
Flatness within pulse duratio	%	0.5	0.5	0.5
Repititiom	Hz	5	5	5
duty		0.0085	0.0085	0.0085
Step-up Ratio of PT		1 : 6	1:15	1:15
Pimary Voltage	kV	23.3	8.7	7.7
Primary Current	A	642	1440	1980
Primary Impedance	Ω	36	6.04	3.9
Peak Power of Modulator	MW	15	12.5	15.2
Average Power of Modulator	kW	128	106	129

9.2.2 Modulator Specifications

As described in section 9.2.1, there are two RF stations, and the modulator and klystron specifications for each station are shown in Table 9-1. A schematic diagram of the No. 1 modulator is shown in Figure 9-1. The red parts in Figure 9-1 are the newly added components and the blue parts are the reused units from the Japanese Hadron Project (JHP). The No. 2 modulator was manufactured according to the ILC specifications, which includes the uses of a 10 MW multi-beam klystron (MBK). The basic circuit layout for the No. 2 modulator was the same as that of the No. 1 modulator except for the step-up ratio of the pulse transformer (see Table 9-1). The bouncer circuit was introduced into these modulators and was shown to successfully compensate for the pulse droop; to demonstrate this, waveforms from the No. 1 station are shown in Figure 9-2. The performance of the bouncer circuit in both the modulators was excellent and a flat-top of less than ±0.8% was achieved in both the modulators.

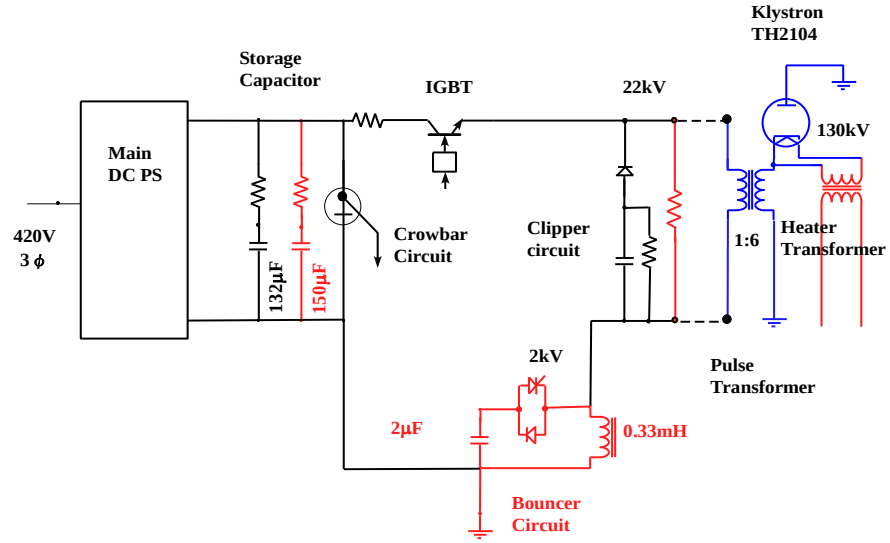

Figure 9-1: Circuit diagram of the No. 1 modulator and klystron.

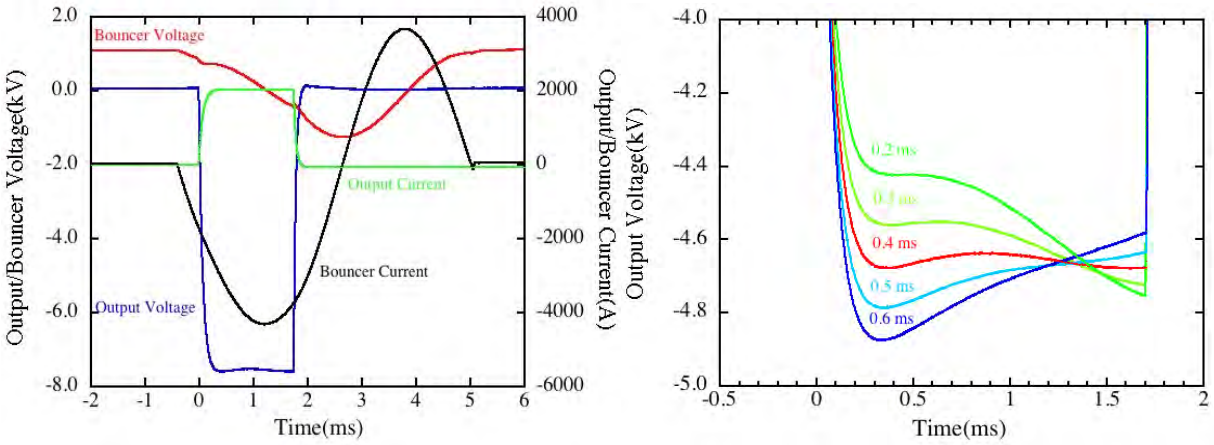

Figure 9-2: Output pulse of voltage (blue) and current (green), and voltage (black) and current (red) of bouncer circuit (left). Change in flatness due to changes in bouncer timing (right).

9.2.3 Klystron Specifications

During the S1-Global tests, we used the No. 1 and No. 2 RF stations with two 5 MW klystrons, which were manufactured by Thales Corporation. The first klystron is referred to as TH2104C, and was once used in the JHP, and the second is referred to as TH2104A, which was newly procured for STF. Both were capable of outputting 5 MW power at 1.3 GHz with a pulse width of 1.5 ms and repetition rate of 5 Hz.

9.2.4 Power Distribution System (PDS)

9.2.4.1 General Description of PDS

The power distribution system of S1-Global used two different schemes, as shown in Figure 9-3. A tree-type power-dividing scheme using variable 3 dB hybrids (3 dB Hybrid PDS) was employed for cryomodule-C. A variable power divider from a variable tap-off (VTO) manufactured in SLAC was also introduced into this system. The linear distribution system (i.e., a TESLA-type PDS used in the TESLA) was used in cryomodule-A. In order to protect the klystron from any large reflected RF power, a 5 MW circulator made by the STP Corporation in Russia was installed and filled with SF6 gas. In each of the coupler's ports, a 400 kW circulator was installed to eliminate the undesired effects produced by reflected power from the SC cavity. In addition, a Q-variation system combined with a reflector and phase shifter was introduced into each of the coupler's ports.

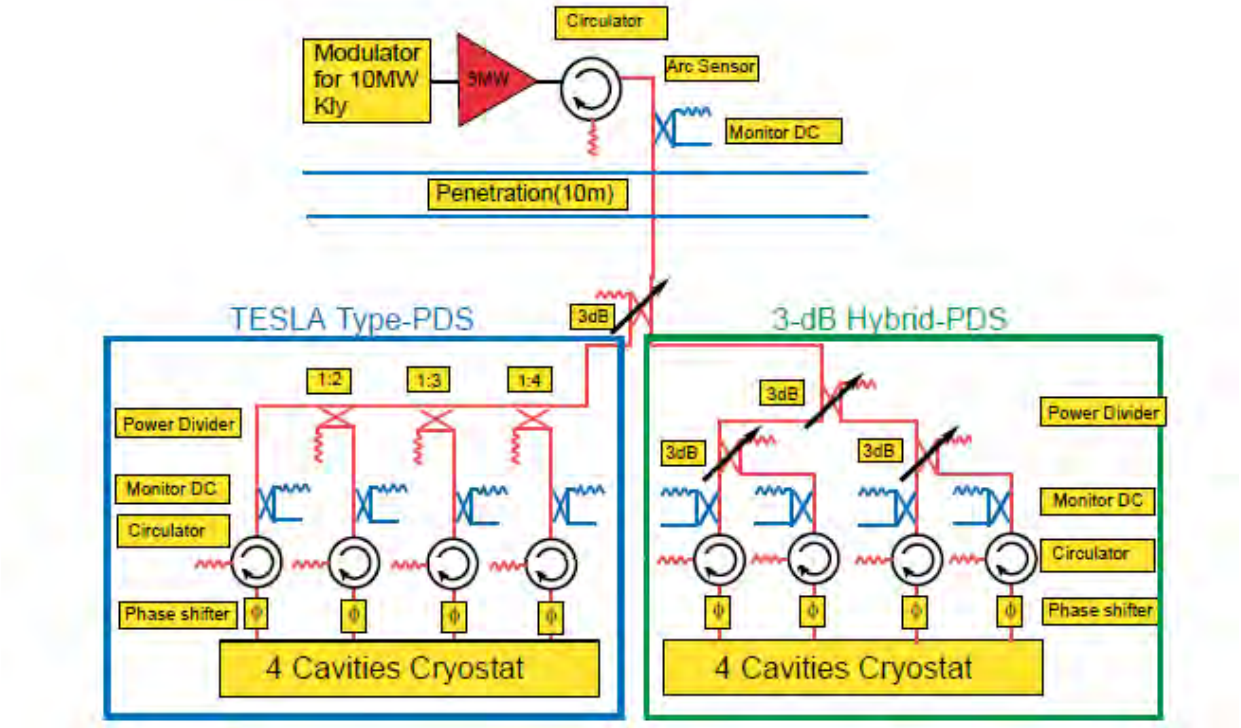

Figure 9-3: Power distribution systems used in the S1-Global tests.

9.2.4.2 Waveguide Components

9.2.4.2.1 Variable Tap-off Developed by SLAC [9-4]

The VTO developed by SLAC was combined by two 3-port junctions and a mode rotator. In the VTO, the polarization selected by the first 3-port junction propagates through the oblong cross-section of the mode rotator and the three outputs were coupled from the second 3 port junctions. By changing the angle of the mode rotator, the coupling could be varied from 0 to 100%. The VTO's power capability was more than 5 MW and its shape is illustrated in Figure 9-4.

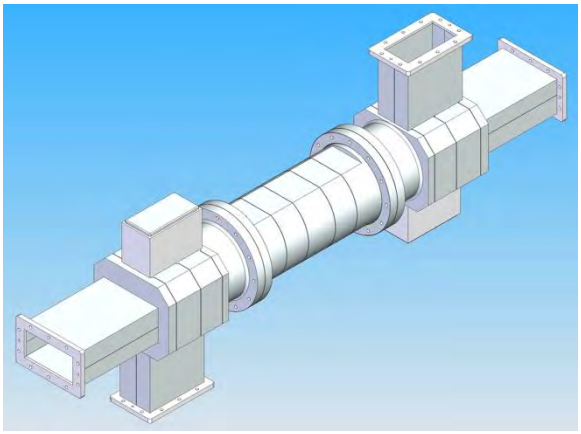

Figure 9-4: Variable Tap-off (VTO)

9.2.4.2.2 Variable Power Divider Developed by KEK

KEK developed another type of variable power divider, which is shown in Figure 9-5. In the central part of the hybrid waveguide, there are two floating boats and the output coupling can be varied by changing the distance between the boats. The range of couplings available depends on the length of the central waveguide, which are illustrated schematically in Figure 9-5. The longest waveguide has a power variation range from 0% to 100%. The power capability of these dividers is greater than 5 MW.

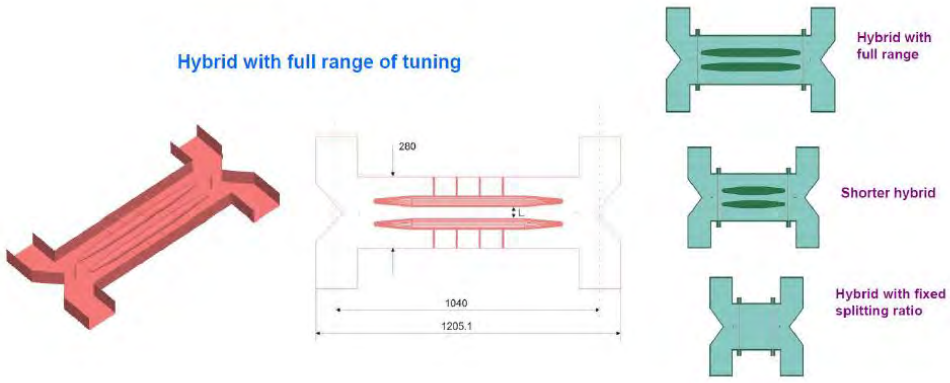

Figure 9-5: Variable hybrid.

9.2.4.2.3 Q-variation Mechanism in PDS for S1-Global

When considering a 2-port PDS connected by a hybrid, possible schemes for varying the power, phase, or loaded Q (individually or at the same time) can be realized by introducing a reflector, a phase shifter, and a circulator. In S1-Global, although the loaded Q could be varied by coupler tuners, it was not controlled remotely. Therefore, we introduced a system consisting of a reflector, a phase shifter, and a circulator, as shown in Figure 9-6. By changing the reflector bane angle and phase shift amount, the loaded Q could be changed by more than +-100% with respect to the design value of 3×10^6.

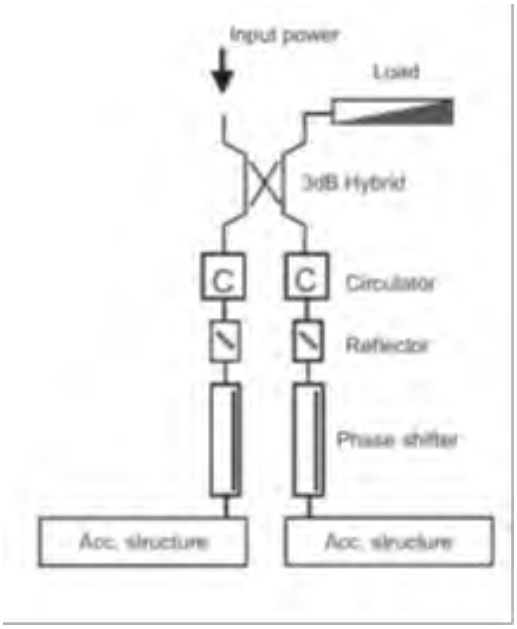

Figure 9-6: Schematic drawing for varying the loaded Q (Q_L) of a cavity in the PDS.

9.2.4.2.4 Phase Shifter and Reflector

A phase shifter, which was used for the PDS described in 2.4.2.3, was realized by using a floating boat inside the waveguide and by changing the insertion of floating boat into the H-plane of rectangular waveguide, the phase was varied. The phase shifter is shown in Figure 9-7. The reflector, which was used for the PDS as described in 9.2.4.2.3, was a structure with a rotatable vain that was perpendicular to the propagation direction and a matching structure was inserted into the E-plane of the rectangular waveguide, as shown in Figure 9-8.

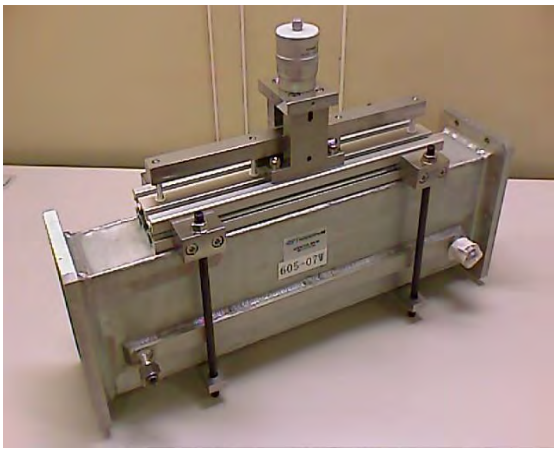

Figure 9-7: Phase shifter.

Figure 9-8: Reflector.

9.2.4.2.5 Circulator

In order to protect a high-power klystron from any reflected power, a 4-port circulator, which has a 5 MW capability, was installed at the output end of the klystron waveguide. The circulator was manufactured by STP Corporation in Russia, and its notable characteristics include a low insertion loss of less than 0.15 dB at 1.3 GHz and an isolation of more than 30 dB. It was used while the waveguide was filled with SF6. In addition, during the RDR configuration of the PDS, medium power (400 kW) circulators were installed at the coupler port of the SC cavity. These cause the reflected power from the SC cavity to be selectively dissipated by the load and they also eliminate any interference between the two cavity ports. We purchased two types of 400 kW circulators with similar capabilities; one made by Russian STP Corporation and another made by Japan Radiofrequency Corporation. In S1-Global, the latter circulators were used. In Figure 9-9, a 5 MW circulator and a Japanese 400 kW circulator are shown.

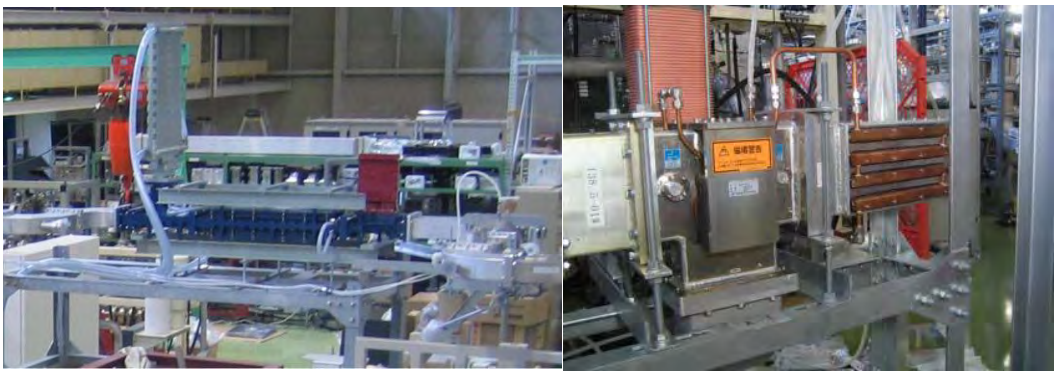

Figure 9-9: 5 MW circulator made by STP Corporation (left) and the 400 kW circulator made by Nihon-Koshuha Corporation (right).

9.2.5 HLRF Study Item in S1-Global

Although similar HLRF studies were performed during Phase 1.0 at STF with Japanese SC, because new SC cavities from Europe and US were installed, the SC cavities were individually reconnected to the PDS to feed power to the cavities from the RF source prior to starting the S1-Global tests. Two power sources were employed and it required one month to complete this process. Each RF source provided power to four cavities in order to evaluate the LLRF feedback. Tests were also performed to evaluate the LLRF feedback while the No. 2 station provided power to eight cavities. These tests are described in the section of LLRF (Section 10).

9.3 DRFS-type Configuration of HLRF [9-5]

9.3.1 Aims and Configuration of DRFS

After successfully completing the RDR-type configuration of the HLRF in the S1-Global module, the DRFS-type configuration of the HLRF was evaluated. The purpose of this was to demonstrate the DRFS system and in particular to demonstrate the LLRF without a circulator in the PDS. Because this was the first time the DRFS system had been operated, tests of the DC power supply, MA modulator, and DRFS MA klystrons were performed in the klystron hall on the first floor, and then the MA modulator and klystrons were moved to the tunnel floor. The DC HV was also moved from the first floor to the tunnel floor. A bird's-eye view of the system is shown in Figure 9-10. While using the DRFS system, it was necessary to demonstrate the feasibility of delivering power from a common DC P/S and MA modulator to several klystrons, and therefore, a minimum of two RF klystrons was required in all tests. After the RDR configuration test, we selected two pairs of SC cavities with reasonably high field gradients and two RF sources were connected to them.

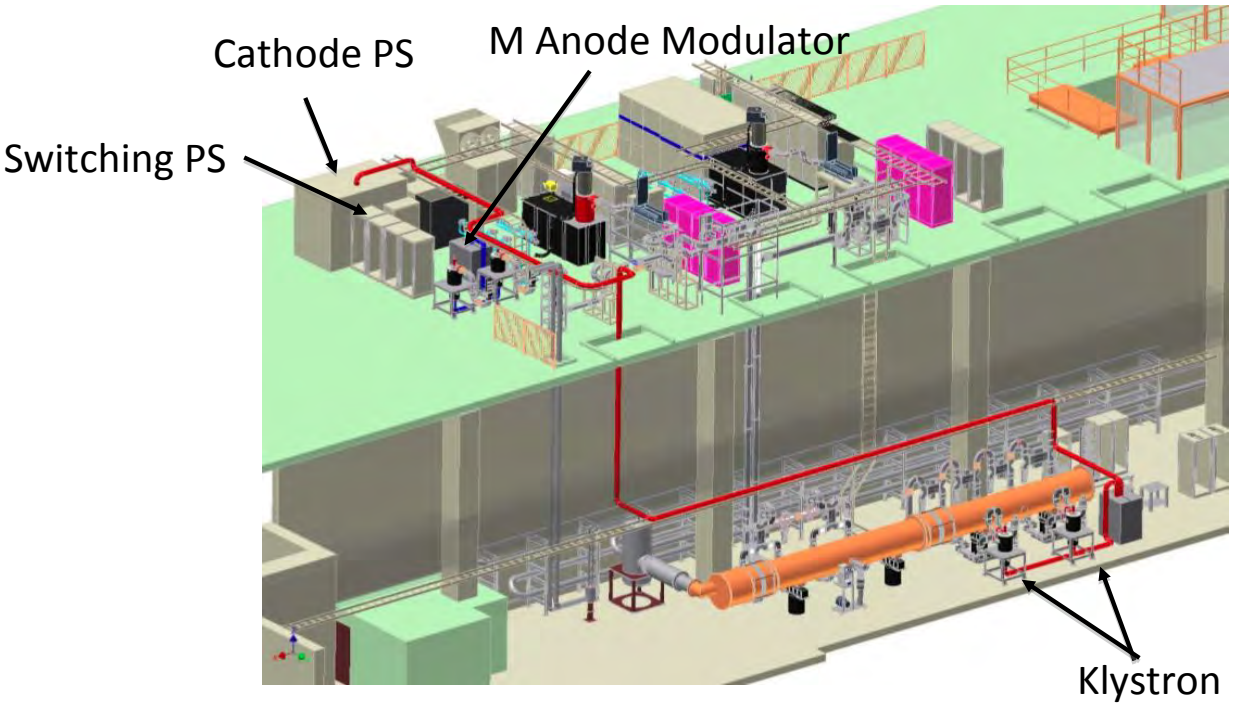

Figure 9-10: Bird's eye view of the DRFS system in S1-Global.

9.3.2 DRFS Klystron

The DRFS klystron is a modulating anode-type klystron that provides power to two SC cavities. The output power is 800 kW with a 1.5 ms pulse width and a 5 Hz repetition rate. The DRFS klystron was newly developed by Toshiba Corporation for this project and Table 9-2 lists the specifications of the DRFS RF source. Prototype DRFS klystrons were manufactured in FY2010 and their typical characteristics are shown in Figure 9-11.

Table 9-2: DRFS klystron specifications.

Table 2:	DRFS Specifications		
Klystron	Frequency	1.3	GHz
	Peak Power	800	kW
	Average Power Output	6.00	kW
	RF pulse width	1.5	ms
	Repitition Rate	5	Hz
	Efficiency	60	%
	Saturated Gain		
	Cathode voltage	65.8	kV
	Cathode current	20.3	A
	Perveance(Beam@65.8kV)	1.2	micro Perv
	(Gun@54.4 kV)	1.56	micro Perv
	Life Time	120,000	hours
	# in 3 cryomodule	13	
	Focusing	Permanent magnet	
	Type of Klystron	Modulated Anode Type	
DC Power supply per 3 cryomodules			
	# of klystron (3 cryomodule)	13	
	Max Voltage	71.5	kV
	Peak Pulse Current	263.4	A
	Average Current	2.9	A
	Output Power	190.7	kW
	Pulse width	2.2	ms
	Repitition Rate	5	Hz
	Voltage Sag	<1	%
	Capacitor	26	mF
Bouncer Circuit			
	Capacitance	260	mF
	Inductance	4.9	mH
M. Anode Modulator			
	Anode Voltage	54.4	kV
	Anode Bias Voltage	-2	kV

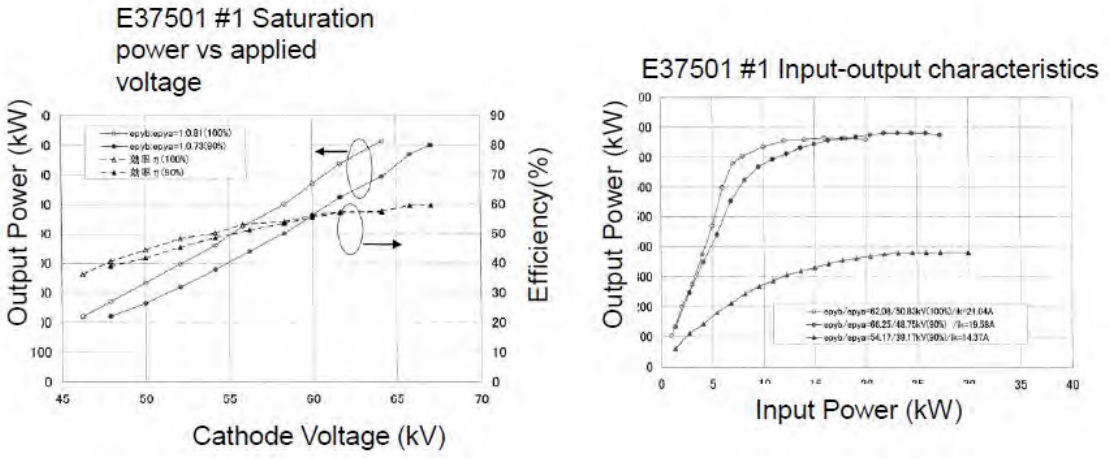

Figure 9-11: Characteristics of DRFS klystron.

9.3.3 DC Power Supply and MA Modulator for DRFS Klystron

Because the DRFS klystron has a MA electrode, a DC power supply and a MA modulator were used to supply power to the two DRFS klystrons. A block diagram of the power supply system is shown in Figure 9-12 (top). Due to budget limitations, a bouncer circuit was not used for pulse droop compensation. Instead, the droop of the output RF pulse was compensated by the LLRF control with a feed-forward table. The output waveform from the power supply is also shown in Figure 9-12.

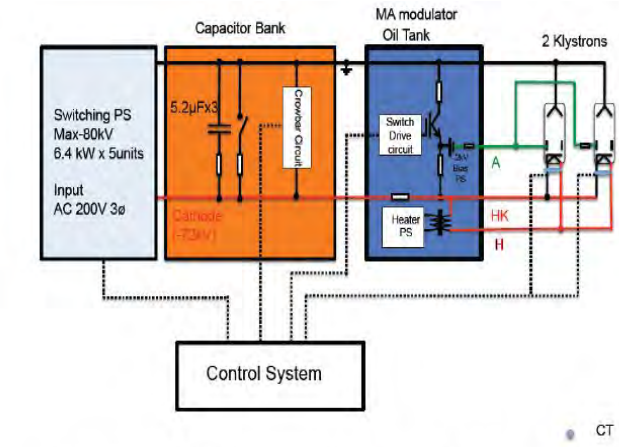

Circuit Diagram used in S1-global DRFS

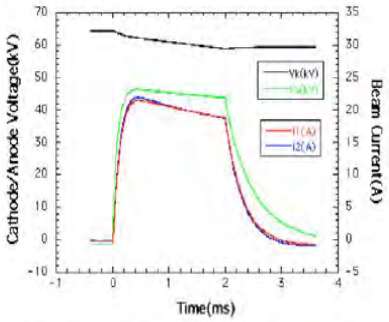

Voltage waveform when 2 klystrons were operated in parallel

Figure 9-12: Circuit diagram of the S1-Global DRFS(top). Power supply output voltage waveform while operating two klystrons in parallel (bottom).

9.3.4 PDS for DRFS

As described earlier, the main purpose of this test in S1-Global is to demonstrate the successful operation of the PDS without a circulator. A schematic drawing of the PDS in DRFS is shown in Figure 9-13. The outputs from the klystron were divided by a magic-tee and fed to two SC cavities. One waveguide port was designed to be a phase of 90° longer in order to cancel the reflected power to the klystron port from the cavities having an equal characteristic. The output window of the klystron was the same size as that of the 5 MW klystron and even for the case of full reflection, fatal failure of the window was avoided.

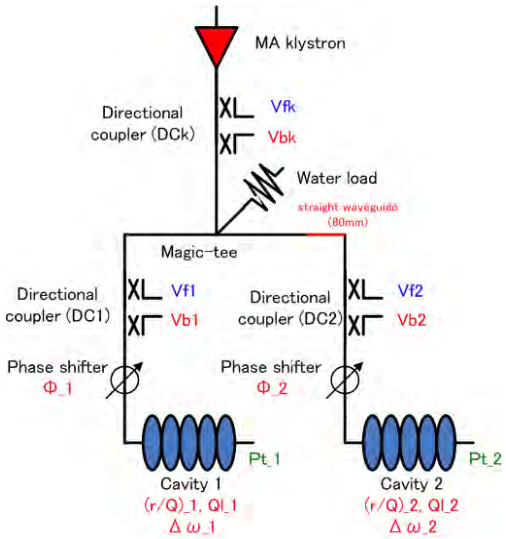

Figure 9-13: PDS of DRFS.

9.3.5 Performance of DRFS HLRF in S1-Global

Although some of the input RF power is reflected at the rising edge and falling edge of the pulse, if two cavities are of the same quality, the two reflections are cancelled by the magic-T as described in Section 3.4 and as a result, there is no reflection back towards the klystron and all the reflected power is dissipated by a dummy load after the magic-T. No cross talk is expected between the two ports of the PDS and the cavities in this case. When two cavities do not have equal characteristics, the power that is not cancelled results in a finite VSWR value and the cavities interfere with each other. This happens at the different detuning by micro phonic effect of cavities. If the gradient of one cavity deteriorates, this may also cause an imbalance in quality. Then the mixed power in the falling edge of the pulse where cavity diagnosis was conducted by RF decay observation gave a wrong Q_L value estimation. However, if Q_L values were extracted using the cavity differential equation, a correct Q_L value was obtained. The desired amplitude and phase stability was obtained, and therefore, the PDS in DRFS without circulators was successfully demonstrated. This is described further in LLRF section (section 10). Figure 9-14 shows a photo of the DRFS klystrons installed near the cryomodule. The DRFS was successfully demonstrated during the S1-Global tests.

Figure 9-14: Picture of the DRFS in the tunnel.

10 Low-Level RF System

10.1 Introduction

From the viewpoint of the RF system, the S1-Global project can be divided into three stages. In Stage 1, the performance of each cavity, characterized by parameters such as the quench limit and Lorentz force detuning, was examined. To examine the cavity efficiently, two RF sources were used. Each 5 MW klystron (1.3 GHz, 5 Hz, 1.6 ms) drove four cavities. Figure 10-1 shows a schematic of the RF system. A conventional digital low-level RF (LLRF) system was adopted in this Stage 1 and Stage 2. A FPGA board on a commercial DSP board (Barcelona) was used to control the RF output from each klystron. The FPGA board has 10 16-bit ADCs and 2 14-bit DACs with an FPGA and installed to cPCI [10-1] as shown in Figure 10-2.

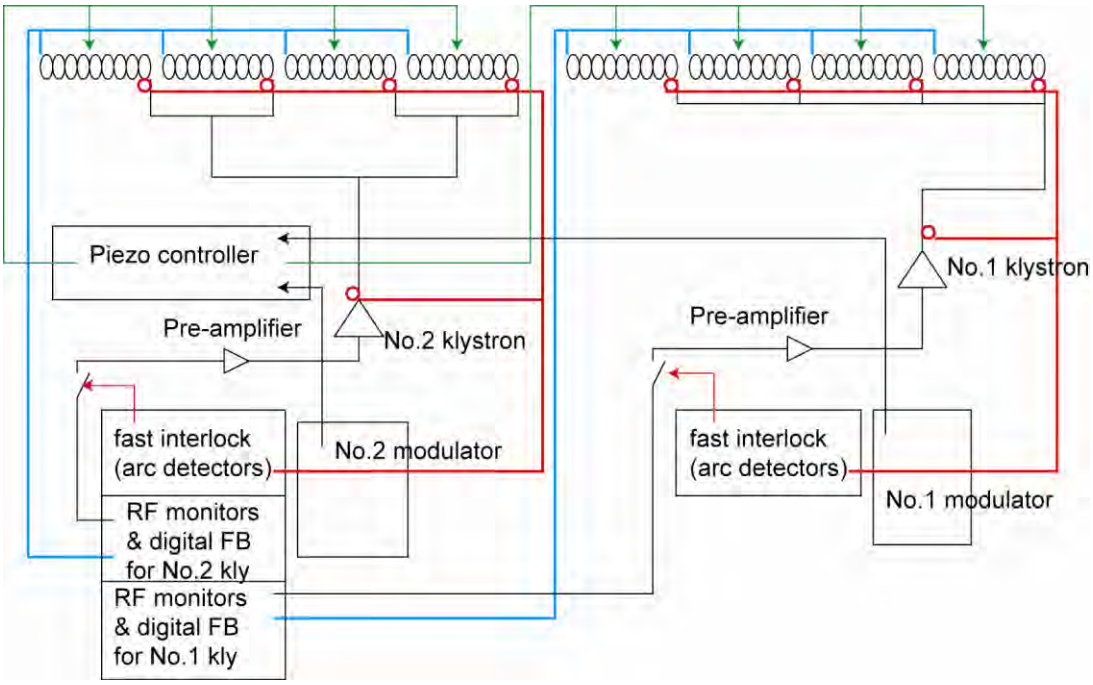

Figure 10-1: Schematic of the LLRF system during Stage 1.

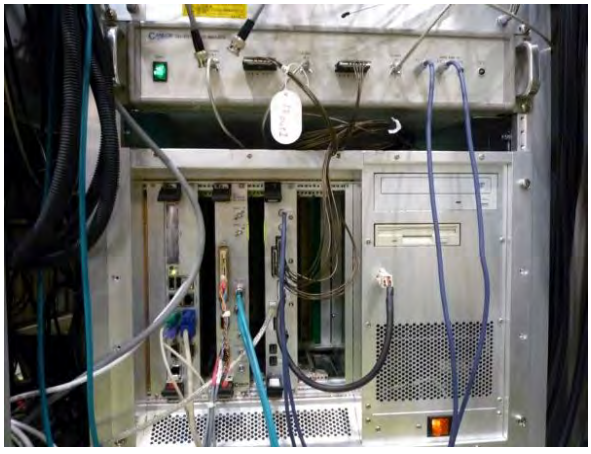

Figure 10-2: Photograph of the cPCI digital FB system.

In Stage 2, the vector-sum performance was evaluated. Figure 10-3 shows a schematic of the RF configuration during Stage 2. To maximize the gradient of each cavity, the ratios of the RF input powers to the cavities were optimized using tunable hybrids and variable tap-offs [10-2]. One cPCI became the FB controller and operated a vector-sum control. The in-phase (I-component) and quadrature phase (Q-component) of the cavity pick-up signals were summed (using a vector-sum) and compared with the reference set points. The errors were multiplied by the numerical gain and finally feed-forward tables were added. The data acquisition during RF operation was every 1 μs, although the feedback frequency was 40 MHz.

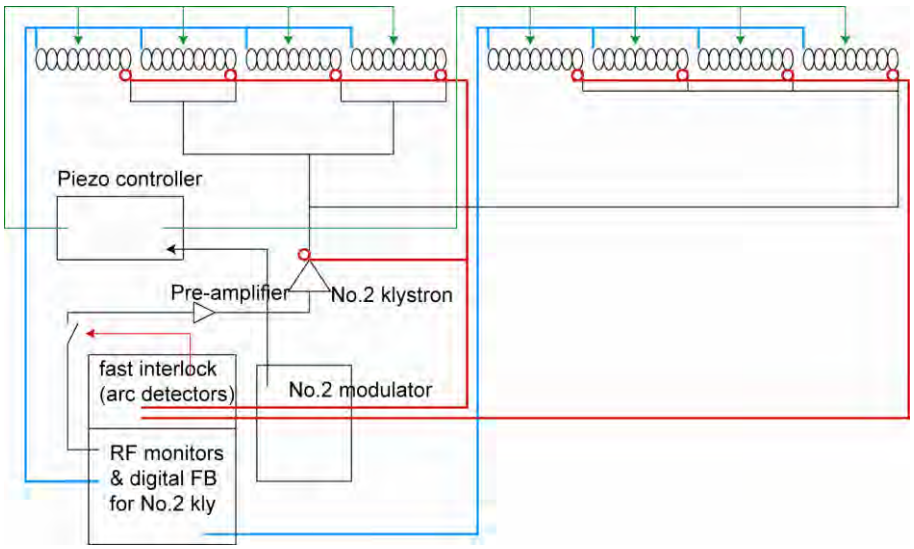

Figure 10-3: Schematic of the LLRF system during Stage 2

The entire LLRF system in Stage-2 is summarized in Figure 10-4. The RF pick-up, and the forward and reflected signals are split between four ports. The first cable is connected to the conventional cPCI via a down-converter. The second is connected to the IF-mix RF monitor. The third is connected to the RF power meter (Gigatronics) (Figure 10-5) or a 32-channel ADC board, and the fourth is used by the cavities. Some of the output from the klystron and part of the reflection back towards the klystron are connected to the VSWR meter and used as interlocks to protect the klystrons. The RF power-meters and fast interlock are EPICS IOCs.

A local oscillator (LO; 1310.16 MHz) is generated by mixing clock dividers output (1300 MHz/32/4) using AD9510 and an IQ modulator. The clock signals (CLK; 40.625 MHz) are generated by clock dividers (1300 MHz/32). In order to define the I and Q components, a timing clock (timing; 10.156 MHz) is also used.

In the IF-mix, three IFs are mixed by a RF combiner and the result is fed into each ADC. These IFs are at 9.02 MHz (IF1, 1300/16/9 MHz), 13.54 MHz (IF2, 1300/32/3 MHz), and 18.06 MHz (IF3, 1300/8/9 MHz). The signal is then separated into three IQ components (cavity pick-up, cavity input, and RF reflection from the cavity) by digital signal processing. This enables the use of a maximum of 30 RF signals by 10 ADCs. Remote-attenuators (EPICS IOCs) are installed after the four port RF dividers and these signals are connected to 96 down-converters or 10 channel down-converters.

The RF cables were calibrated by the following method, because a beam-based calibration method was not available during the S1-Global experiments. The attenuation of each cable was obtained using a network analyzer by measuring the S-parameter S11 while changing the reflection position (line-stretcher).

This method enabled us to cancel the VSWR of the cable itself. Figure 10-6 shows the typical measured signals obtained by this procedure. The offset of the circle corresponds to the VSWR of the cable itself and the cable loss is calculated from the radius of the circle.

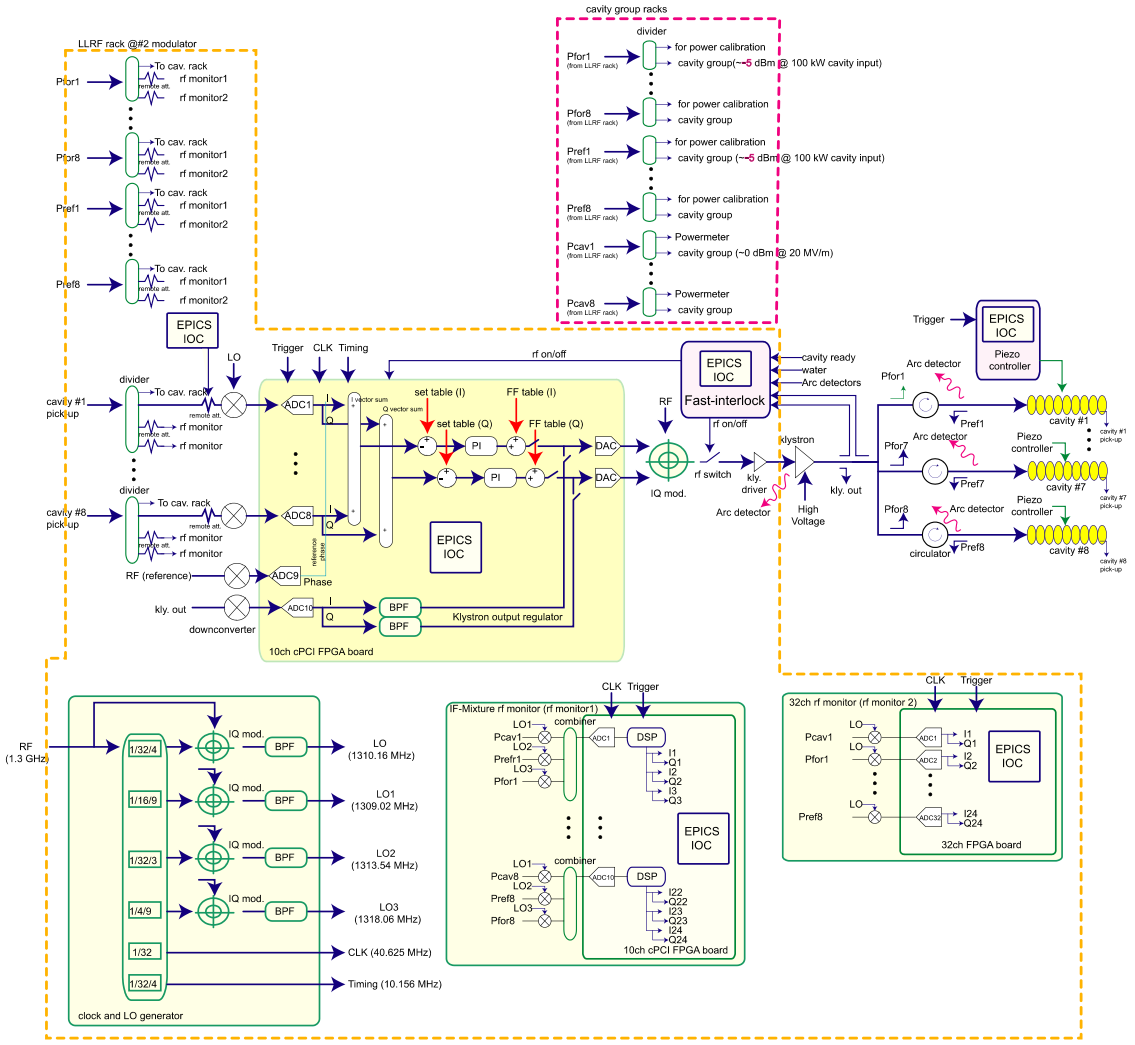

Figure 10-4: Digital LLRF configuration during Stage 2.

Figure 10-5: Photograph of the power-meters used for the S1-Global experiments.

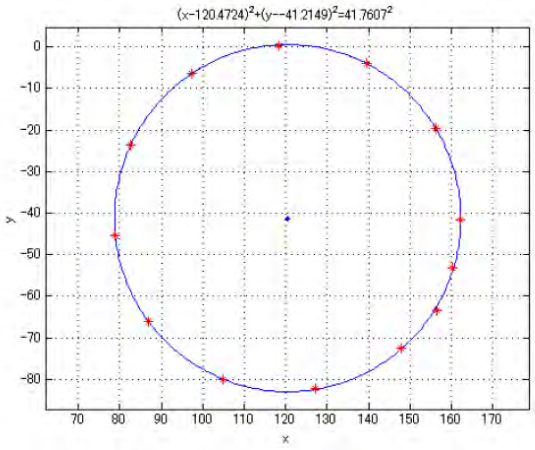

Figure 10-6: Measured S11 used for cable calibration.

10.2 LLRF System for DRFS (Stage 3)

In Stage 3 of S1-Global, a distributed RF system (DRFS) [10-3] was evaluated. Two 800 kW klystrons were connected to one RF modulator; each klystron drove two cavities. The digital feedback system based on the µTCA standard [10-4] (Figure 10-7) was located near the cryomodule tunnel. Figure 10-8 shows a photograph of the LLRF racks located in the tunnel. Not only the digital FB system but also the LO signals for the µTCAs and down converters were generated, as shown in Figure 10-9. Figure 10-10 shows a schematic of the LLRF system in the tunnel. The total operating time of the DRFS was about 66 h and the total radiation ionizing doze at the LLRF racks was 140 mSv (~2 mSv/h). Because the total ionizing dose effects for semiconductors appears above ~8 Gy [10-5], the DRFS configuration (without beam) will allow 4000 h of operation. The radiation level (with beam) measured at FLASH was 15 mGy/h [10-5] and this allows for 500 h of operation without a shield. In “Quantum beam” and STF-2, some type of radiation shield will be required to protect the LLRF equipment installed in the beam tunnel.

Figure 10-7: µTCA-based digital LLRF system during Stage 3.

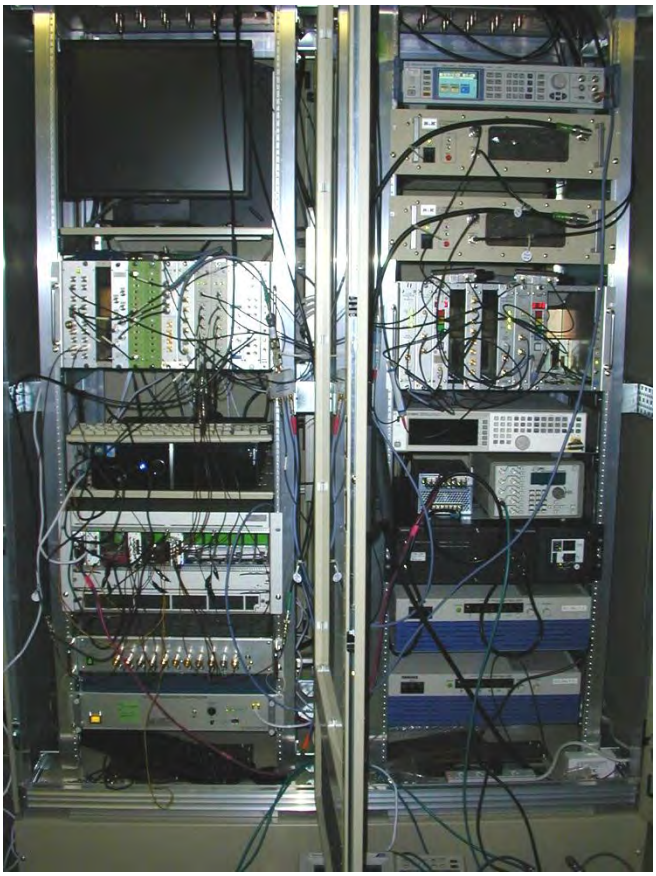

Figure 10-8: Photograph of the LLRF rack layout during Stage 3.

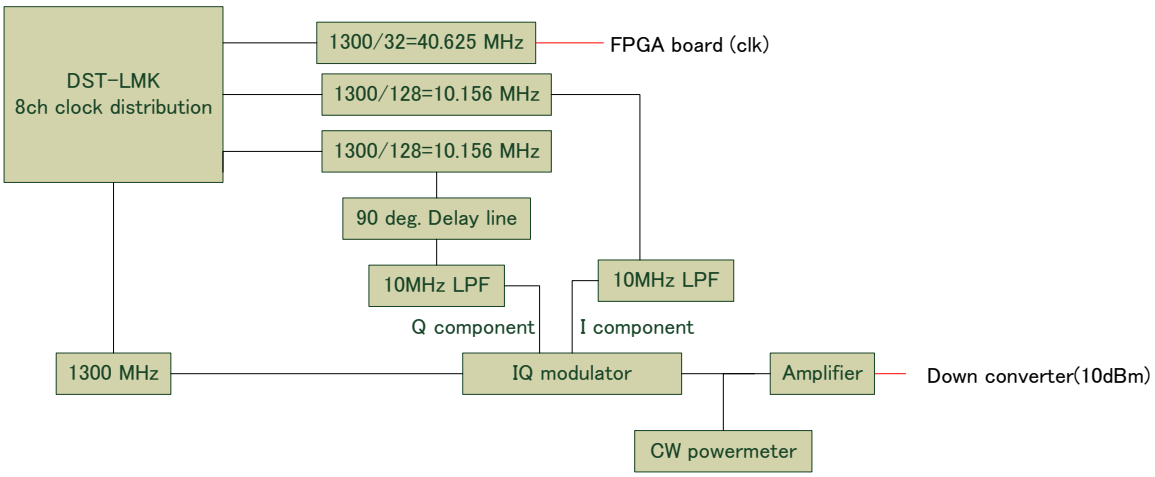

Figure 10-9: Clock generation used for Stage 3.

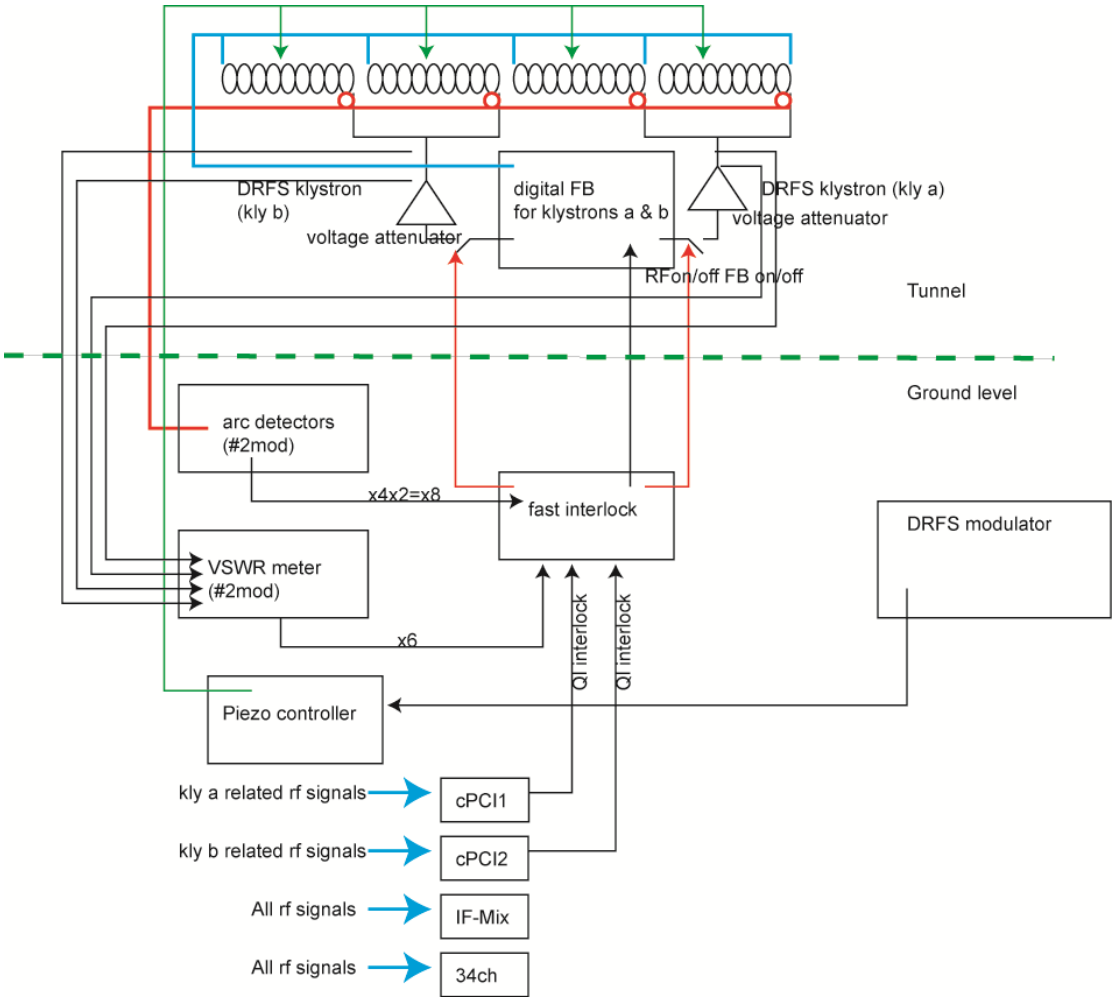

Figure 10-10: Schematic of the LLRF system at Stage 3.

10.3 Interlock System

A quench introduces a significant cryogenic heat load. If quenching occurs, the RF input to the cavity should be stopped as soon as possible; otherwise, the system cannot operate until the cryogenic system has recovered. Thus, we developed a rapid quench detection and interlock system. The loaded Q (Q_L) of each cavity (~2.4 x 10^6) is calculated using the RF decay time at the end of the RF pulse; if the value is lower than the threshold for Q_L (e.g., 2.0 x 10^6), RF operation stops at the next pulse, as shown in Figure 10-11. This quench-interlock system works well and helps to lower the heat load on the cryogenics system.

The DRFS operation makes it difficult to detect quench with this procedure because of the cross talk between cavities. However, we continued to use the Q_L value obtained from simple RF decay. Quench detection sometimes requires an additional pulse, but the cryogenic heat load is reduced even when this is this case. Arc detectors attached near the cavity couplers and RF power interlocks were also introduced to protect the couplers and klystrons, respectively, from breakdown.

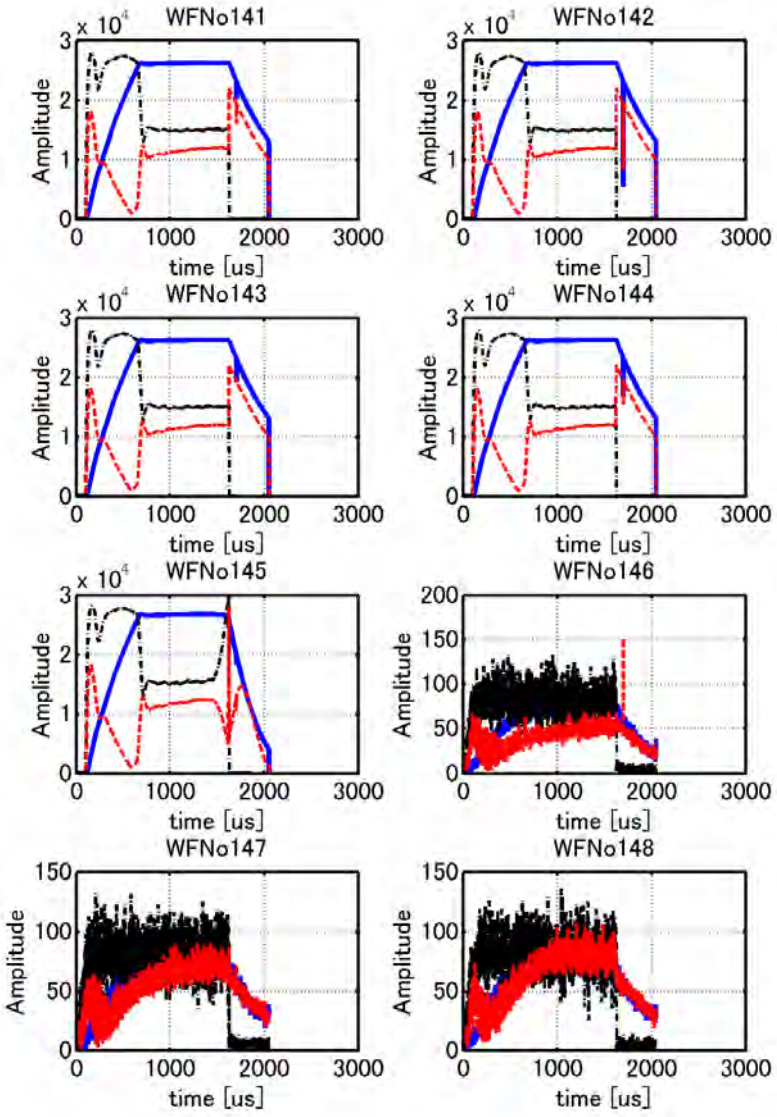

Figure 10-11: Quench detector: Blue curve shows field waveform in the cavity. Black doted curve is input RF waveform, red doted curve is reflected waveform. These eight plots shows each pulse waveform along pulse sequence. At No.145 pulse, blue curve fall down in the pulse tail, shows quench sign. In the next pulse, input RF was shut down by this quench detection.

10.4 Cavity Diagnostics

A special feature of the DRFS is that it was operated without circulators [10-3]. If the cavities are paired, the RF reflection can be cancelled when the paired cavities are operated with exactly the same parameters (dynamic detuning and Q_L etc). If the cancellation is not perfect (for example, during commissioning of the cavities), reflection back towards the klystron occurs, and cross talk between the cavities subsequently appears. The former may result in damage to the klystron and the latter makes cavity diagnostics difficult.

Correct on-line cavity diagnostics are essential for successful DRFS operation. Therefore, we have developed these diagnostics.

Dynamic detuning caused by the Lorentz force in the cavity affects the RF performance when the cavity is operated at a gradient above 20 MV/m. Piezo-actuators were installed in all the cavities, so the cavity tuning could be controlled dynamically. The cavity detuning should be maintained below 50 Hz during the RF flat-top. The optimization of the piezo-actuator requires a precise detuning monitor (e.g., < 5 Hz of detuning frequency). Dynamic detuning is typically measured by the pulse-shortening method [10-6], in which the RF pulse length is changed and the detuning at the end of the pulse is calculated from the phase change. These values appear reliable but do not take into account microphonic effects (fluctuations in the pulse-to-pulse detuning). In addition, this method is not suitable for systems without circulators, such as the DRFS, because the release of stored energy in one cavity becomes the RF input to the other cavity (and vice versa). Thus, we cannot define a clear "RF-off" status, which is essential for the pulse-shortening method. To solve these problems, we developed a real-time detuning monitor based on the cavity differential equation. The cavity voltage (V_{cav}) and cavity input voltage (V_{for}) satisfy the following cavity equation:

$$\frac{\mathrm{d}}{\mathrm{dt}}\mathrm{V_{cav}} = -\left(\omega_{1/2} - \mathrm{j}\Delta\omega(\mathrm{t})\right)\mathrm{V_{cav}} + 2\omega_{1/2}\mathrm{V_{for}}, \qquad (1)$$

where $\omega_{1/2}$ $(= 2\pi f_0/2Q_l)$ and $\Delta\omega$(t) are the bandwidth and dynamic detuning of the cavity, respectively. By using eq. (1), we can obtain Q_L and the detuning.

Eq. (1) can be modified as follows:

$$\frac{1}{2}\frac{\mathrm{d}}{\mathrm{dt}}|\mathrm{V_{cav}}|^2 = \omega_{\frac{1}{2}}(\mathrm{t})\left(|\mathrm{V_{for}}|^2\text{-}|\mathrm{V_{ref}}|^2\right), \qquad (2)$$

where V_{ref} is the reflection voltage from the cavity, which satisfies $V_{cav}=V_{for}+V_{ref}$. We can calculate the time-dependent Q_L by using eq.(2) except in the RF flat-top region where the cavity voltage (V_{cav}) is constant.

The precise cavity input power is needed for this detuning calculation. Because the directional RF couplers have a directivity of 20-30 dB, cross talk occurs between V_{for} and V_{ref} and it is difficult to determine the precise cavity input power. To obtain better resolution for the detuning and Q_L estimates, both V_{for} and V_{ref} are corrected by using the measured directivities. Figure 10-12 shows the calculated detuning at Stage 2. The upper eight plots show the detunings and the lower eight show the normalized V_{cav}, V_{for}, and V_{ref}. Because signals from a total of 24 channels (8 cav. $\times$ V_{for}, V_{ref}, and V_{cav}) are required for these measurements, signals obtained by the IF-mix are utilized for the real-time detuning calculation. This real-time detuning monitor is quite useful for adjusting the piezo-actuator compensation.

Figure 10-13 shows the results of the cavity diagnostics (dynamic detuning and Q_L values) during DRFS operation with cavities of different loaded Q condition. Under these conditions (caused by e.g., differences in detuning), cavity input signals exist even after the RF input is switched off and the Q_L values obtained from a simple decay constant are incorrect. However, those calculated from eq. (2) (blue line) remained constant under various detuning conditions. The cavity diagnostic method works well and enables control of the detuning, which is especially useful for optimization of the piezo-actuator control.

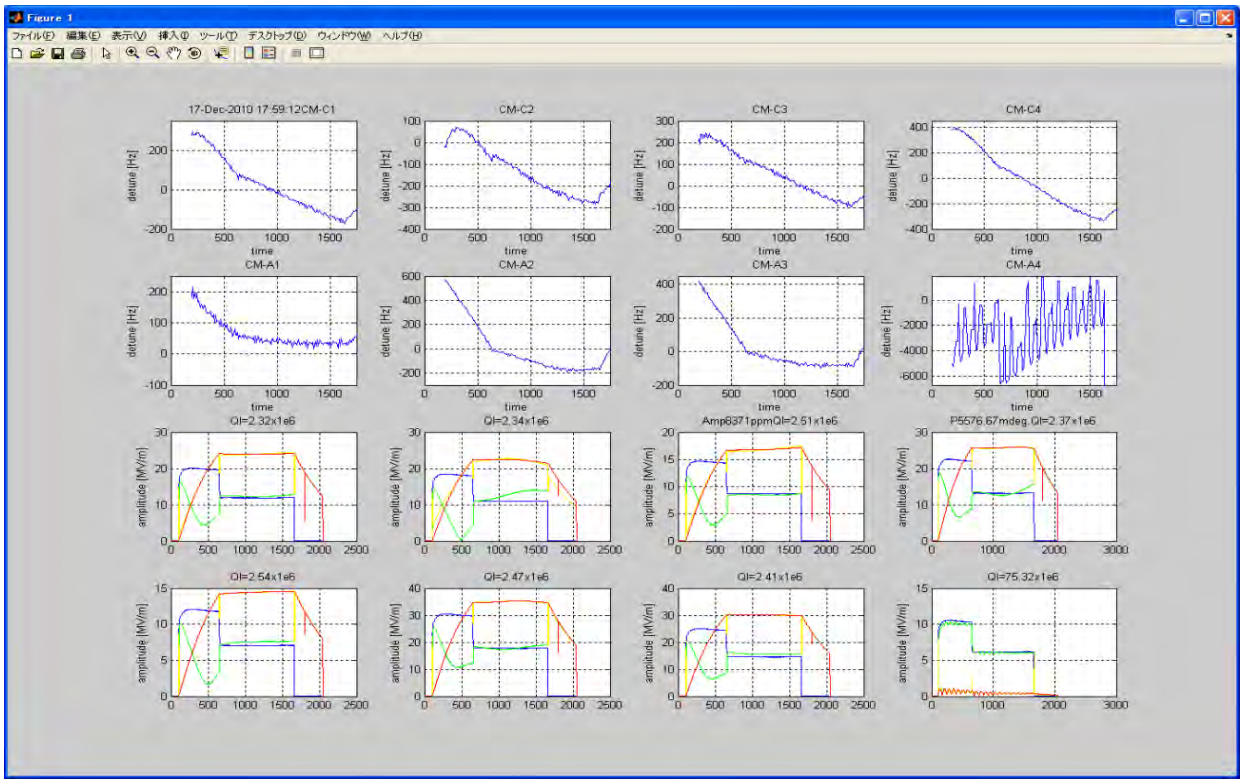

Figure 10-12: Real-time diagnostics from the on-line detuning monitor used at Stage 2.

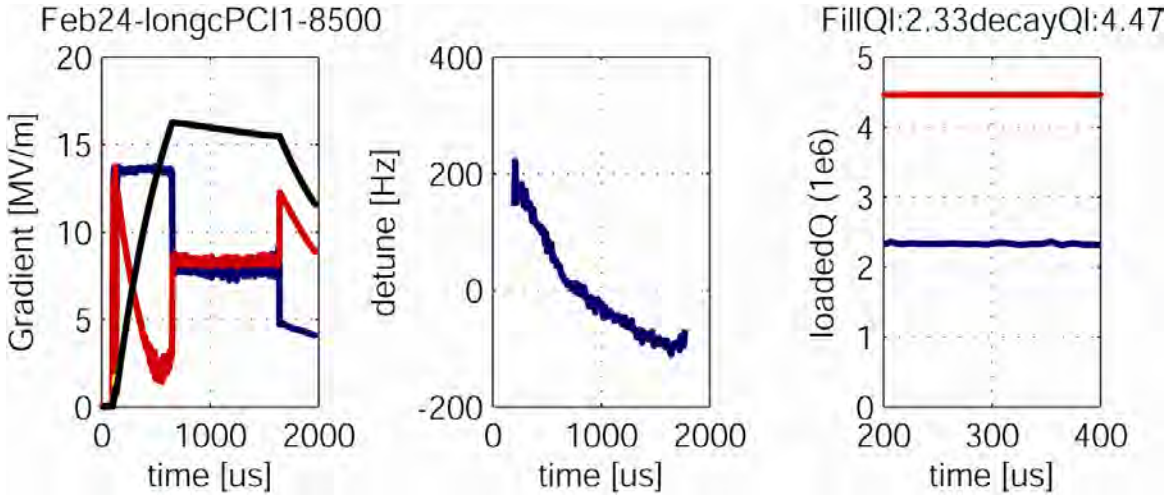

Figure 10-13: RF waveforms (Vcav(black), Vfor(blue), and Vref(red)) in the left, the calculated detuning in the center, and the calculated loaded Q factor in the right.

11 Single-Cavity Operation

11.1 Introduction of Single-Cavity Operation

Cold testing was performed from Jun/2010 to Feb/2011, interspersed by scheduled downtime and additional work on the hardware. The cryomodules were cooled down three times in total. The first cool-down test was carried out from Jun. to Jul. in 2011 in order to measure the thermal and mechanical performance of the cryomodules, and to perform RF tests of all the cavities with low power [11-8, 11-9]. The second test was performed from Sep. to Dec. 2011 and included a check-up of the cavity performance, LFD measurements, LFD compensation by piezo tuners, long-term operation tests, and dynamic loss measurements with high power. The DRFS was tested in a third cold test [11-10] from Jan to Feb 2011 by using two 800 kW klystrons that were placed in the tunnel.

11.2 Low Power RF Tests

In the low power RF tests [11-8] performed by the INFN, FNAL, and KEK teams during the first cool-down, it was found that the tuners attached in TB9ACC011 and MHI-09 were not controllable, and it was not possible to set the frequency of these cavities to 1300.000 MHz, which is the canonical operation frequency. The trouble is presumed to have been caused by tension due to mechanical misalignment of tuner components (a fuller analysis is described in the following sections). Therefore, the simultaneous operation of multiple cavities was limited to seven cavities rather than eight. Results of the low power tuner tests are shown in Figure 11-6.

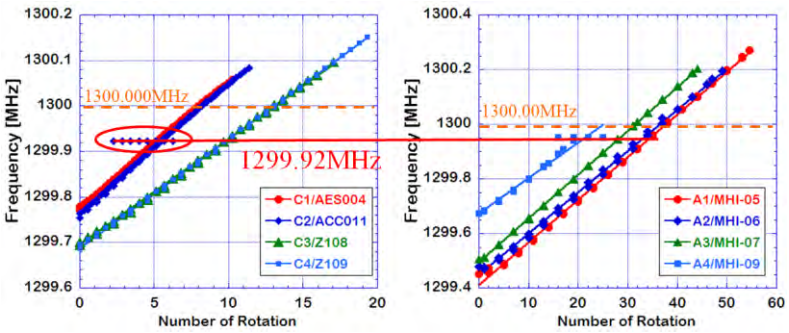

Figure 11-6: The result of the drive test for the motor tuner at low power. The tuner for TB9ACC011 did not work at 2 K, and MHI-09 could not be set to 1300.000 MHz.

On the other hand, adjustment of the variable coupling could be performed for all power couplers, and these were set to the optimum coupling value of 2.4×10^6, which gave rise to a pulse rise-up time of 540 μs, as shown in Figure 11-7.

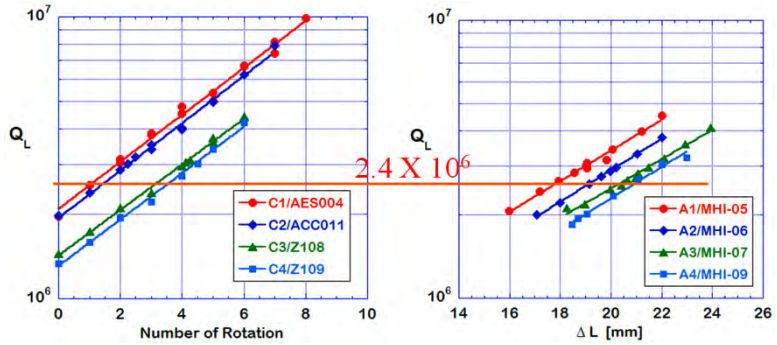

Figure 11-7: The results of the drive test for the variable coupling of the power couplers.

11.2.1 Causes of the TB9ACC011 Slow and Fast Tuner Failures

As described in Section 11.2, the slow tuner installed on cavity TB9ACC011 failed after only a single tuning cycle (Figure 11.6). In addition, one of the two piezo-actuators installed on the same cavity discharged at approximately half the nominal maximum operating voltage of 200 V and the TB9ACC011 fast tuning range was smaller than had been expected.

Following the slow tuner failure, clicking noises from inside the cryomodule were audible when the TB9ACC011 motor was operated. This was an indication that the problem was not with the motor but was located in the mechanical linkage between the motor and the tuner. However, there was no obvious method to narrow the list of possible causes for the fast tuner failure prior to disassembly. As the cryomodule was dismantled the reasons for both the failures became fully apparent.

The TB9ACC011 slow tuner had failed because the two M3 set screws in the shaft connecting the motor and the harmonic drive had worked loose, which was presumably due to vibrations during operation. One of the two screws was completely loose. The second was unable to transmit the full torque of the motor and was allowing the shaft to slip (Figure 11.2.1-1).

Following the operational failure of the TB9ACC011 slow tuner, but prior to the post-mortem, a number of slow tuners were subject to an exhaustive battery of tests in the FNAL Horizontal Test Stand. These tests identified the setscrews as a possible point of failure and also identified a number of other weak points. Among the modifications made to the slow tuner design as a result of these tests, the set screws were replaced by a pin through the shaft to prevent the type of slippage that led to the TB9ACC011 slow tuner failure.

A visual inspection of the TB9ACC011 piezo actuators during disassembly showed that the two brass end caps holding the actuator stack were not well aligned. Misalignment of the caps can result in the transmission of excessive shear forces onto the actuator stack (Figure 11.2.1-2). Further inspection revealed that the actuator installed on the coupler side of the cavity had fractured on one edge (Figure 11.2.1-3). The physical damage to the stack could account for the discharges observed during operation and for the reduced tuning range.

The possibility of this type of failure had been recognized even before the failure occurred and FNAL had modified the fast tuner design to prevent it. Piezo-actuators installed on the cavities assembled for CM2 were fully encapsulated to prevent the transmission of any shear forces (Figure 11.2.1-4). Unfortunately, the modified design had not been completed by the time TB9AES004 and TB9ACC011 were shipped to KEK.

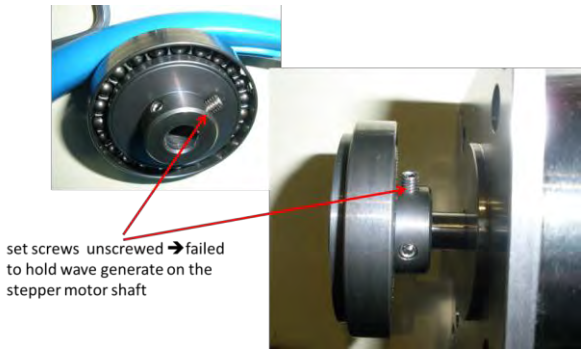

Figure 11.2.1-1: Set screws that connect the motor shaft to the harmonic drive. One of these had worked completely loose, and the remaining screw was not able to transmit the full torque of the motor.

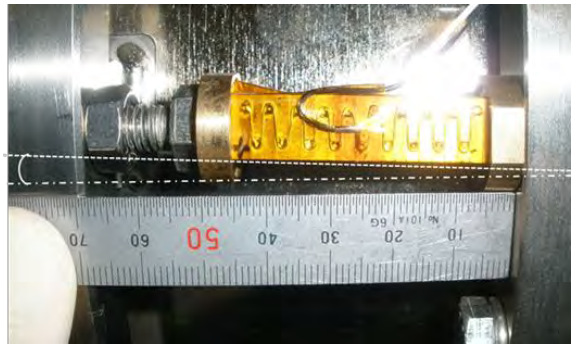

Figure 11.2.1-2: The brass end-caps holding the piezo-actuator. These were not well aligned with the result that shear forces were applied to the actuator stack.

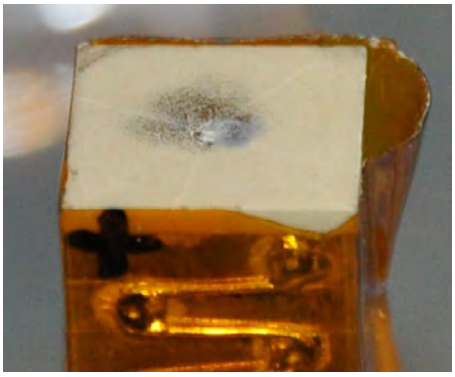

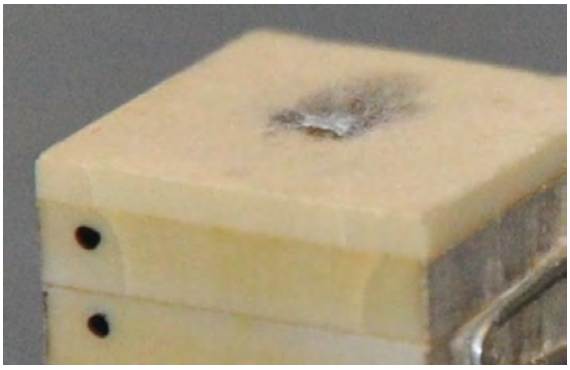

Figure 11.2.1-3: Fracture damage to the end plate of the piezo as a result of excessive shear forces.

Figure 11.2.1-4: Fully encapsulated piezo-actuators installed on the FNAL CM2 cavities. Encapsulation prevents the transmission of shear forces to the piezo stack.

11.2.2 The Causes of the MHI-09 Slow Tuner Failure

The slow tuner of MHI-09 failed during the first excursion test (Figure 11.6). The rotation of the motor became slow and finally stopped at 1299.95 MHz. After several attempts, the tuner ceased to work even when the motor was rotating. During the intermediate warm-up in Aug. 2010, a crash of the rotation feeder into the cryomodule inside was observed. A check of the motor gear system was done using a fiberscope

from the motor axis, as shown in Figure 11.2.2-1. The access flange was also opened, and the thermal shield portion was removed so that the gear system could be checked directly. Visual and function tests were performed and the gear system did not appear to be damaged, even though there was a point at which the gears tended to stick. Even after the rotation feeder was replaced with a stronger one, the tuner continued to stick during the second cool-down. After disassembly, the mechanical tuner of the MHI-09 cavity was carefully checked. When the fixed bolts of the slide-jack were loosened from the thick flange, the movement of the tuner mechanism became smooth and did not stick. In this case there was a gap between the flange and the slide-jack. These gaps were 0.55 mm to 0.6 mm in size, as shown in Figure 11.2.2-2. They were caused by a flange bending deformation, which occurred during welding. Figure 11.2.2-3 shows these gaps. These welding deformations could be minimized by the improvement of the welding procedure, in the future cavity fabrication.

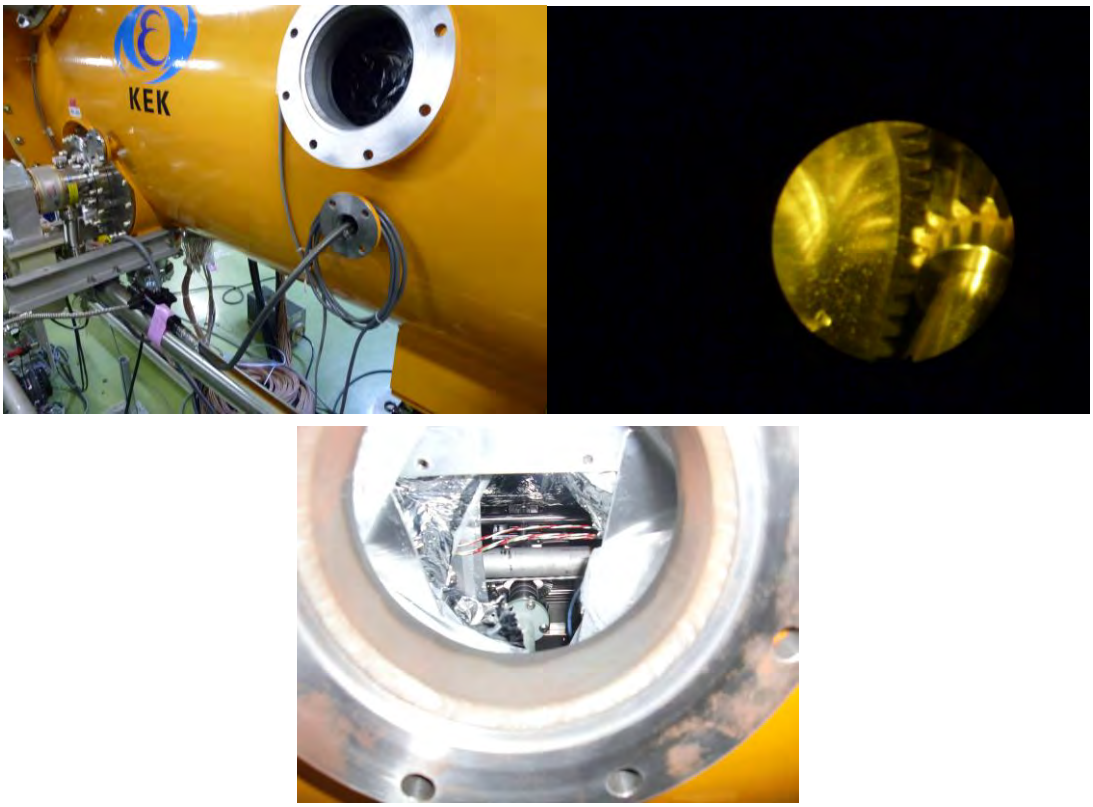

Figure 11.2.2-1: Visual check of tuner (top-left) during intermediate warm-up. From the tuner shaft the fiberscope viewer was inserted and the gear mechanism was checked (top-right). The maintenance port was opened and a portion of the thermal shield was removed. The gear mechanism was also checked by this method (bottom).

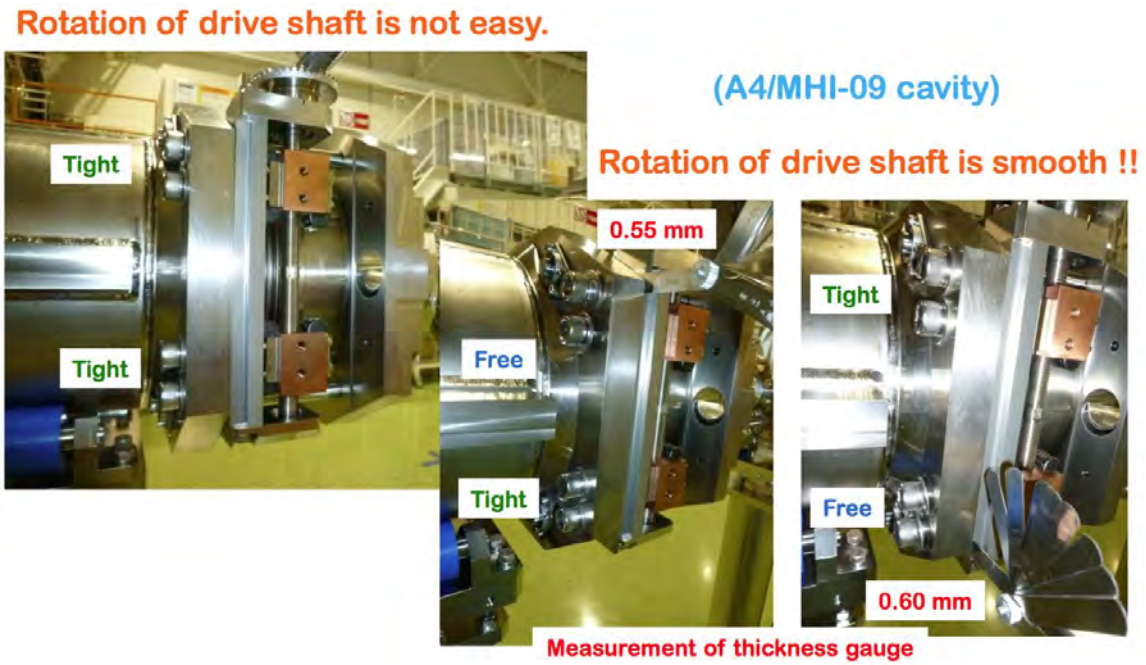

Figure 11.2.2-2: The thickness of the gap caused by bending of the tuner mount flange was checked after disassembly of the cryomodule.

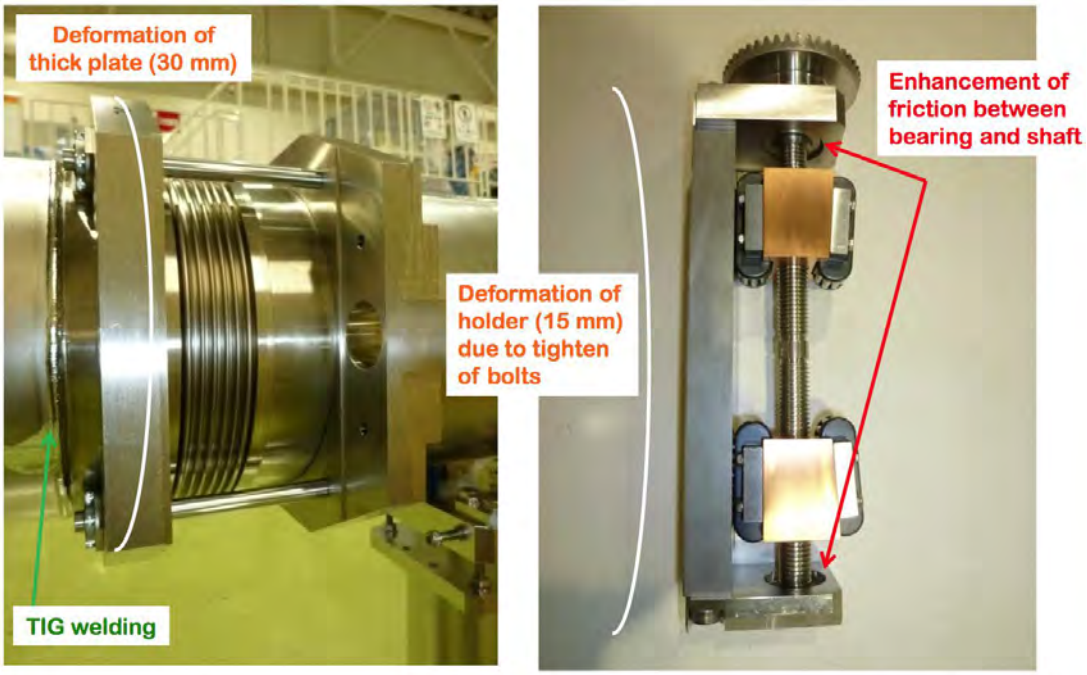

Figure 11.2.2-3: The deformation of the tuner mount flange caused by heat during welding. The jack mechanism was force to align with the deformed flange, which increased the friction of the gear.

11.3 Cavity Performance & Issues

After the second cool-down, cavity conditioning with high power was carried out by members of the groups from DESY and KEK. The achieved gradient values in vertical and cryomodule tests are shown in Figure 11-8. The maximum average gradient is 30.0 MV/m during vertical testing, 27.7 MV/m for single cavity operation, and 26.0 MV/m for the simultaneous operation of seven cavities (presented later) during the cryomodule tests.

The performance of MHI-06 drastically improved from its result in the vertical test, and the achieved gradient was 38 MV/m. In contrast, the gradient of two of the cavities (TB9ACC011 and Z108) was significantly lower in the cryomodule than in previous tests. Issues during the assembly processes or transportation to KEK are suspected to be the cause of this reduced gradient. This problem should certainly be addressed for the ILC. The performance of MHI-05 (in particular, the performance of the input coupler) also degraded during the adjustment for the FB control due to the abnormally high input power. Figure 11-9 shows the performance degradation of MHI-05. The vacuum level of the input coupler on the warm side was unsteady due to the abnormally high power. After several vacuum bursts, the maximum gradient was limited to around 20 MV/m. These difficulties were caused by the incorrect operation during FB control tuning.

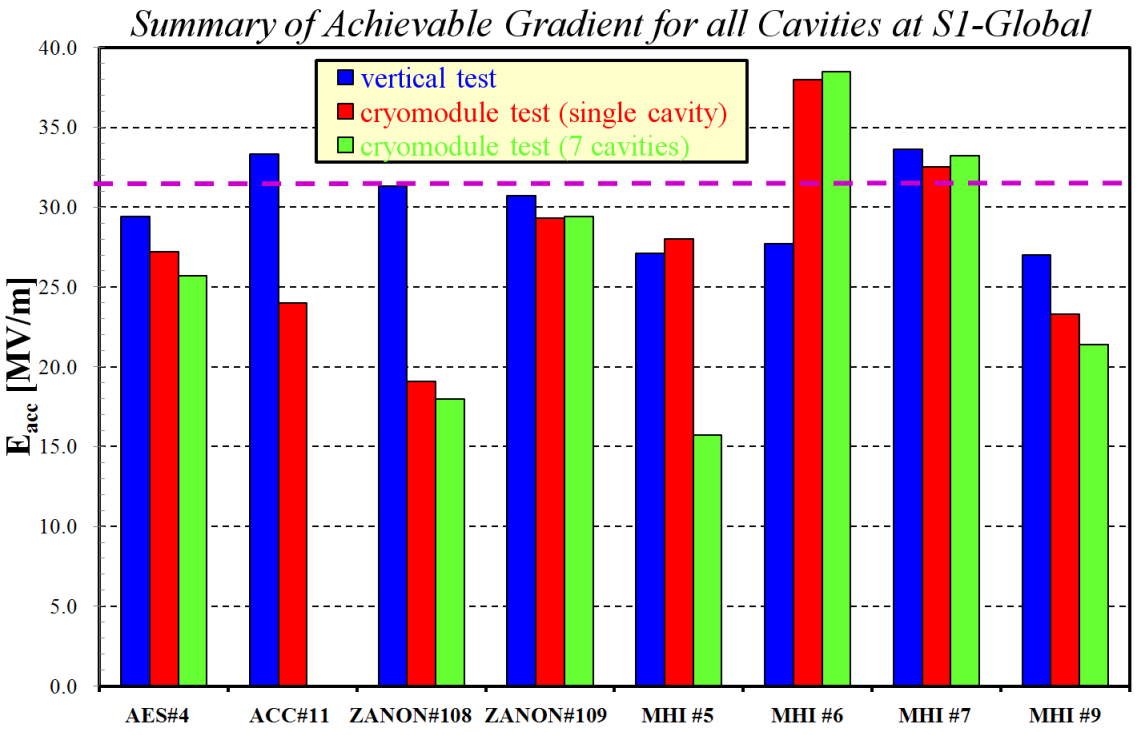

Figure 11-8: The achieved gradient values for eight cavities in vertical and cryomodule tests. The maximum average gradient is 30.0 MV/m during a vertical test, 27.7 MV/m for single cavity operation, and 26.0 MV/m for simultaneous operation of seven cavities during a cryomodule test. The purple dotted line shows 31.5 MV/m, which corresponds to the ILC specification.

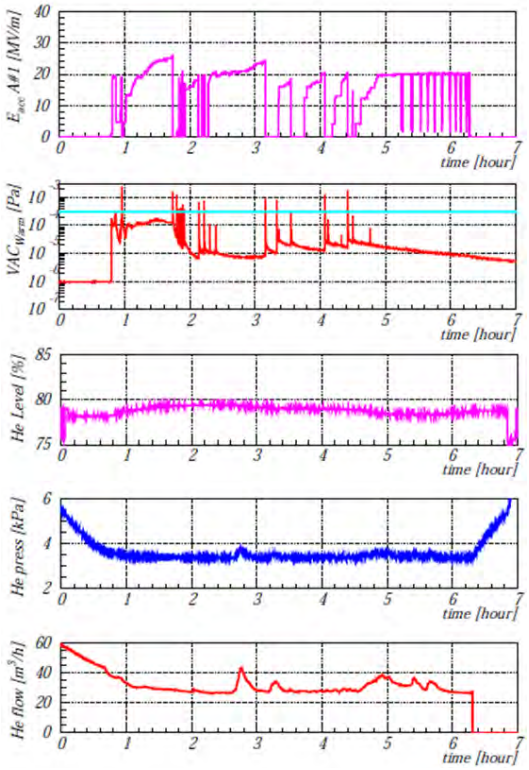

Figure 11-9: The performance degradation for MHI-05 during the adjustment of FB control.

11.4 Power Coupler Conditioning

All power couplers were RF conditioned at room temperature. A standing wave remains in the power coupler due to total reflection. The achievable power was 500 kW for a pulse width of 500 μs and 200 kW for 1500 μs at a repetition rate of 5 Hz. The average conditioning time was 21 h for TTF-III-type couplers and 13 h for STF-II-type couplers. The difference between these times is probably due to the structure of the RF window. None of the RF windows experienced any vacuum leaks during the S1-Global experiments.

11.5 Measurement of Mechanical Vibration with Piezo

The mechanical vibration modes were measured during low power operation for all cavities. In addition, for MHI cavities, measurements were conducted by using a piezo response during high-power operation. The observed dominant mechanical modes exhibited considerable variation, as shown in Figure 11-10. This is presumably due to the different mechanical constraints. The dominant modes found are as follows: 540 Hz for MHI-05, 220 Hz for MHI-06, 325 Hz for MHI-07, 210 Hz for MHI-09, 179 Hz for TB9AES004, 204 Hz for TB9ACC011, 260 Hz for Z108, and 245 Hz and 252 Hz for Z109. The first order mechanical vibration mode is known to have a frequency of around 200 Hz.

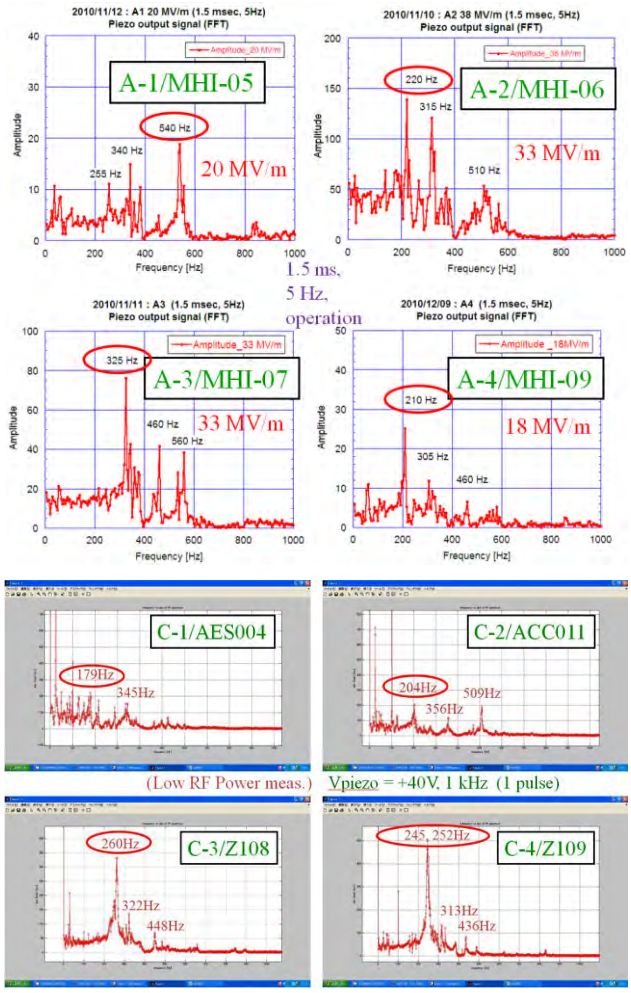

Figure 11-10: The result of the mechanical vibration modes measured at high power for Cryomodule-A (top four plots), and at low power for Cryomodule-C (bottom four plots).

11.6 LFD Measurement

After conditioning, the LFD measurement for each cavity was carried out by members of the FNAL and KEK teams. The KEK team used the 'pulse shortening' measurement method, which is the standard method at KEK. Figure 11-11 shows an example of the pulse shortening method for MHI-06 with steps of 50 μs. Figure 11-12 shows examples that illustrate the linear fitting range at the pulse end that can be used for the evaluation of Q_L and the detuning frequency (Δf) with pulse widths of 1500 μs and 450 μs. The linear fitting range is approximately 40 μs from the pulse end for both the pulses. Figure 11-13 shows the results of the LFD measurement at the maximum gradient for every cavity. The points at the pulse width of 0.0 μs are values extrapolated using a fit of the measured points to a quadratic curve in the rise-up period.

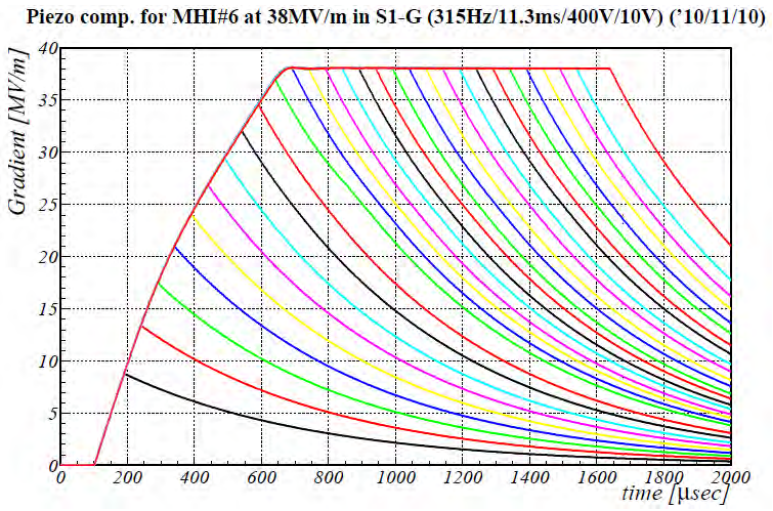

Figure 11-11: An example of measurements taken with the pulse shortening method. Each time step is 50 μs.

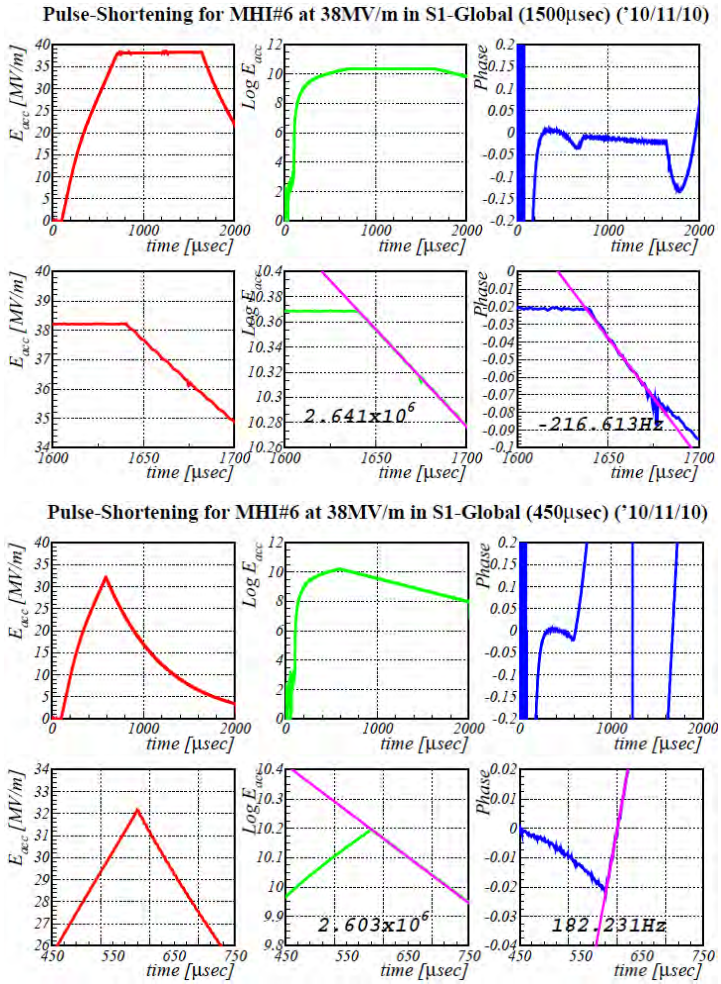

Figure 11-12: Examples showing the linear fitting range for pulse widths of 1500 μs (top six plots) and 450 μs (bottom six plots). The red line shows the accelerating gradient, green shows the logarithmic gradient, blue shows the phase for MHI-06, and the purple line is the fitted line.

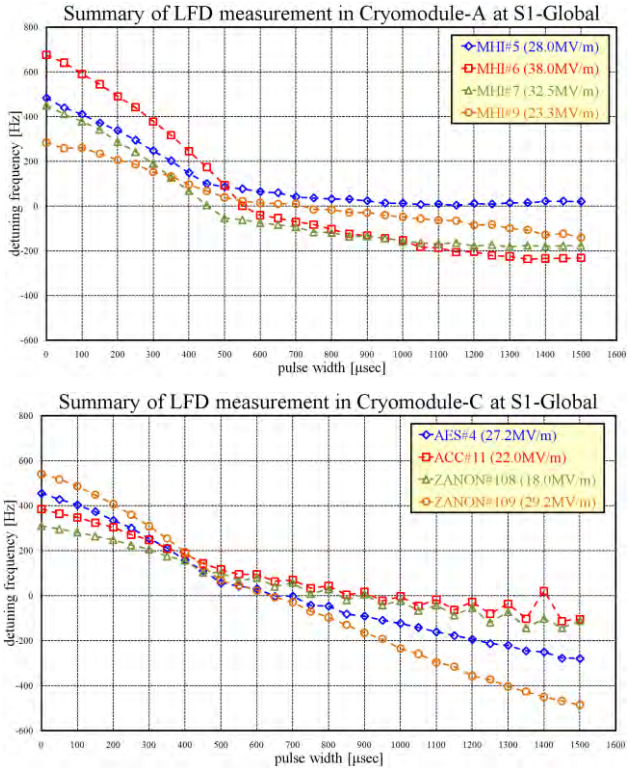

Figure 11-13: Result of LFD measurements at the maximum gradient for every cavity. Top plot is for Module-A cavities, bottom plots for Module-C cavities.

The detuning frequency for three periods, i.e., rise-up, flat-top, and full-pulse, was evaluated in order to compare the stiffness of all the cavities. Figure 11-14 shows the correlation between the detuning frequency for the three periods and the square of the gradient. From the slope of a linear fit to these data, it is possible to evaluate the cavity stiffness, as shown in Figure 11-15. The MHI cavities are found to be stiffer than the others. The effect is remarkable in the flat-top period, while the difference is smaller during the rise-up period. According to the 'two modes model' analogy [11-11], high stiffness of the end plate of a helium jacket is much more effective in the slow mode (several hundred hertz). A comparison of the stiffness ratios, which are normalized to that of MHI-07, is shown in Figure 11-16.

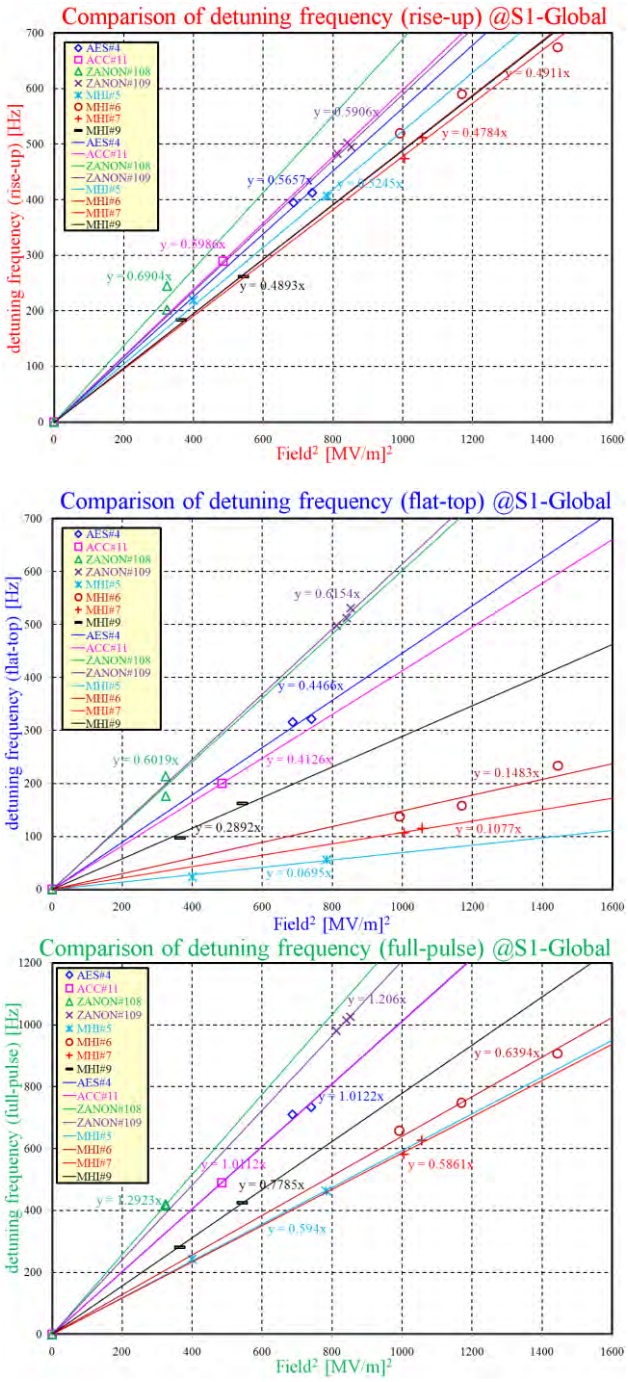

Figure 11-14: Correlation between the detuning frequency and the square of the field for rise-up(top), flat-top(middle), and full-pulse(bottom) including a linear fit to each set of data.

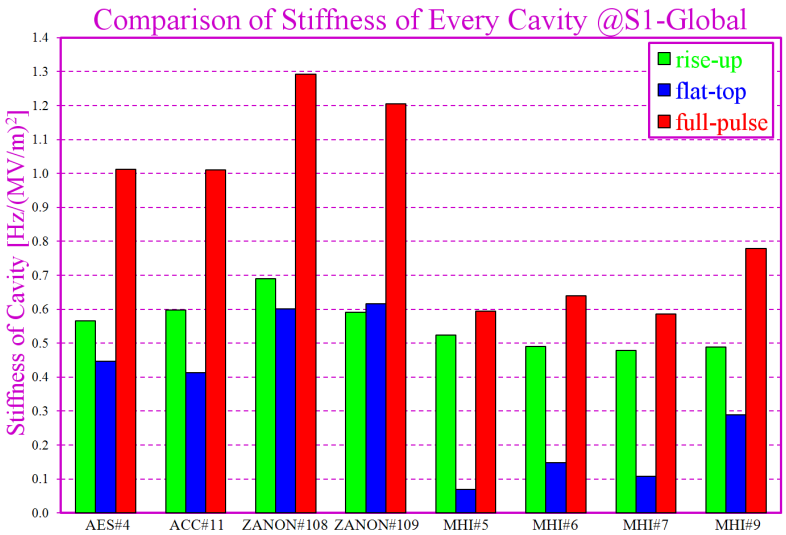

Figure 11-15: Comparison of the slopes from the linear fits to the rise-up, flat-top, and full-pulse data sets.

Cavity	AES004	ACC011	Z108	Z109	MHI-05	MHI-06	MHI-07	MHI-09
rise-up	1.16	1.18	1.34	1.21	1.09	0.97	1.00	0.98
flat-top	3.99	3.90	5.66	5.44	0.71	1.59	1.00	2.72
full-pulse	1.73	1.73	2.20	2.06	1.01	1.09	1.00	1.33

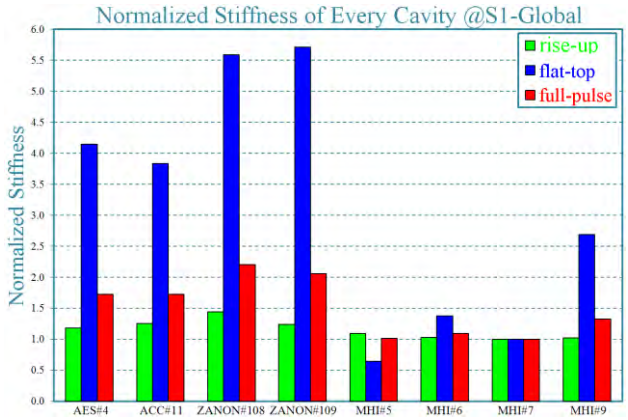

Figure 11-16: Comparison of the ratio of the stiffness normalized to that of MHI-07.

11.7 Compensation of LFD by Piezo

Both the FNAL and KEK teams carried out LFD compensation of the cavities using piezo-actuators. The KEK team performed a ”single pulse compensation” that employs a sine curve, and this method was used for STF Phase-1 [11-11]. The FNAL team introduced the “adaptive compensation method,” a new method that has been presented in recent papers [11-12]. Both the compensation methods were successful.

11.7.1 Compensation by the Pre-determined Pulse Method

In the LFD compensation method employed by the KEK team, which was suitable for detuned cavities, a pulse corresponding to one period of a sine curve was applied to the piezo before the RF pulse, as shown in Figure 11-17. The piezo drive has four adjustable parameters, that is, the drive frequency, delay time, pulse height, and pulse offset. Figure 11-18 shows the results of compensating six cavities using this pulse shortening method. The peak-to-peak excursion of the detuning frequency across the flat-top of the pulse was introduced as a measure of the compensation, which is a similar approach to that taken during STF Phase-1 [11-11]. Figure 11-19 shows the correlation between the peak-to-peak excursion of the detuning frequency and the gradient for the best three sets of results obtained using the pulse shortening compensation method. After compensation, the MHI cavity still has a smaller peak-to-peak detuning frequency excursion during the flat part of the pulse. This means that the MHI cavity has a stiffer structure than the other cavities.

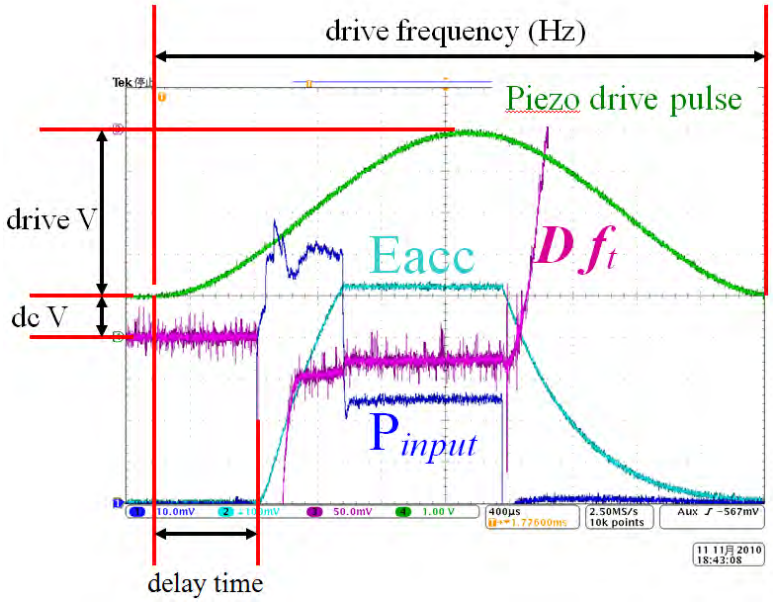

Figure 11-17: One pulse of the sine curve added to the piezo for LFD compensation. The dark blue trace shows the input power, light blue shows the accelerating gradient, purple shows the phase in the cavity, and green shows the drive pulse to a piezo. Four adjustable parameters exist, and these are the drive frequency, pulse height, pulse offset, and delay time for the piezo drive.

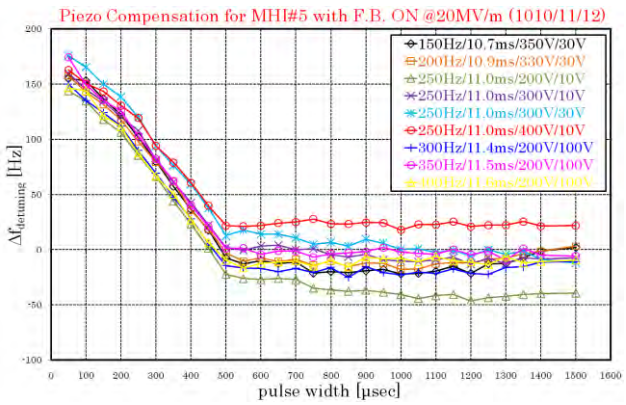

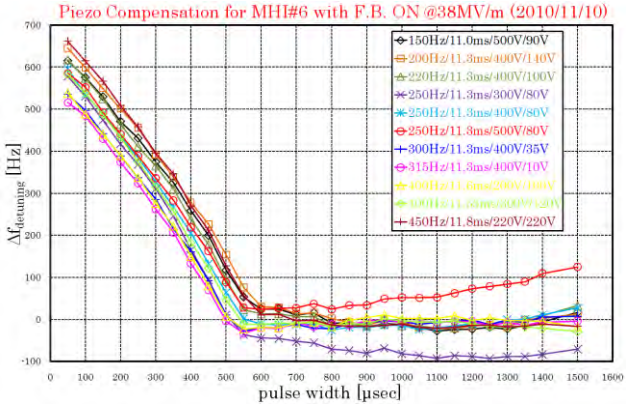
Piezo Compensation for MHI#6 with F.B. ON @38MV/m (2010/11/10)
150Hz/11.0ms/500V/90V
200Hz/11.3ms/400V/140V
220Hz/11.3ms/400V/100V
250Hz/11.3ms/300V/80V
250Hz/11.3ms/400V/80V
250Hz/11.3ms/500V/80V
300Hz/11.3ms/400V/35V
315Hz/11.3ms/400V/10V
450Hz/11.8ms/220V/220V
Δf_detuning [Hz]
pulse width [μsec]

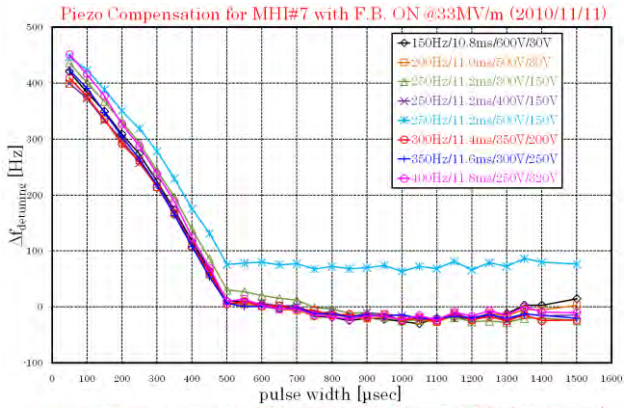
Piezo Compensation for MHI#7 with F.B. ON @33MV/m (2010/11/11)
150Hz/10.8ms/600V/30V
250Hz/11.2ms/300V/150V
250Hz/11.2ms/400V/150V
250Hz/11.2ms/500V/150V
300Hz/11.4ms/350V/200V
350Hz/11.6ms/300V/250V
400Hz/11.8ms/250V/220V
Δf_detuning [Hz]
pulse width [μsec]

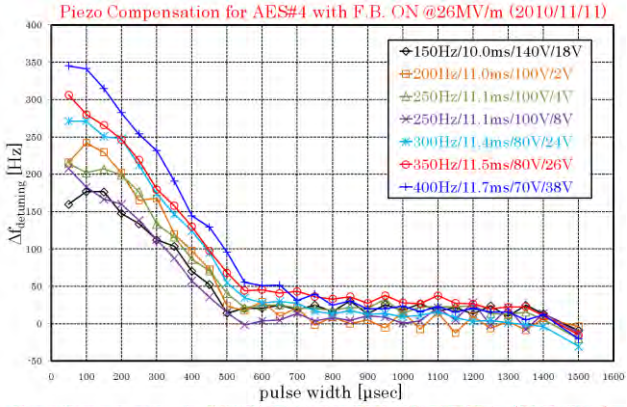
Piezo Compensation for AES#4 with F.B. ON @26MV/m (2010/11/11)
150Hz/10.0ms/140V/18V
200Hz/11.0ms/100V/2V
250Hz/11.1ms/100V/4V
250Hz/11.1ms/100V/8V
300Hz/11.4ms/80V/24V
350Hz/11.5ms/80V/26V
400Hz/11.7ms/70V/38V
Δf_detuning [Hz]
pulse width [μsec]

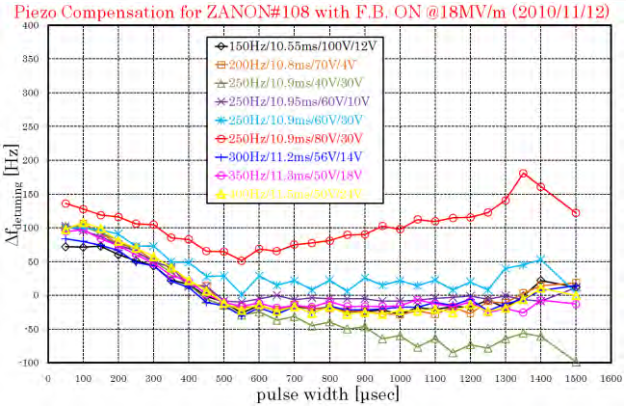
Piezo Compensation for ZANON#108 with F.B. ON @18MV/m (2010/11/12)
150Hz/10.55ms/100V/12V
200Hz/10.8ms/70V/4V
250Hz/10.9ms/40V/30V
250Hz/10.95ms/60V/10V
250Hz/10.9ms/60V/30V
250Hz/10.9ms/80V/30V
300Hz/11.2ms/56V/14V
350Hz/11.3ms/50V/18V
Δf_detuning [Hz]
pulse width [μsec]

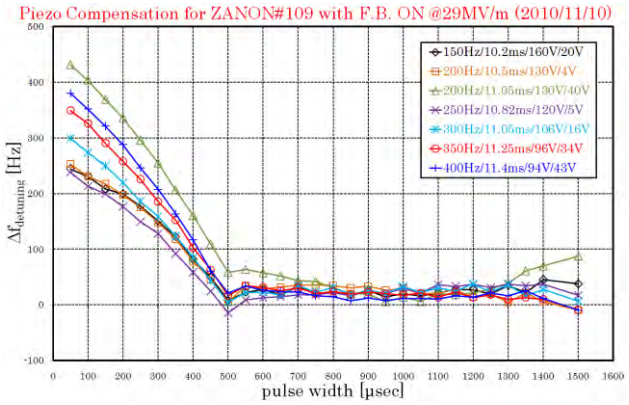

Figure 11-18: Results of the piezo compensation of six cavities. The varied parameters listed in the legend are the drive frequency, delay time, pulse height, and pulse offset for the sine curve pulse (from left to right).

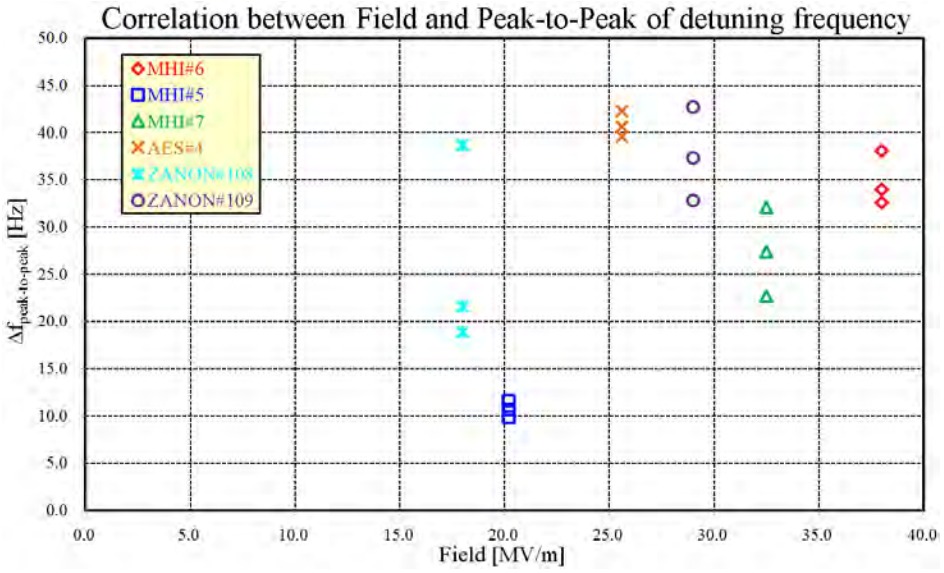

Figure 11-19: The correlation between the peak-to-peak excursion of the detuning frequency during the flat part of the pulse and the field gradient. The three best sets of results are shown.

11.7.2 Adaptive LFD Compensation

In addition to the standard Lorentz force detuning compensation described above, an adaptive feed-forward method developed at FNAL for CM1 was employed to compensate for the detuning in six of the eight S1-Global cavities. The coupler conditioning on the other two cavities was not fully complete at the time of this test.

The adaptive feed-forward procedure first measures the detuning response of each individual cavity to a series of small amplitude, short duration piezo stimulus pulses and to changes in the DC bias applied to the piezo. The matrices of stimulus and response data were then inverted using Least Squares to obtain the small-signal cavity detuning response for any arbitrary piezo waveform and to determine the piezo waveform required to cancel out any arbitrary detuning profile.

The feed-forward method allows the detuning compensation process to be fully automated. It can track changes in cavity gradients without the need for operator intervention; it can also automatically adjust the

piezo bias to correct for changes in the cavity resonance frequency caused by changes in the pressure of the surrounding helium bath and any other sources that may slowly change the detuning.

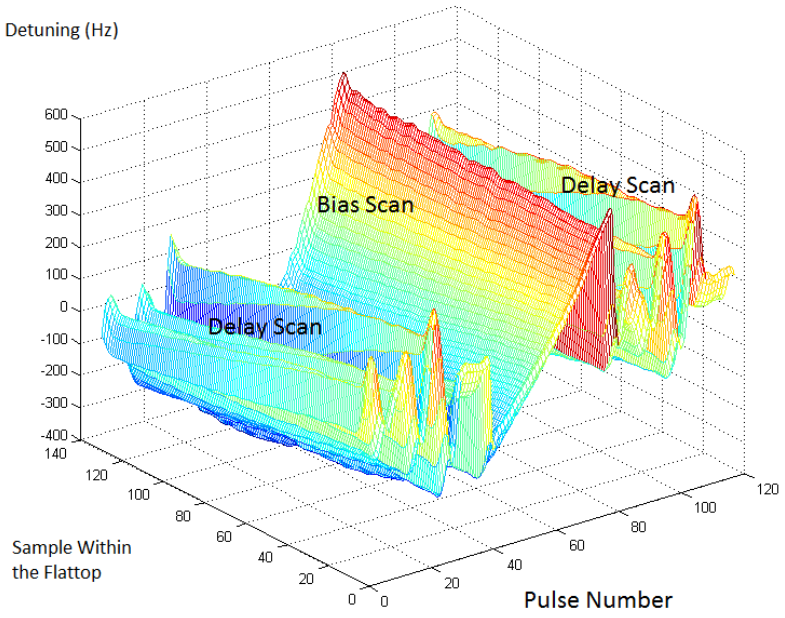

Figure 11-20: 3D Visualization of the Cavity Detuning Response Matrix.

Figure 11-20 shows a 3D visualization of the matrix of detuning responses of the S1-Global cavity C4. During the first 40 RF pulses, the piezo is excited with a series of small-amplitude positive impulses at different delays. During the next 40 pulses the piezo DC bias voltage is varied over the operating range of the actuator. During the final 40 pulses the piezo is excited with a series of negative impulses.

As the piezo bias voltage is varied across its operating range, the detuning of the cavity responds approximately linearly across the entire flat-top portion. In contrast, when short piezo stimulus pulses are applied, the detuning at any given point during the RF pulse depends on the delay between the stimulus pulse and the RF pulse and on the mechanical response of the cavity to the stimulus. As the delay between the stimulus and the RF pulse is varied, the detuning shifts accordingly.

Each of the detuning response waveforms can be shifted in such a way that all the piezo pulses are aligned in time. Averaging the shifted waveforms over all the pulses yields an estimate of the cavity detuning impulse response, as shown in Figure 11-21. The detuning response estimated in this way is in good qualitative agreement with the CW detuning measurements for each distinct S1-Global cavity design. The response of the DESY cavity (C3) was dominated by a prominent mechanical resonance near 200 Hz. The KEK cavities (A2 and A3) were deliberately designed to be much stiffer and to damp much more rapidly. The response of the INFN/FNAL blade-tuner/cavity (C1) combination lies somewhere in the middle.

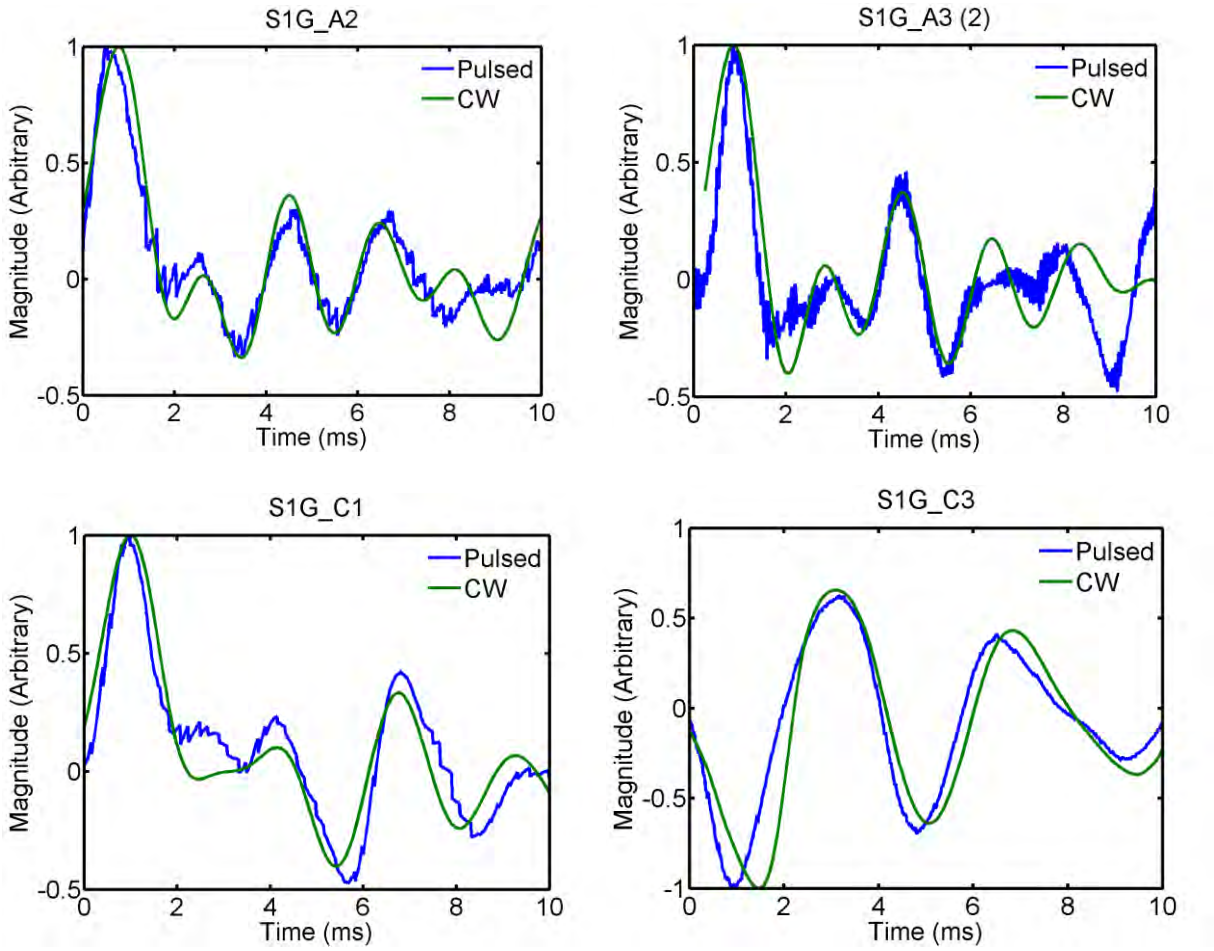

Figure 11-21: Comparison of the detuning impulse response measured during pulsed and CW operation for different S1-Global cavity designs.

The stimulus procedure allows the mechanical response of each cavity to be characterized in situ during pulsed operation without the need to reconfigure the RF system for CW operation.

Once the detuning response of each cavity has been characterized, a suitable piezo compensation waveform is calculated. Figure 11-22 shows an example of the piezo waveforms applied to the S1-Global cavity A2. The spectral content of the compensation pulse reflects the mechanical response of the cavity design. The detuning in the DESY cavities can be compensated for using a relatively slow waveform with a single dominant frequency. The KEK cavities require a much faster waveform to deal with the stiffer design and the INFN/FNAL cavity combinations are again somewhere in between.

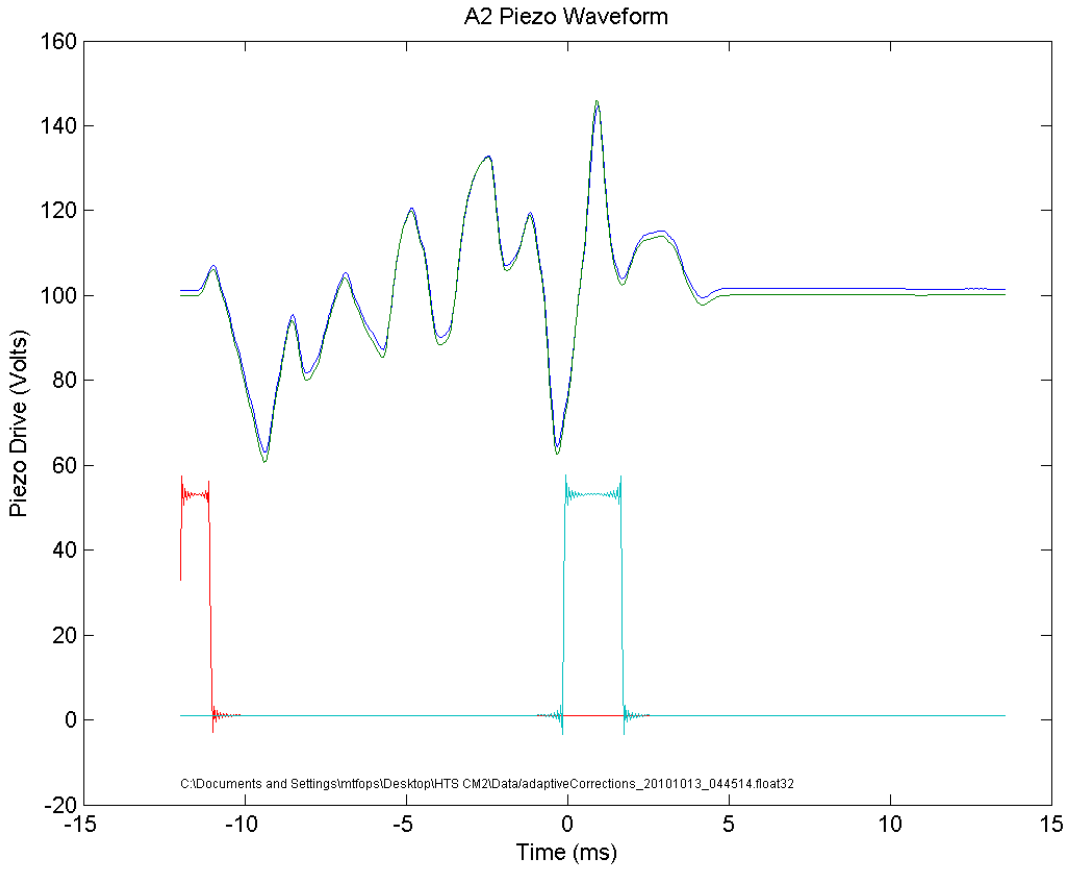

Figure 11-22: Example of an adaptive feed-forward piezo waveform.

Figure 11-23 shows the detuning waveforms for multiple pulses following compensation in each of the cavity designs tested using the adaptive feed-forward method. With the exception of the end slide-jack design, the residual detuning is less than or comparable to the pulse-to-pulse variation of the detuning. Because the test durations were limited, it was not possible to investigate in detail the reason for the difference between the detuning response of the end slide-jack and other designs. However, it may well be due to the limitations of the current and frequency response of the piezo driver supplied by FNAL that was used during these tests rather than any inherent limitation of the end slide-jack design.

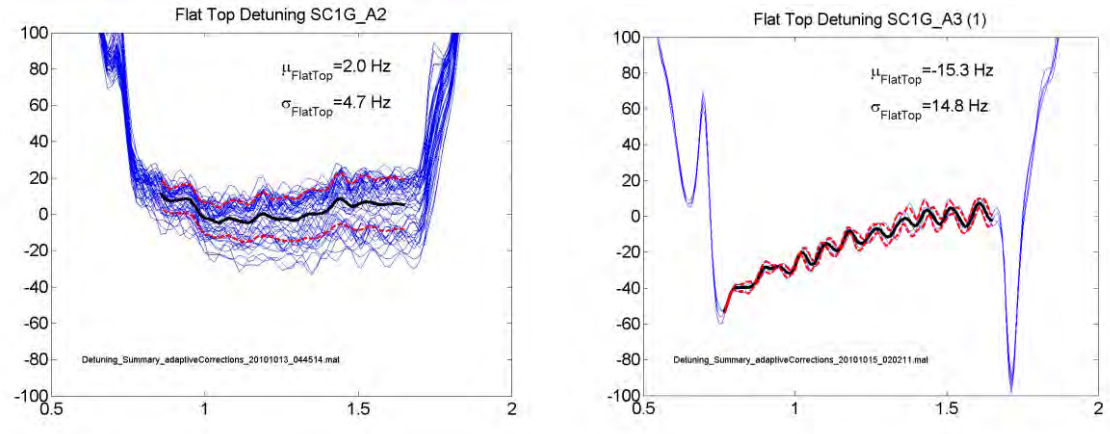

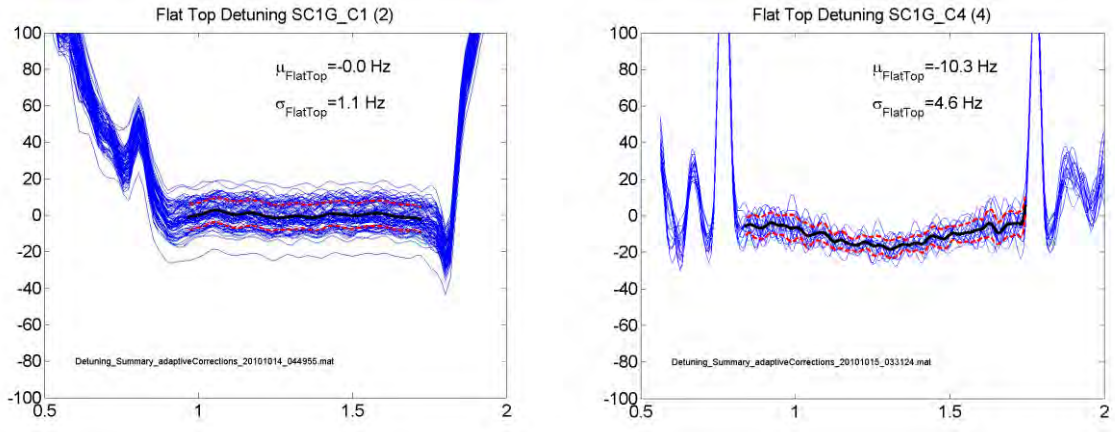

Figure 11-23: Comparison of the detuning over multiple pulses in different S1-Global cavity designs following adaptive feed-forward compensation.

The mean and standard deviation of the average detuning during the flat-top of the pulse were used to estimate the residual bias and detuning, respectively, for each cavity tested, as shown in Figures 11-24 and 11-25. Measureable non-zero constant offsets in the detuning remained following the adaptive compensation. Subsequent studies at FNAL/CM1 showed that this offset could be suppressed to a small fraction of a Hertz by adding an integral term to the feed-forward compensation loop used to control the piezo bias. The residual RMS detuning following compensation was less than 15 Hz in all cavities regardless of their design or gradient. With the exception of the end slide-jack design, which may not have received an adequate piezo drive signal, the residual detuning ranged between 2 Hz and 8 Hz.

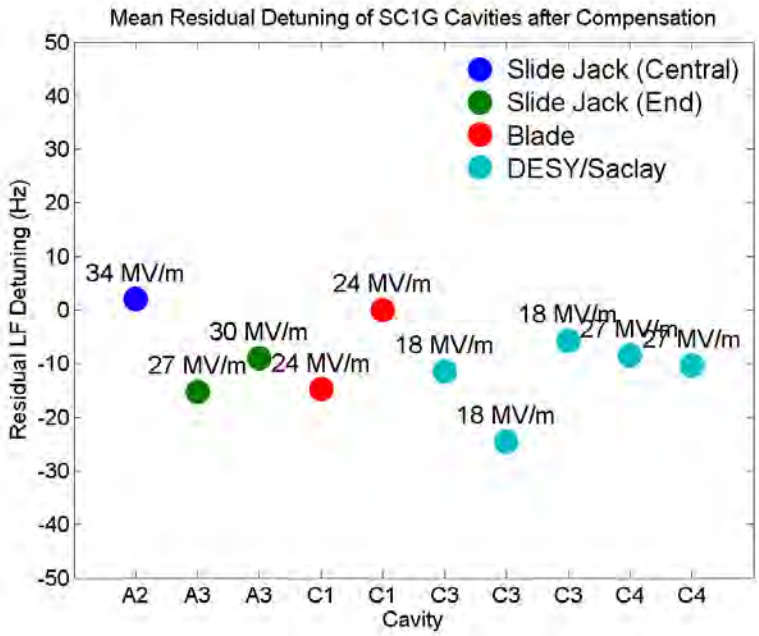

Figure 11-24: Comparison of the average detuning offset during the flat-top in different S1-Global cavity designs following adaptive feed-forward compensation.

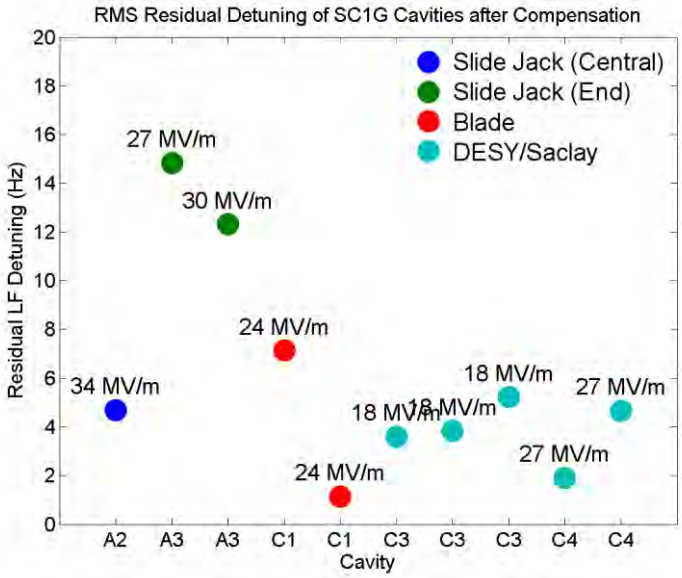

Figure 11-25: Comparison of the average residual detuning during the flat-top in different S1-Global cavity designs following adaptive feed-forward compensation.

Adaptive feed-forward compensation successfully suppressed the Lorentz force detuning in each of the S1-Global cavities, which were tested to the point where the residual detuning should have had no significant impact on the design, the cost, or operation of a machine such as the ILC.

11.8 Long Term Operation of Single Cavities

- MHI-06 cavity

The long-term operation of single cavities was tested many times during the S1-Global cryomodule tests. The longest period of operation was over 4 hours for MHI-06 at 38.0 MV/m with the feedback and piezo operating, as shown in Figure 11-26. A clear decrease in Q_L was observed at the end of the run, and this decreased approximately 8.3% from the initial value. However, the decrease stopped during the last 10000 pulses with the piezo operating.

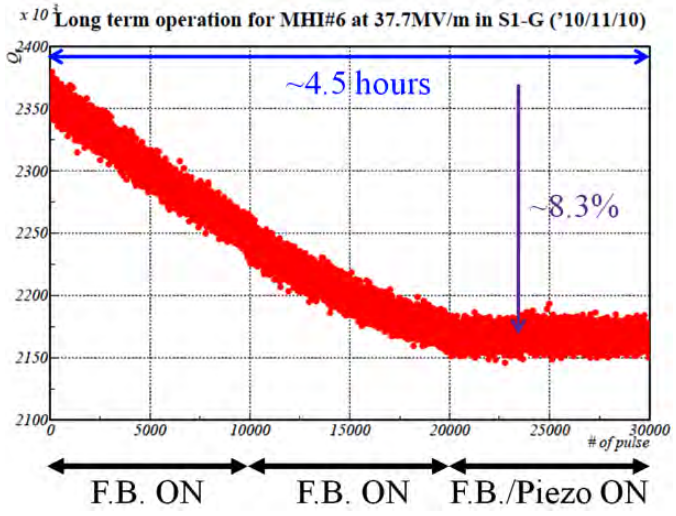

Figure 11-26: Behavior of Q_L during the long-term operation of MHI-06.

- Z109 cavity
  The long-term operation of cavity Z109 was also carried out at 28 MV/m for about 15 min using feedback control with Piezo operation. Figure 11-27 shows the behavior of Q_L and Δf during this operation. A slight decrease in Q_L was observed as was observed for cavity MHI-06, and the root mean square of Δf was 4.3 Hz, which confirmed that the cavity was operating stably.

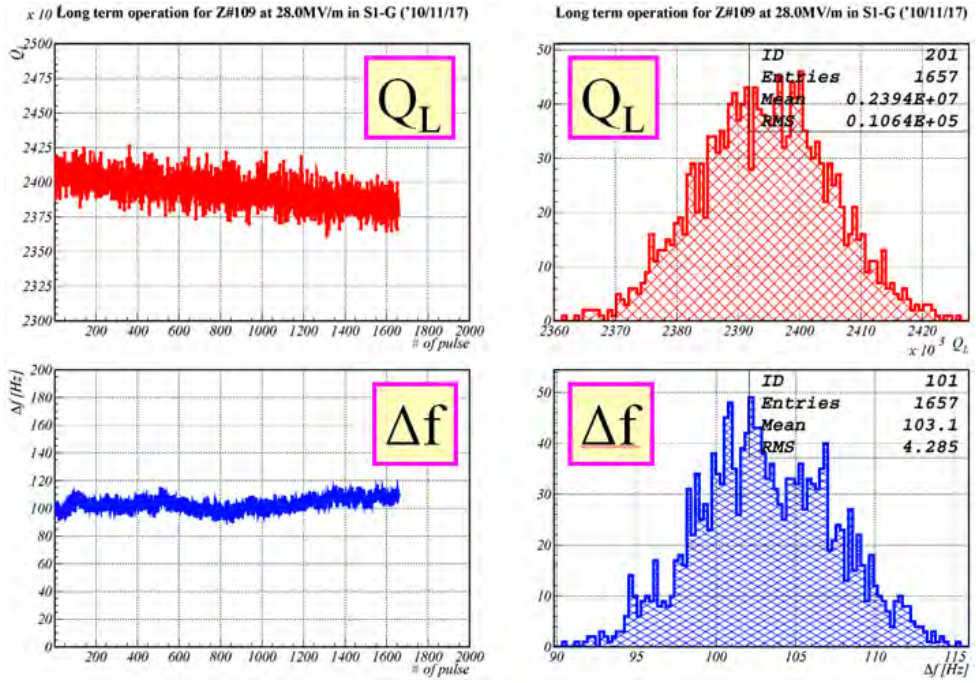

Figure 11-27: Behavior and histogram of Q_L and Δf during the long-term operation of Z109.

11.9 Summary of Single Cavity Operation

The following list is a summary of the single cavity operation tests and results in the cryomodule.

- Gradient performance degradation in two cavities (TB9ACC011 and Z108).
- Gradient performance improvement in one cavity (MHI-06).
- One tuner did not work after cool-down (TB9ACC011).
- One tuner could not be set to 1300.000 MHz due to a limited stroke (MHI-09).
- The input coupler performance was degraded by operating at an excessively high power (MHI-05).
- All of the variable couplers were adjusted to the optimum coupling of 2.4×10^6.
- Stable long-term operation of the cavities was demonstrated.
- The stiffer structure of the MHI cavity was demonstrated.
- No difference was observed in the performance of the three types of tuners.
- LFD compensation by piezo was successfully demonstrated for the pulse method and the adaptive feedback method.
- Different responses to mechanical vibrations were observed in the cavities.

12 Multi-Cavity Operation

12.1 Operation of Seven Cavities with Vector-sum Feedback Control

In the final stage of the experiment, the single 5 MW klystron provided power to all eight cavities, and the performance of its operation with vector-sum feedback control was evaluated [12-1]. During this operation, one cavity (C-2) could not be used for vector-sum control because of the mechanical failure of its tuner. The input power to the cavities was adjusted by the tunable hybrids and the variable tap-offs [12-2] to yield the maximum gradient for each cavity. The detuning of each cavity during the RF pulse flat-top (1 ms) was set near 0 Hz by using the piezo tuners.

Measurements taken during the vector-sum feedback control operation of seven cavities are shown in Figure 12-1. The average gradient of seven cavities after input power optimization for each cavity was 26 MV/m. Because the average of each cavity's quench limit was 26.7 MV/m, operation near the quench limit was achieved for each cavity. The amplitude and phase stabilities were 0.005% (RMS) and 0.015° (RMS), respectively, which are consistent with the results (0.007% [RMS] in amplitude and 0.018° [RMS] in phase) of the four cavity operation in STF Phase 1 [12-3] and satisfy the ILC requirements of stabilities of 0.07% (RMS) in amplitude and 0.24° (RMS) in phase [12-4].

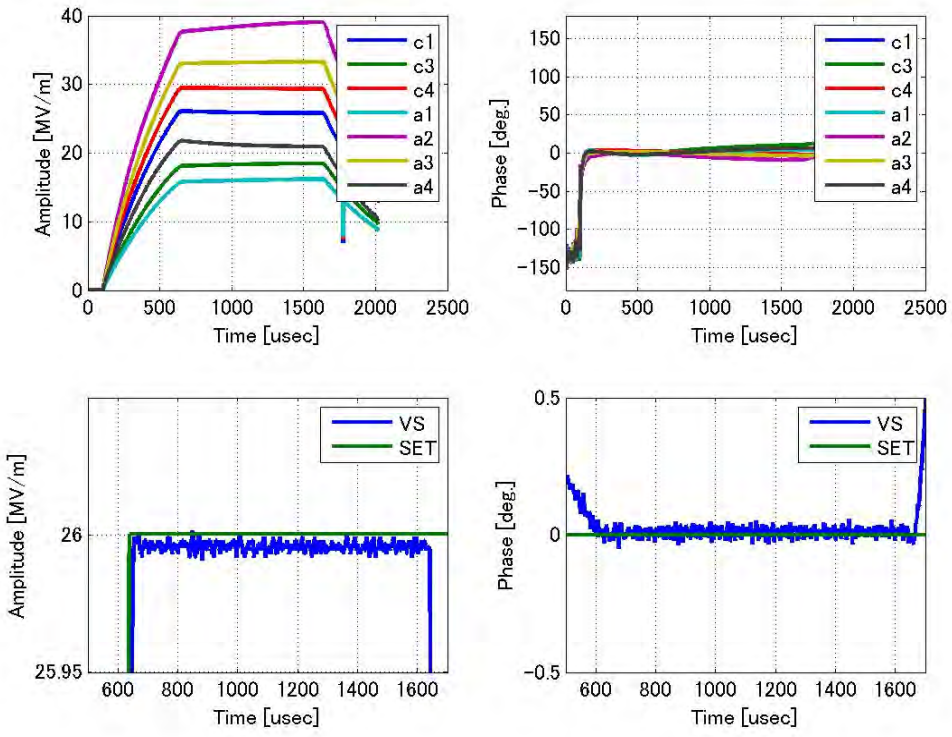

Figure 12-1: Vector-sum (VS) operation. The gradient and vector-sum gradient of each cavity (left) and the phase and vector-sum phase of each cavity (right).

12.2 Detuning Measurements during Long Duration Operating Tests

The cavities that were controlled by vector-sum feedback control were operated with an average gradient of 25 MV/m for 6000 s, and the detuning variation of each cavity during the flat part of the RF pulses is shown in Figure 12-2. An abrupt change in the detuning (2800 s) occurred in some cavities. The changes in detuning agree well with the changes in He pressure in the cryomodule. The high gradient cavities (approximately 38 MV/m in A-2 and 32 MV/m in A-3) show smaller detuning variations, and the response of the change in cavity detuning depends on the cavity structure rather than the operational gradient.

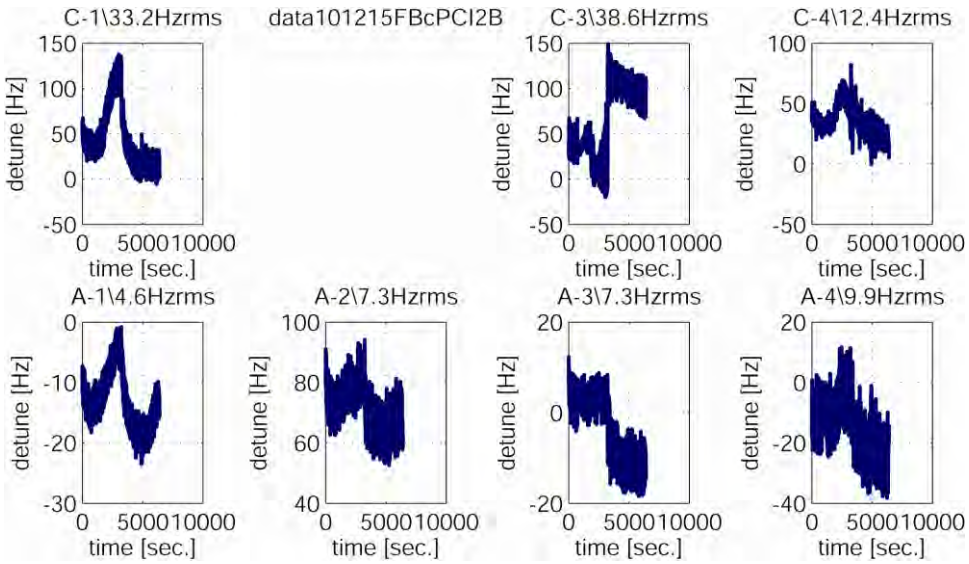

Figure 12-2: Detuning fluctuations of each cavity during 6000 s operation.

12.3 Quench Phenomenon

The digital LLRF system, as mentioned in Section 10-1, can store the RF waveforms of the last 150 pulses. These data can be used to examine the interesting phenomenon of quench during vector-sum operation. Figure 12-3 shows the cavity detuning and gradient of each cavity during a typical quench event. The red line corresponds to the pulse during which quench occurred, and the blue lines correspond to the pulses prior to the quench. The upper eight plots show the detuning of each cavity and the bottom eight plots show the cavity gradient during RF operation. An abrupt detuning change (approximately +100 Hz) occurred in C-4 and the gradient became smaller compared with the previous pulse. As a result, the gradient of the other cavities increased so that the vector-sum gradient remained constant. When the gradient of C-1 increased by about 3%, the gradient of C-1 decreased and the detuning changed -100 Hz at the end of the flat-top region of the RF pulse in Figure 12-3. This means that the gradient of C-1 exceeded the quench limit. The margin between the operational gradient and the quench limit should therefore be carefully considered.

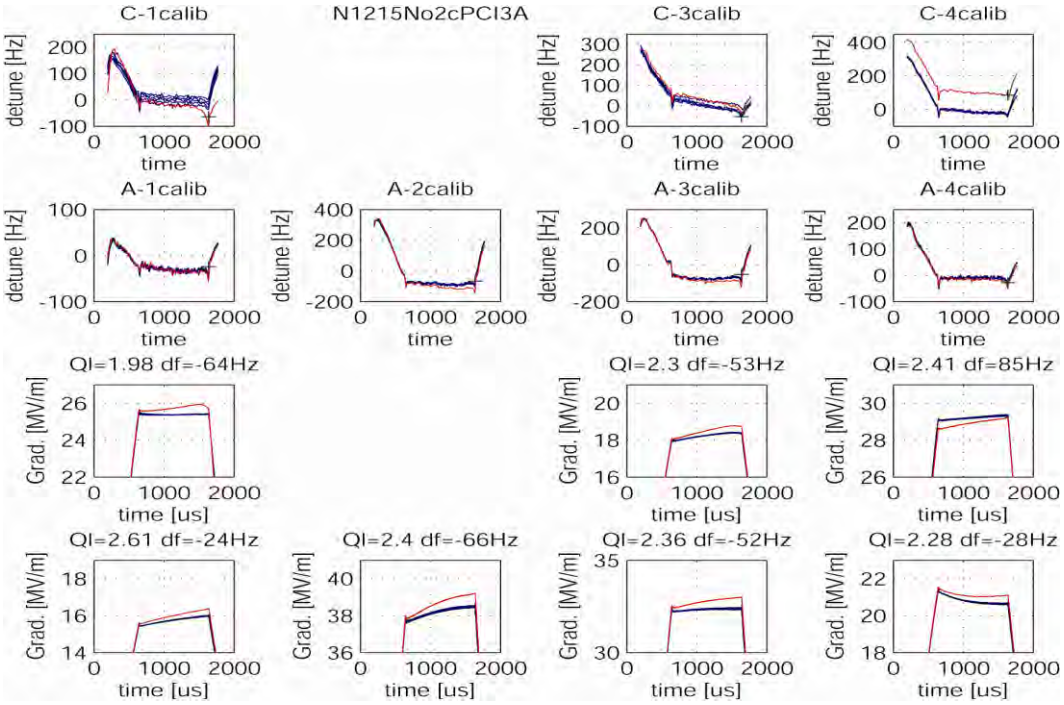

Figure 12-3: Cavity detuning (upper eight panels) and amplitude (bottom eight panels) for each cavity. The red line shows the quench pulse, and the blue lines show the pulses prior to quench.

12.1 Simultaneous Operation of Four Cavities

The simultaneous operation of four cavities at an average gradient of 26.9 MV/m for Cryomodule-A and of 20.0 MV/m for Cryomodule-C was carried out during the dynamic loss measurements. During this operation of about 35 min, the refrigerator system, LLRF feedback system, and piezo drive (feed-forward) worked stably.

Figure 12-1 shows the behavior of Q_L and the detuning frequency during the dynamic loss measurements for each cryomodule. Figure 12-2 shows the distributions of Q_L and the detuning frequencies for each cryomodule. The superimposed RF pulses at the full width of the pulse (the flat-top region of the blue trace) for two different periods (from the 200^{th} to the 450^{th} of the pulse and from the 1200^{th} to the 1600^{th} of the pulse) are shown for MHI-06 in Figure 12-3. Figure 12-4 shows data for various parameters measured during the dynamic loss measurements.

From Figure 12-1, it is clear that some changes occurred at the beginning of the dynamic loss measurements for both the cryomodules. In particular, there was a remarkable change in the detuning frequency, typically about 60 Hz, due to the effect of drift, as shown in Figure 12-2. On the other hand, the change in the gradient at the flat-top was 0.7 MV/m during #200-450 of the pulse, as shown in Figure 12-3. However, the helium pressure was stable during the dynamic loss measurements of both the cryomodules, as shown in Figure 12-4. This means that changes in the gradient and the detuning frequency are independent of those in the helium pressure, and another mechanism is likely to be responsible for these changes.

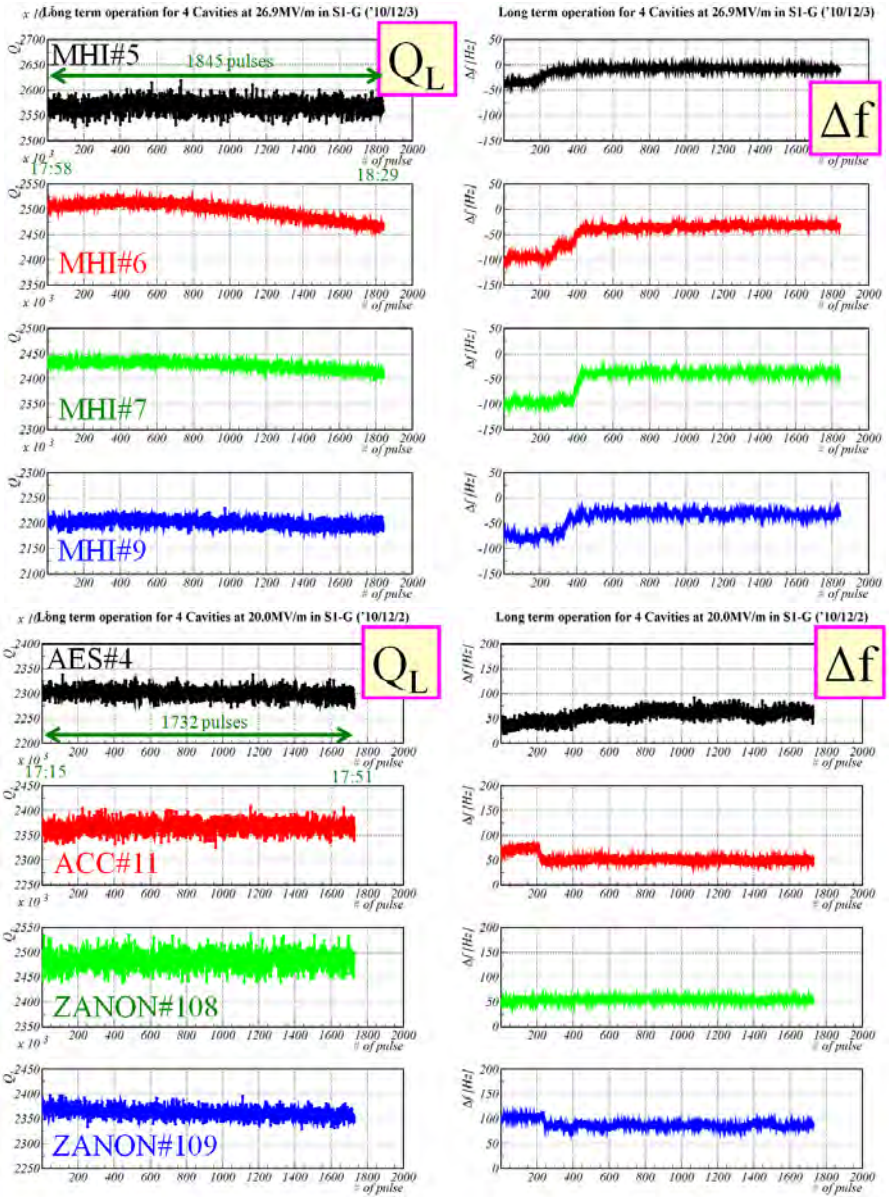

Figure 12-1: The behavior of Q_L and the detuning frequency during the dynamic loss measurements for each cryomodule.

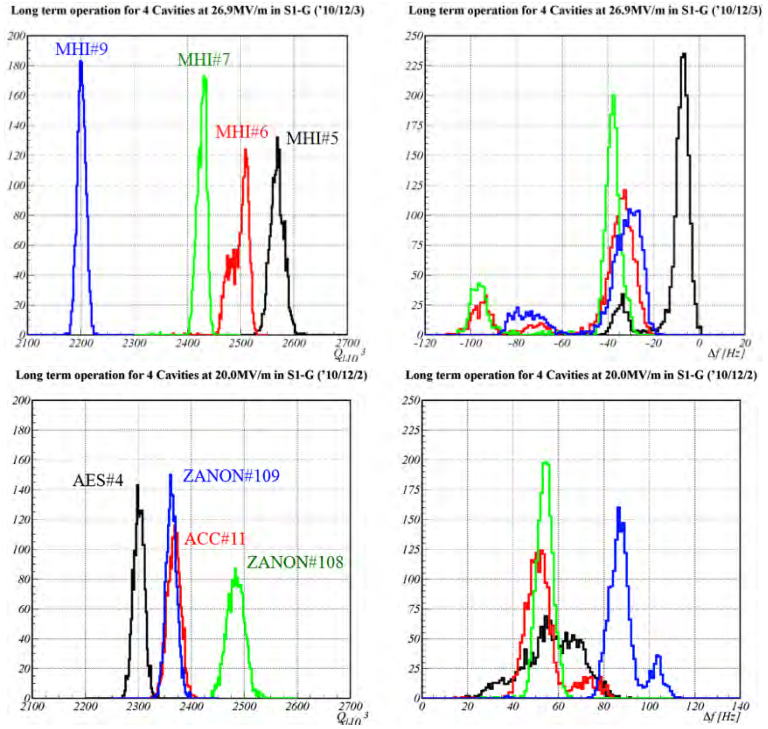

Figure 12-2: The distributions of Q_L and the detuning frequency during the dynamic loss measurements for each cryomodule.

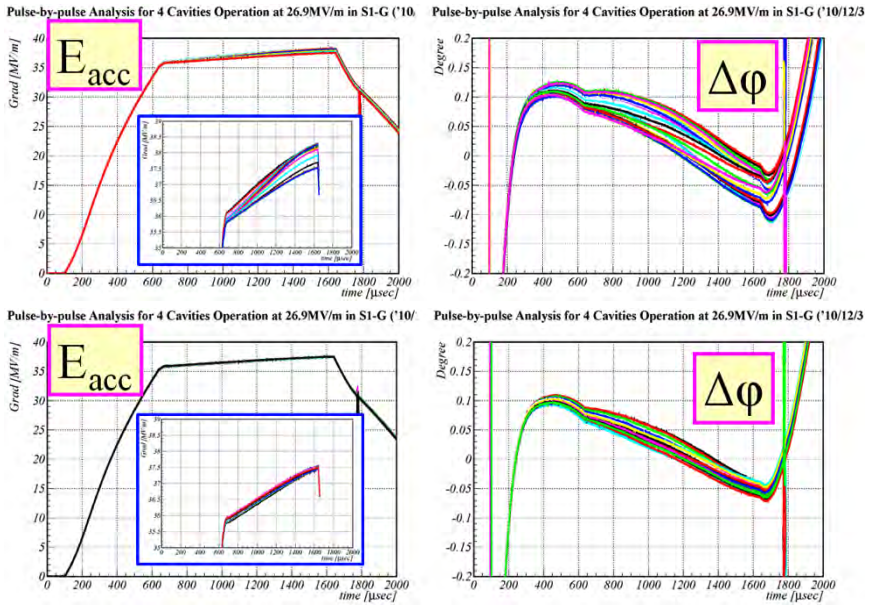

Figure 12-3: The superimposed RF pulses at the flat-top for two periods (from the 200th to the 450th and from the 1200th to the 1600th of the pulse) during the dynamic loss measurement.

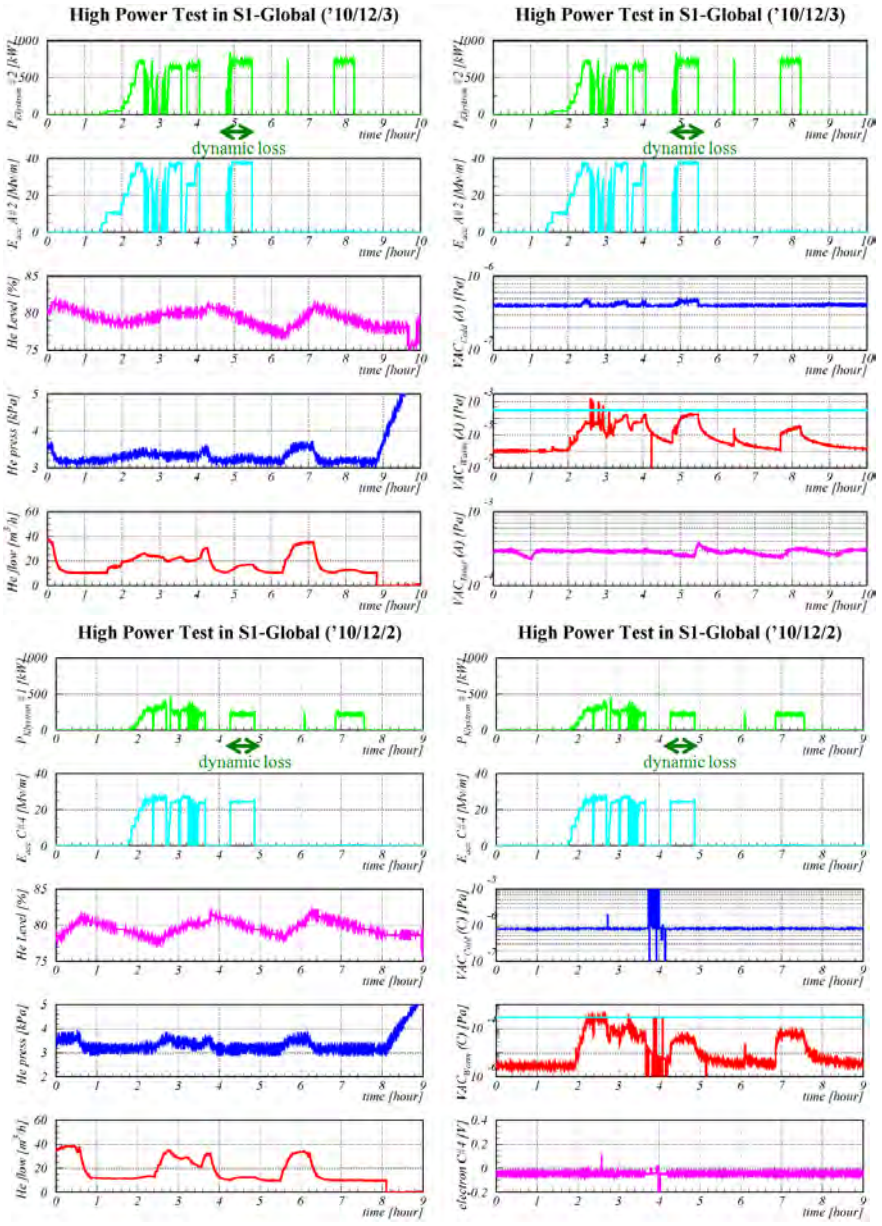

Figure 12-4: The behavior of the helium level, helium pressure, helium flow, and vacuum during the dynamic loss measurements for each cryomodule. Dynamic loss was measured for Cryomodule-A (Dec. 2) and Cryomodule-C (Dec. 3).

12.2 Simultaneous Operation of Seven Cavities

The simultaneous operation of seven cavities at an average gradient of 25.0 MV/m was carried out at the end of the second cold test. TB9ACC011 was excluded from this exercise due to the problem with its tuner, which was discussed earlier. During this operation, which lasted about 2 h, the refrigerator system, LLRF feedback system, and piezo drive (feed-forward) worked stably. Figure 12-5 shows the behavior of Q_L and the detuning frequency for the seven

cavities. Figure 12-6 shows the distributions of Q_L and the detuning frequencies. Because TB9AES004 and TB9ACC011 showed a large change in the detuning frequency, the distribution in Figure 12-6 is wider. Figure 12-7 shows the flat-top of the RF pulses for three periods superimposed over one another. Around pulse No. 3000, the detuning frequency changed noticeably for all cavities. In particular, the detuning frequency and Q_L for TB9ACC011 changed dramatically. Figure 12-8 shows the trends in the values of parameters recorded by various monitors for RF, helium, and vacuum. From these figures, it is clear that the helium pressure and flow gradually increased from the beginning to the middle of the operating time. A correlation seems to exist between the helium pressure and the changes in the detuning frequency for TB9AES004 and Z109. The detuning frequency of the MHI cavities also changed slightly.

A decrease in Q_L was observed for every cavity, and the difference between the initial and end value for MHI-06 and MHI-07 was large, at -3.9% and -3.5%, respectively. These cavities operated at 38 MV/m and 33 MV/m, and more input power was required for the power coupler. The drop in the Q_L value may be due to the heating of the inner conductor of the power coupler. The increase in the vacuum level of the inner conductor, as shown in Figure 12-8, suggests that heating occurs during the cavity operation.

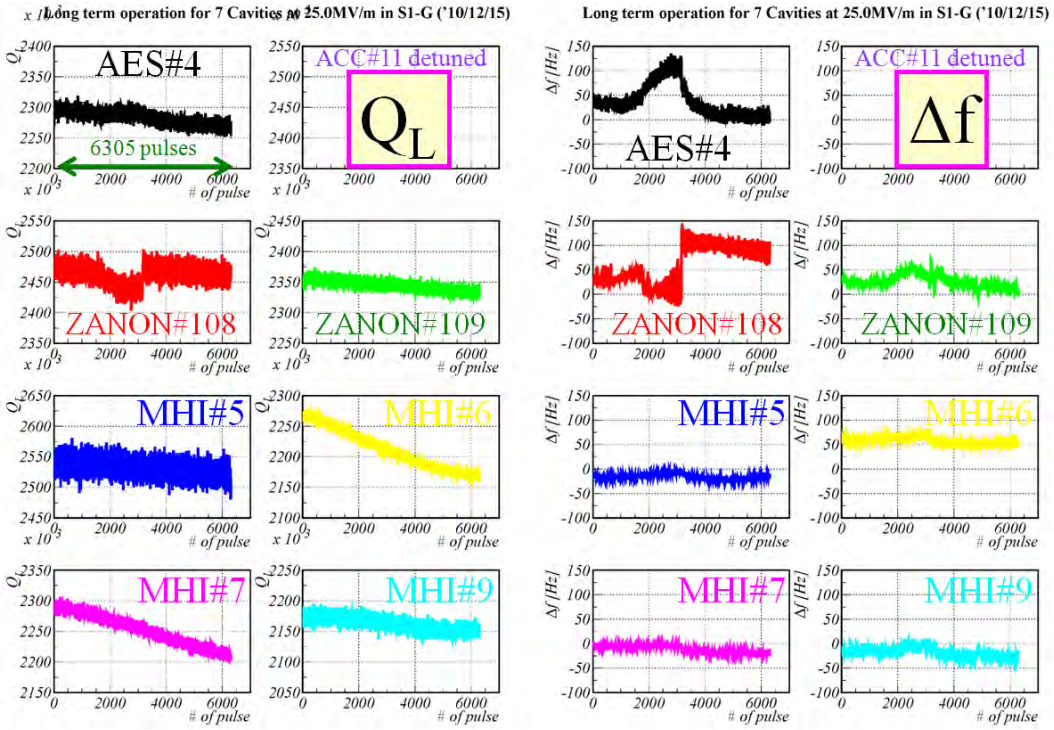

Figure 12-5: The behavior of Q_L and the detuning frequency for seven cavities during simultaneous, long-term operation.

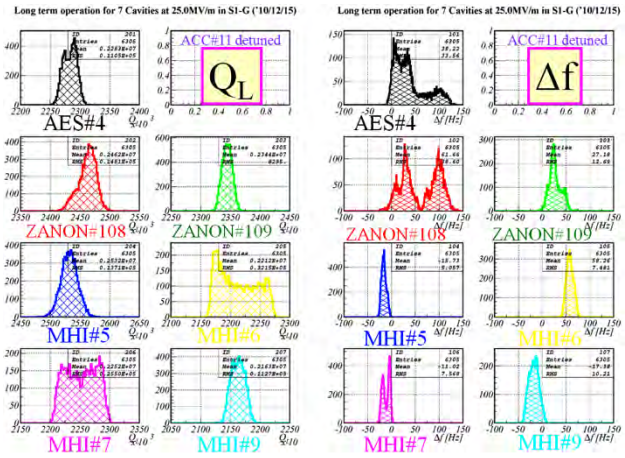

Figure 12-6: Distributions of Q_L and the detuning frequency for seven cavities during simultaneous, long-term operation.

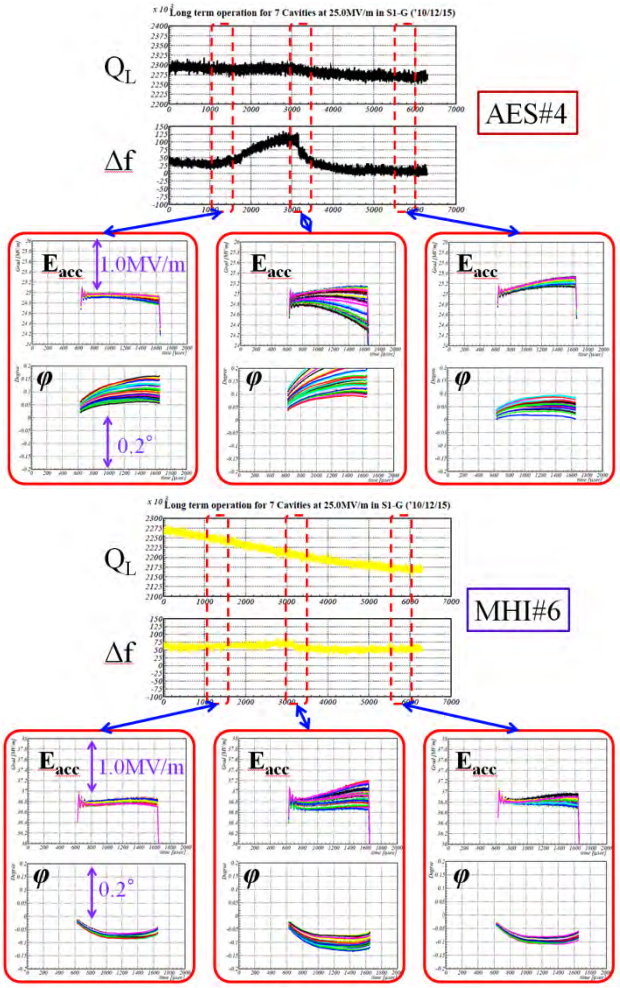

Figure 12-7: Superimposed RF pulses at the flat-top for three periods during long-term operation.

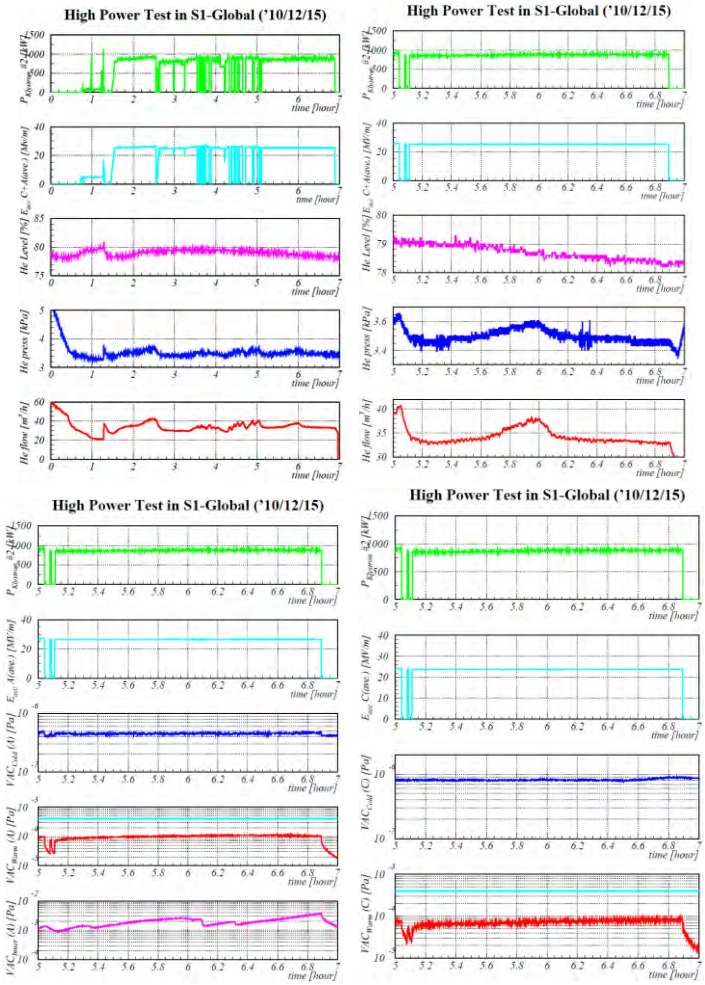

Figure 12-8: The helium level, helium pressure, helium flow, and vacuum pressure during the long-term operation (17:00-19:00): 12:00-19:00 (top-left) and 17:00-19:00 (others). The vacuum level at three locations for Cryomodule-A (left) and two locations for Cryomodule-C (right) are shown in the bottom figures.

12.3 Dynamic Loss Measurement

The dynamic loss measurement was carried out by members from FNAL and KEK in three cavity configurations (i.e., a single cavity, a string of four cavities, and a string of seven cavities) for the tuned and detuned conditions of these three configurations. [12-13]. The heat loss was estimated from the helium flow rate. While this was carried out, the liquid helium supply was temporarily stopped. The results, including the calculated values, are shown in Figure 12-9. It is clear that the STF-2 coupler suffers more heat loss, according to the results of the four detuned cavities. There was a difference of almost nine-fold between them.

It is conceivable that the Q_0 values below 10^{10} were caused by field emission. This is also clear from the results of the three radiation monitors attached near the cryomodule, which typically measured values that were above several 10 mSv/h at the maximum gradient.

Summary of dynamic loss measurements

	C-4 Z109	C-1 AES004	A-3 MHI07	A-2 MHI06	A-2 MHI06	4 C Cavities	4 A Cavities	4 C Cavities	4 A Cavities	7 Cavities	7 Cavities
Date	Nov. 17	Nov. 19	Nov. 23	Nov. 24	Nov. 25	Nov. 26	Nov. 30	Dec. 2	Dec. 3	Dec. 9	Dec. 10
Gradient [MV/m]	28	25.2	32.3	38	32	32 Detune	32 Detune	20 .0 Average	26.9 Average	25.4 Average	20.4 Average
Q_D, W	0.84	1.4	2.8	4.8	2.6			2.7	6.9	9.6	4.8
$Q_{D\text{-}det}$, W	0.09	0.18	0.7	1.8	1.2	0.5	4.6	0.2	2.5	2.6	1.6
$Q_{D\text{-}cav}$, W	0.8	1.3	2.0	2.9	1.3			2.5	4.4	7.0	3.2
Q_0	8.8E9	4.3E9	4.3E9	4.2E9	6.5E9						
								C1=22.2 C2=18.9 C3=14.9 C4=24.3	A1=15.8 A2=37.6 A3=32.9 A4=21.4	C1=25.2 C2=NA C3=17.6 C4=28.8 A1=15.3 A2=37.4 A3=32.4 A4=20.9	C1=20.1 C2=NA C3=14.1 C4=23.0 A1=12.3 A2=30.4 A3=26.0 A4=16.7

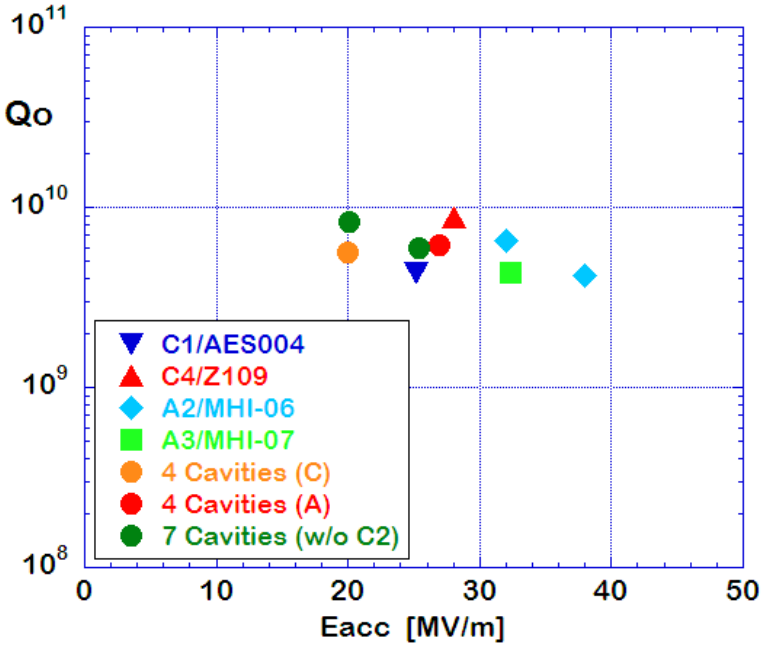

Figure 12-9: Results of the dynamic loss measurements. These measurements were recorded on 26 Nov and 30 Nov and were performed using the detuned cavities. All measured Q_0 values were below 10^{10}.

13 DRFS Operation

13.1 Introduction

During the final stage of the S1-Global experiment, a demonstration exercise of the distributed RF System (DRFS, [13-1]) was carried out for the pulsed operation of the cavities. The DRFS is a candidate scheme for producing and delivering RF power to the cavities in the single main linac tunnel design of the ILC. The version of the DRFS, considered during late 2011 (Figure 13-1), was to have thirteen 800 kW modulating-anode (MA) klystrons that would be driven by a common MA modulator and a common DC power supply. Each of the MA klystrons provides RF power to two superconducting cavities. Thus, one MA modulator is sufficient for twenty-six cavities, which is an equivalent beam accelerating capability to that of one RDR RF unit. All the components required for producing RF power are placed inside the underground tunnel.

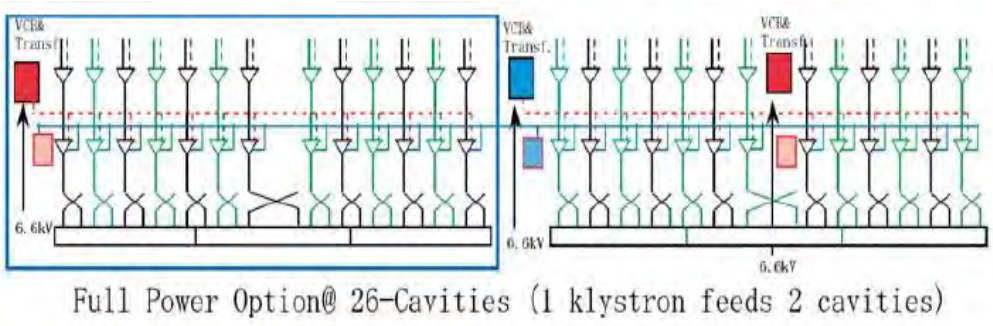

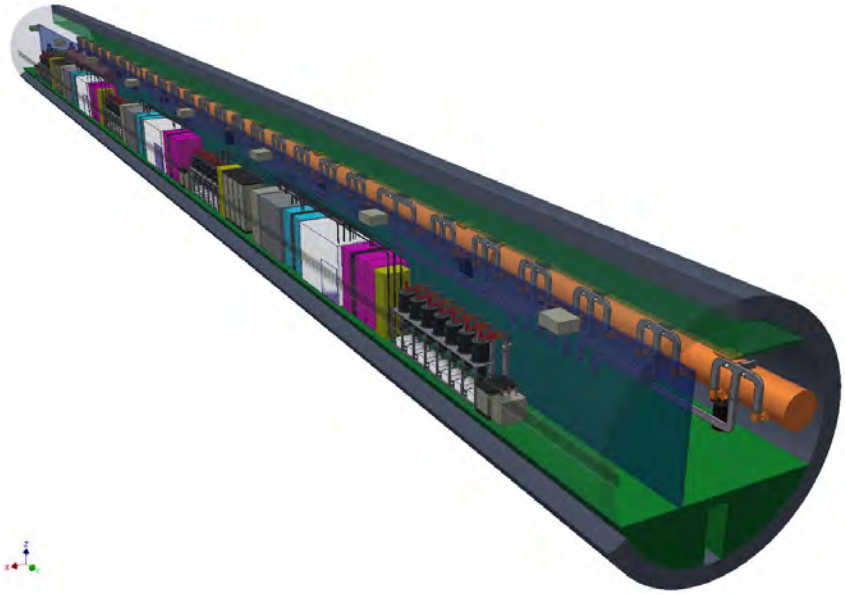

Figure 13-1: Top: Conceptual layout of the two RDR units configured by DRFS in the ILC main linac tunnel. Bottom: 3D CAD view of the DRFS that is implemented in the ILC main linac tunnel.

In the S1-Global, two MA klystrons (TOSHIBA E37501) were installed in the STF tunnel and connected to a nearby MA modulator. Each klystron provided RF power to two superconducting cavities via a circulator-less power distribution system (see section 9.3). The arrangement of multiple klystrons with a common MA modulator and DC power supply corresponds to one DRFS unit.

The ILC implementation of DRFS will involve more than 7000 RF units. In a system with such a large scale, careful consideration must be given to the simplicity of the hardware and the cost-effectiveness of the production and installation of components. Removing the circulators from the RF distribution system offers a substantial benefit in this regard. To establish the feasibility of this approach, the DRFS was operated in S1-Global with a circulator-less power distribution system.

13.2 Low-level RF System of DRFS at S1-Global

13.2.1 Digital Feedback Control Board

All the low-level RF (LLRF) systems, including the digital feedback (FB) system, were placed near the RF source in the tunnel. Digital FB control was performed by using a field-programmable gate array (FPGA) board with the μTCA standard. This board was the same as the one developed for the compact-ERL at KEK [13-2]. The digital FB boards, which were based on the advanced mezzanine card, were installed in a shelf of the μTCA. The board consists of a base card with FPGA (Virtex5FXT) and daughter cards having four-channel 16-bit ADCs (LTC2208) and DACs (AD9783). The embedded Linux is installed in a PowerPC on the FPGA, and EPICS is installed to make the digital FB board an EPICS IOC. Two digital FB boards, named μTCA1 and μTCA2, were prepared to control the two RF sources.

13.2.2 LLRF System of DRFS

Figure 13-2 shows a diagram of the LLRF control system [13-3]. The cavity pick-up signals, with the operating frequency of 1300 MHz, are down-converted to an intermediate frequency (IF) of 10.156 (=1300/128) MHz. This IF signal is sampled with a clock signal of 40.625 (=1300/32) MHz using a 16-bit analogue to digital converter (ADC). The sampled data are reconstructed to I and Q components via digital signal processing. The process of feedback calculation is carried out at 81.25 (=1300/16) MHz inside the FPGA. The vector-sum calculation is performed after the amplitude and phase correction of the I and Q data. The I/Q data are then passed through a digital low-pass filter. This filter consists of an IIR filter that rejects the noise in the ADC-input and a pass-band filter of the TM010 mode (except for the π mode). After passing through the IIR filter, the FB calculation of proportional control is carried out and the feed-forward (FF) table is added to the I/Q components. The baseband signals of the I/Q components from the digital to analogue converters (DACs) are fed to the IQ modulator, and then, the modulated signal is fed to the klystron.

The FB loop delay of the LLRF system was estimated by scanning the loop delay that was added inside the digital FB board. The obtained FB loop delay was 1.62 μs for μTCA1 and 1.26

μs for μTCA2. The difference between the FB loop delay of μTCA1 and μTCA2 is broadly explained by the excess cable length, which was approximately 0.17 ?s, and excess group delay of BPF, which was approximately 0.156 ?s, present in μTCA1.

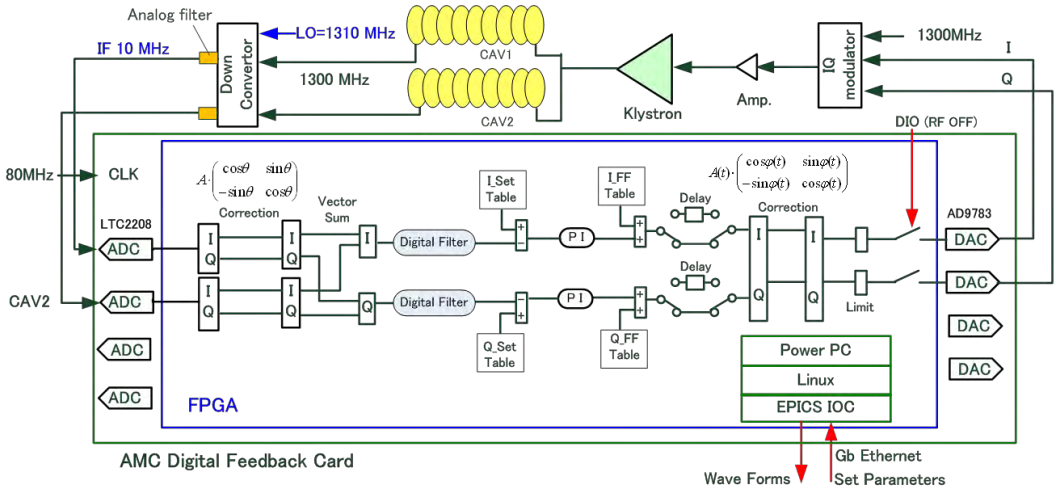

Figure 13-2: Schematic diagram of the LLRF control system in DRFS.

13.2.3 Sag Compensation

The modulating-anode voltage of the klystron has a large sag (~5%) during RF pulse operation because a bouncer circuit for pulse droop compensation was not installed. For a constant RF-input, the klystron output changed by approximately 10% in amplitude and 40° in phase for an RF pulse-width of 1.6 ms. This phase rotation is excessively large for compensation by using only FB. Hence, amplitude and phase correction tables were prepared to compensate for the large sag before the DAC-output, as shown in Figure13-3.

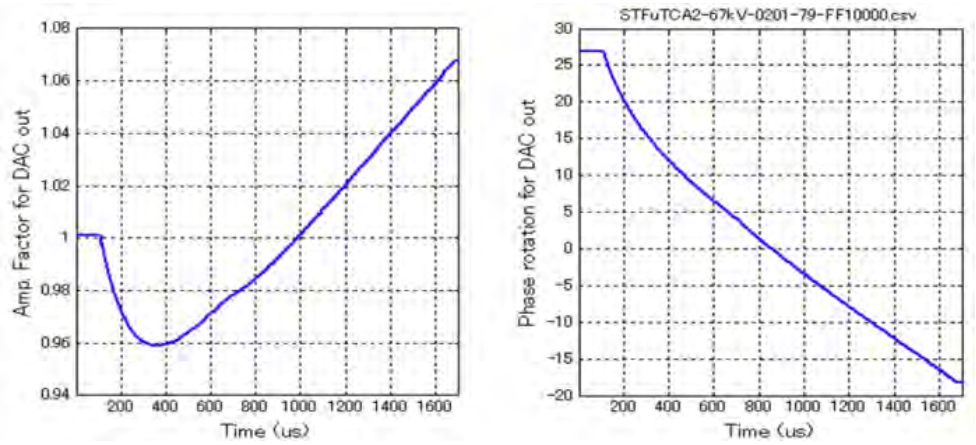

Figure 13-3: Correction factors for amplitude and phase for sag compensation.

13.3 Circulator-less Power Distribution System

13.3.1 Concept

The function of circulators in RF power distribution systems is to mitigate instabilities in the RF sources, which can be caused by reflected power, and to prevent the excitation of high-voltage standing-wave fields in the system. This is needed in order to protect the ceramic windows of the klystrons. Circulators also help to reduce the crosstalk between cavities that is mediated by the reflected power. This crosstalk makes it difficult to measure the cavity parameters (such as Q_L and cavity detuning) needed for precise diagnosis [13-4].

To achieve RF operation with a circulator-less power distribution system in DRFS, two cavities that had the same parameters were selected and configured with a specific phase difference. This causes the magnitude of the reflected powers from the two cavities to be very similar, and they can be made to interfere destructively by selecting an appropriate phase difference. If this is not the case, part of the reflected power goes back to the klystron and can result in crosstalk between the cavities.

In order to demonstrate the successful operation of a circulator-less power distribution system for the DRFS during the S1-Global tests, feedback operation of the RF source and system diagnosis schemes were investigated.

13.3.2 Configuration of Circulator-less Power Distribution

Figure 13-4 shows a schematic diagram of the power distribution system used for demonstrating the DRFS in the S1-Global tests. The RF output power from the klystron is split equally between the two arms of the waveguide by a magic-tee. To cancel the power reflected to the RF source at the magic-tee, a straight, 80-mm long waveguide (equivalent to about 90° at the operating frequency of 1.3 GHz), is inserted within one arm. If the phase difference of the reflected powers is 180°, the combined reflected power will be dissipated through the water load.

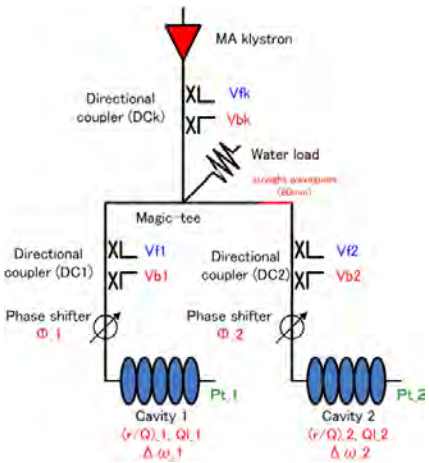

Figure 13-4: Schematic of RF system with circulator-less waveguide distribution system.

The power distribution system contains three directional couplers, as shown in Figure 13-4. The directional coupler that is located near the klystron (DCk) monitors the forward and backward signals of the klystron (Vfk and Vbk). The other two (DC1 and DC2) are placed in front of the cavities in order to measure the signals of the individual cavities (Vf1, Vb1, Vf2, and Vb2). In addition, two-phase shifters were installed in the two waveguide arms. These were used to control the cancellation of reflected power in order to study the influence of the reflected RF power.

13.3.3 Klystron Performance in Circulator-less Power Distribution

In order to estimate the influence of the reflected power on the performance of klystrons, both ends of the waveguide were shorted by end plates instead of being connected to cavities. The power reflected to the klystron was adjusted by changing the length of the phase shifter and the VSWR at the directional coupler, DCk, was measured.

The measured VSWR at DCk was less than 2.0 and was within 20° of the phase length from the position of minimum reflection, as shown in Figure 13-5. This was consistent with the estimates obtained from the simulation. This tolerance is sufficiently wide in comparison with the expected phase difference due to configuration errors (i.e., about 5°).

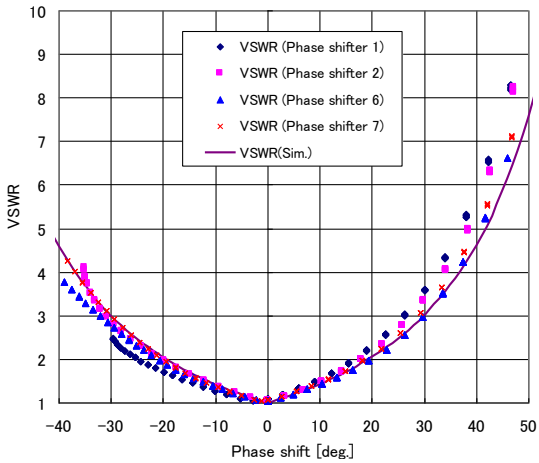

Figure 13-5: Change in VSWR caused by varying the phase length.

13.4 Relation between VSWR and Cavity Detuning

Figure 13-6 shows the correlation between the VSWR and differences in cavity detuning during the flat-top of the pulse. The detuning of the cavity was calculated from the measured data using eq. (1) in Section 10.4. The purple line in Figure 13-5 indicates the simulated VSWR, which includes the cavity detuning difference and agrees well with the VSWR observed at DCk. From this agreement, it is concluded that the calculation of the cavity detuning based on eq. (1) in Section 10.4 is still appropriate for the circulator-less power distribution system.

It was hoped that the VSWR would be suppressed to within a value of 2 during the operation. This could be achieved by controlling the detuning difference of both the cavities to be within

100 Hz in case the Q_L of each cavity is equal to 2.4×10^6. The ILC requires suppressing the cavity detuning at a pulse flat-top to within 50 Hz to guarantee the power margin of the RF source. If the cavity detuning were regulated in this manner, stable operation of the RF system would be achieved.

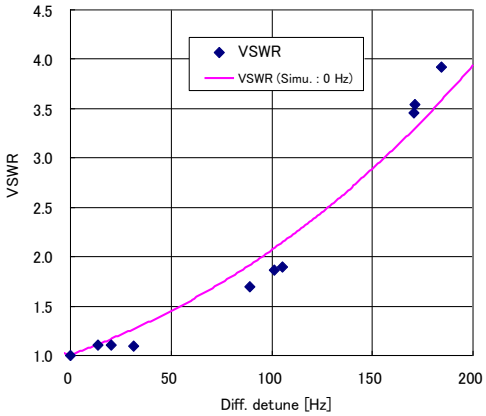

Figure 13-6: VSWR vs. the difference in the cavity detuning.

13.5 Field Stability under Feedback Operation

Figure 13-7 shows results of the vector-sum feedback operation at an accelerating field of 16 MV/m with a proportional gain of 145. In order to evaluate the range of detunings corresponding to stable feedback operation, the cavity detuning was changed by the piezo tuner under feedback operation.

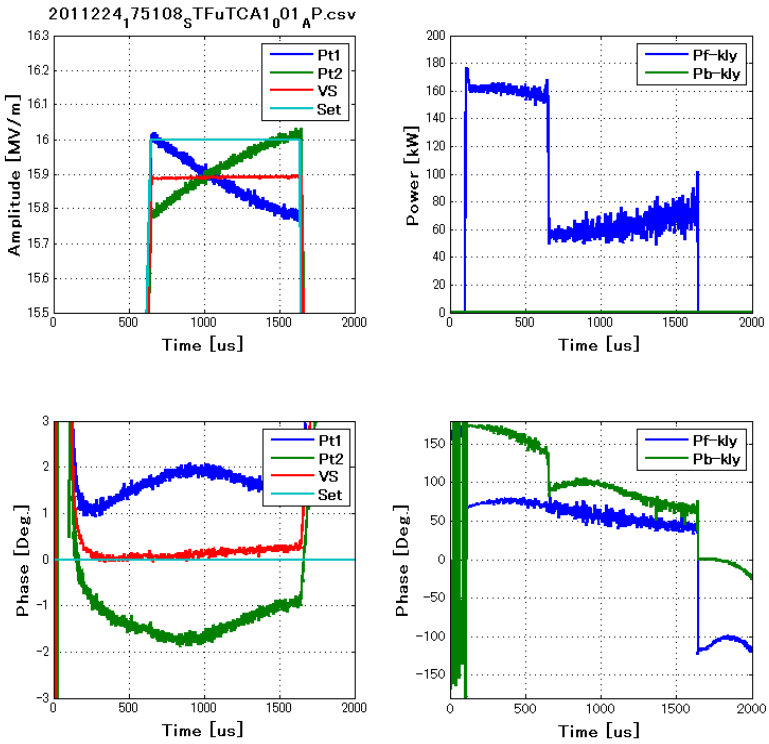

Figure 13-7: Amplitude (top left) and phase (bottom left) of each cavity, and the vector sum, the klystron output power (top right), and the reflected power and its phase (bottom right).

The correlation between the VSWR at the flat-top of the pulse and the detuning difference of both the cavities is shown in Figure 13-8. As the detuning difference increased, the VSWR at the flat-top deteriorated; however, it was confirmed that the feedback loop maintained the detuning difference to within 200 Hz.

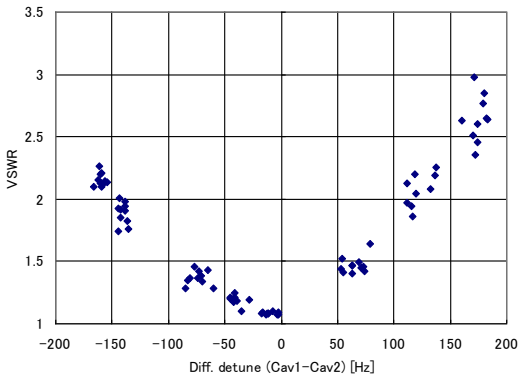

Figure 13-8: Correlation between the VSWR and the difference in cavity detunings under feedback operation.

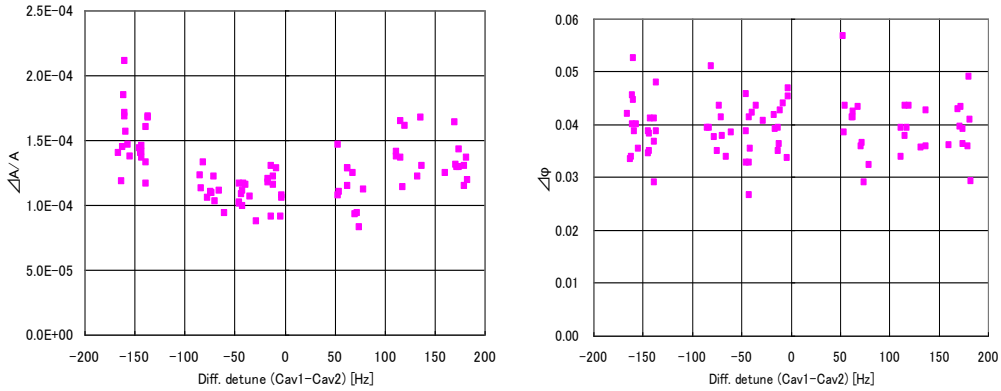

Figure 13-9: Correlation between the detuning difference of both the cavities and the stability of the amplitude (top) and phase (bottom) under feedback operation.

Figure 13-9 shows the correlation between the stabilities of the amplitude and phase of the accelerating field at the flat-top and the detuning difference of both the cavities. An amplitude stability of 1.3×10^{-4} (RMS) and a phase stability of 0.04° (RMS) were achieved while operating with feedback even when the detuning difference of both the cavities was greater than 200 Hz.

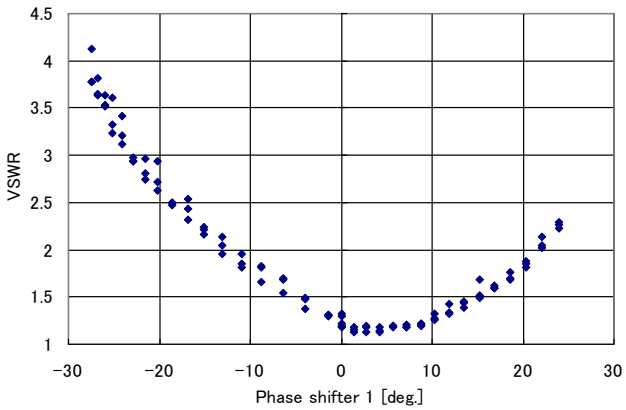

Figure 13-10: Correlation between the VSWR and the difference of phase length under feedback operation.

The effect of the phase length difference between both the cavities was also estimated by changing the phase length using the phase shifter. The measured correlation between the phase length difference and the VSWR is shown in Figure 13-10. During this measurement, the feedback loop was closed. The amplitude and phase stability was estimated and an amplitude stability of 1.3×10^{-4} (RMS) and a phase stability 0.04° (RMS) were verified with the feedback operation, as shown in Figure 13-11.

The measured stabilities satisfy the ILC requirements of variations of less than 0.07% in amplitude and 0.24° in phase.

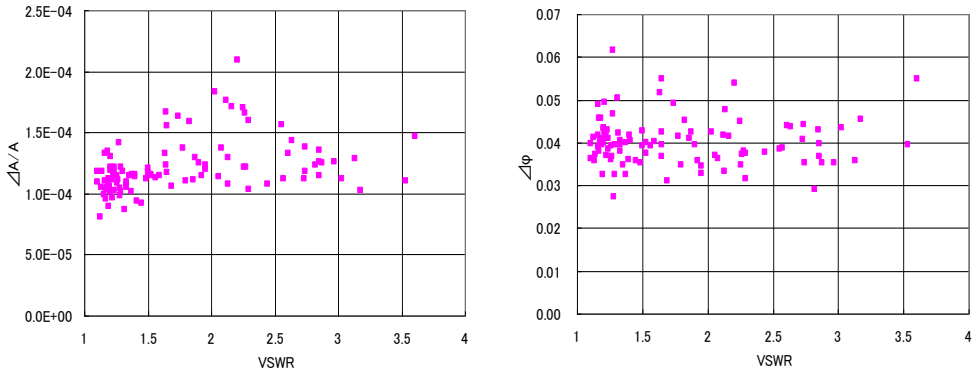

Figure 13-11: Correlation between the phase length difference and the stability of amplitude (top) and phase (bottom) under feedback operation.

14 Alignment

The alignment of the cavities in the cryomodules of S1-Global was set during the assembly of the cold mass and cryomodule, with contractions during cool-down to operating temperature accounted for in the design such that the cavities would be in the desired position after being cooled down. The support structures for the cavities in each cryomodule are the same as shown in Figure 14-1. The gas return pipe (GRP) in each cryomodule is suspended from the vacuum vessel by two support posts with the upstream support post fixed while the downstream post is allowed to slide in order to accommodate the thermal contraction of the GRP. Below the GRP, each of the four cavities is suspended through two support hangers. The longitudinal position of each cavity is fixed by a connection of the helium vessel to an Invar rod; the support hangers are rolling connections that allow for motion of the cavities during cool-down. The cavity position displacements during cool-down and in the cooled state at the operating temperature of 2 K are major concerns for the accelerator alignment.

From the earliest stages of cryomodule development at STF, wire position monitors (WPM) have been used in attempts to measure the displacement of the GRP and the cavities during cool-down; however, reliable data has not been obtained. In 2009, comparative measurements of the GRP movement in STF-cryomodule-B were performed using three types of methods, i.e., laser displacement sensors (LDS), optical telescopes, and WPM. The agreement between the GRP displacement obtained using the LDS and optical telescope was confirmed; however, the WPM still produced unstable results.

In this S1-Global experiment (2010 and 2011), we have upgraded the WPM electronics from a CW RF drive method to a pulsed RF drive and upgraded the sample-hold detection electronics with 100 Hz slow filtering in order to avoid interference of drive RF leakage into the detection circuit. The measured GRP and cavity displacements obtained by using LDS and WPM are discussed in the following section.

14.1 Installed Instrumentation

After the experience of assembling STF cryomodule B, a more extensive instrumentation plan was created to monitor the GRP displacement in both the modules of S1-Global during cool-down and when the system is in equilibrium at 2 K. The position of the GRP of module A was measured using both LDS and WPM. In addition, the cavity displacements were also monitored directly using a WPM system in module A. In module C, the position of the GRP was measured by WPM as in module A, although no LDS system was installed, and the cavities in module-C were not monitored in order to save engineering effort and the preparation time for the jacket modifications that would be required to be made to the DESY and FNAL cavities. GRP1 to GRP5 are the names of the WPM pickups that were attached in the GRP of module-A, while LDS1 through LDS4 are the name of the LDS sensors attached in the top of the module-A (Figure 14-1). CAV-1U, CAV-1D, and so on, are the names of the WPM pickups that were attached at the upstream (U) and downstream (D) ends of each cavity of module-A (see Figure 14-1).

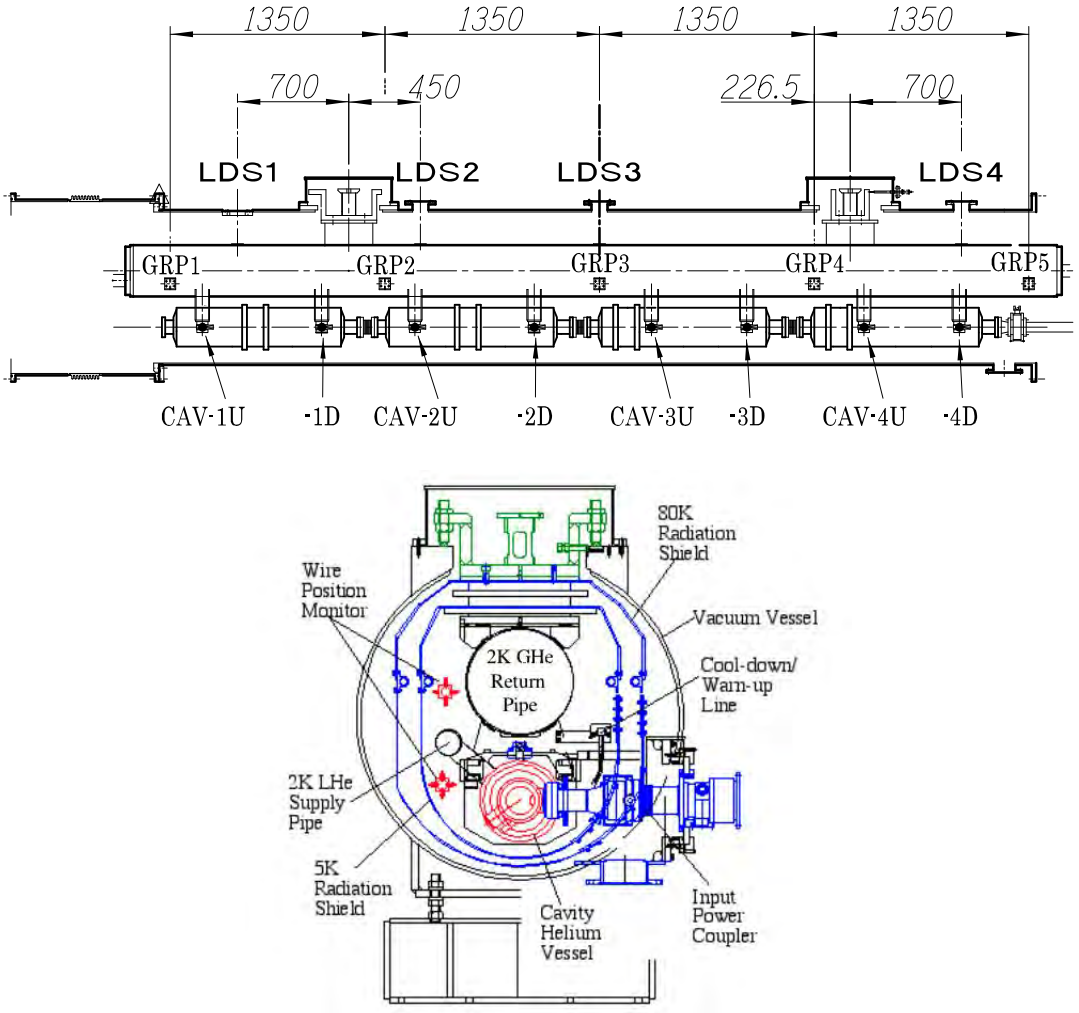

Figure 14-1: Displacement monitors installed in Module-A. LDS1-4 are the laser displacement sensors, GRP1-5 are the wire position monitors on the GRP, and GRP-1-5 and CAV-1U -4D are the wire position monitors on the cavity jackets.

14.2 Laser Position Monitor

Four laser displacement sensors, i.e., LDS1, LDS2, LDS3, and LDS4, were installed on top of the module-A vacuum vessel (Figure 14-1). There are four glass windows that allow laser light to reach a mirror mounted on the GRP and to be reflected back to the sensor. Keyence LK-G sensors were used, as shown in Figure 14-2. The specifications are as follows:

measuring range: 400±100 mm

resolution: 2 μm

linearity: ± 0.05% of F.S.

laser spot diameter: approximately 290 μm

Figure 14-2: Laser displacement sensor.

14.3 Wire Position Monitor

Two stretched wires consisting of 70 µm diameter gold-plated tungsten were used in the S1-Global experiment: one was used to monitor the displacement of the GRP, and the other, to monitor the displacement of the module-A cavities. The wires were stretched along the 12-m distance through module-C and module-A. In module C, at the upstream end of each wire is an N-type feed-through connector for feeding the RF pulses into the wire. At the other end, the wires are electrically insulated with no resistor and an SUS weight of 500 g is suspended from the end to provide tension in the wire. Aluminum shield pipes are used for inter-connections between the WPMs, and thin SUS pipes are used for forming connections between the WPMs and endplates.

Each WPM pickup (Figure 14-3) consists of four strip-lines (SUS electrodes) and an aluminum body with SMA connectors, where one end is terminated by a 50 Ω resistor and the other is connected to the signal cable. The drive RF pulse is a burst sine-wave signal of 160 MHz with a 100 ns pulse width and +23 dB amplitude. The mV-level signals from the pickup electrodes were multiplexed and amplified by a log-amplifier and amplitude-detected, and then converted into a DC voltage by a sample/hold circuit. The detected DC voltages are routed into a 16 bit ADC and sent to the data-logging computer. The time interval of the WPM recording is around 10 s. The resolution of the system is on the order of 10 µm, and the error in position detection is estimated to be less than 5%. Figure 14-4 shows the position of the installed WPMs in the cross-sectional view of the cryomodule.

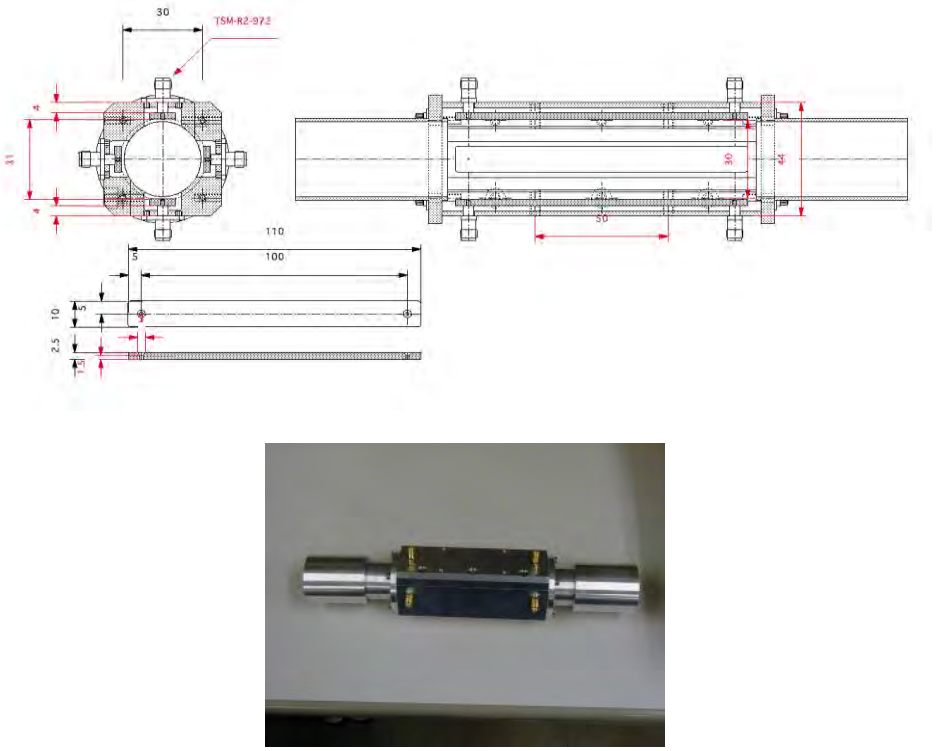

Figure 14-3: Drawings and photo of WPM pickup. Four strip-line electrodes with SMA connectors in both ends are installed in the aluminum body.

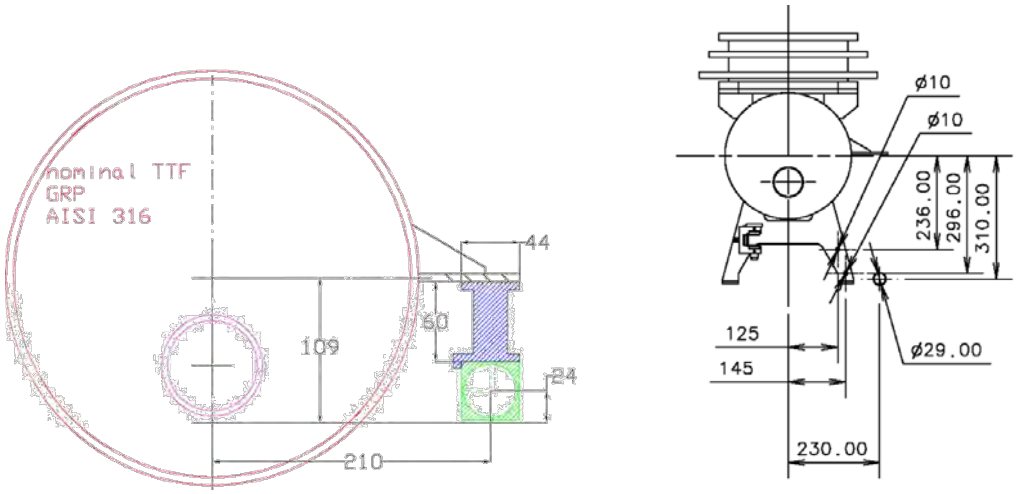

(a) GRP-WPM installation position (210 mm right and 109 mm down from the center of GRP)
(b) Cavity-WPM installation position (230 mm right and 310 mm down from the center of GRP)

Figure 14-4: Cryomodule cross-section showing WPM position.

14.4 Position Displacement Measurement for GRP and Cavities

Cooling down from room temperature to ~150 K was performed by using He gas (~80 K) at a mass flow rate of ~1.5 g/s. From 150 K to 2 K, the cool-down was completed using liquid He

with a mass flow rate of ~0.35 g/s. For the duration of the test, due to administrative limits, the STF cryogenic system was only operated between 8 AM and 7 PM, four days a week, and it was not operated overnight or on weekends (intermittent cooling). The representative displacement data presented here for the alignment discussion were collected from the period between 19 Jan, 2011 to 9 Mar, 2011. During this period, the WPM electronics were in the most stable and upgraded state. The temperature variation of the GRP and helium vessel over this period are shown in Figure 14-5 (a), which includes the cooling down and warming up periods at the beginning and the end, and includes, in total, four full weeks of daily operation and weekend warming up periods. All the measurements of the WPM in the GRP are shown in Figure 14-5 (b) and (c). They show shifts in the X position and Y position of the GRP during cool-down and during the 2 K state.

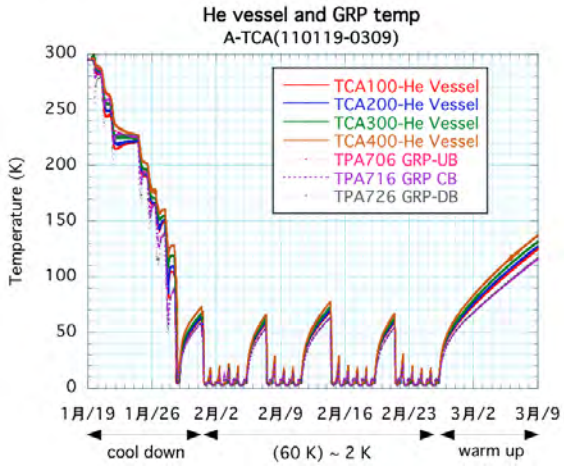

(a) Temperature change during the Jan. 2011 to Mar. 2011 experiment.

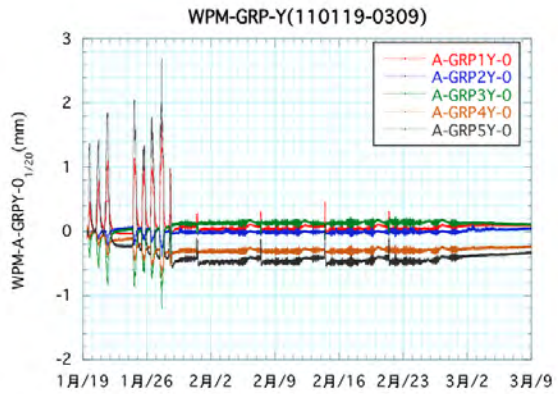

(b) Y position change of GRP as measured by WPM during the Jan. 2011 to Mar. 2011 experiment.

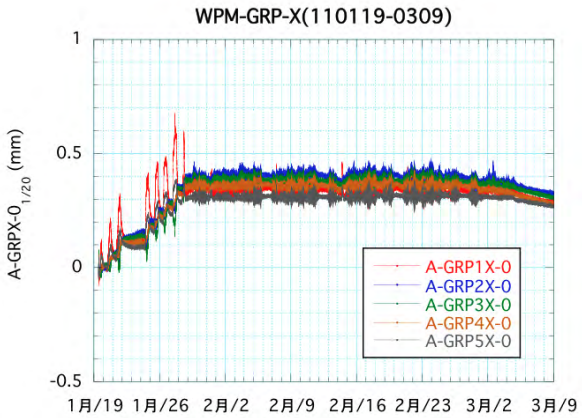

(c) X position change of GRP as measured by WPM during Jan. 2011 to Mar. 2011 experiment.

Figure 14-5: GRP-WPM signal overview during Jan. 2011 to Mar. 2011 experiment.

During cool-down, large displacements of the GRP in the Y direction (a maximum of 2.7 mm) were observed, as shown in Figure 14-6 (a), (b), (c), and (d). However, the measurements at 2 K, obtained from the WPM-GRP Y positions, were not consistent with the Y positions measured by the LDS, or with the estimated displacement (dY = - 0.22 mm). The displacements of the GRP in the Y direction at 2 K, as measured by the WPM, were split two groups as shown in Figure 14-6 (a). Upstream three WPM displaced to 0 to +0.2mm. Downstream two WPM displaced -0.3mm and -0.5mm. They were difficult to interpret. On the other hands, LDS showed -0.2 to -0.3mm displacement, consistent with estimation.

The behavior of the WPM-GRP X position during the entire period seems to be reasonable; however, the amount of displacement at 2 K, which was around +0.4 mm, is smaller than the estimated value (+0.62 mm), as shown in Figure 14-6 (b). The excursion behavior at cool-down of the WPM-GRP-1 X position is different from the behavior of the other WPM-GRP X positions.

The displacements in the Y direction at 2 K, which were measured by the WPM mounted on the cavities, can be separated into two groups, as shown in Figure 14-6 (c). The first group of displacement are around -0.5 mm, the other group are around -1 mm. The estimated value (-1.07 mm) is consistent with the results of the second group, but the result of the first group is not readily understood. The behavior of WPM-Cavity X positions as shown in Figure 14-6 (d) is roughly consistent with the estimated value, i.e., +0.75 mm. However, there are 0.4 mm variations in these measurements.

WPM-Cavity-2 UY and WPM-Cavity-4 UY were omitted because of unstable data, and WPM-Cavity-1 DY and WPM-Cavity-3 UX were interchanged due to a misconnection.

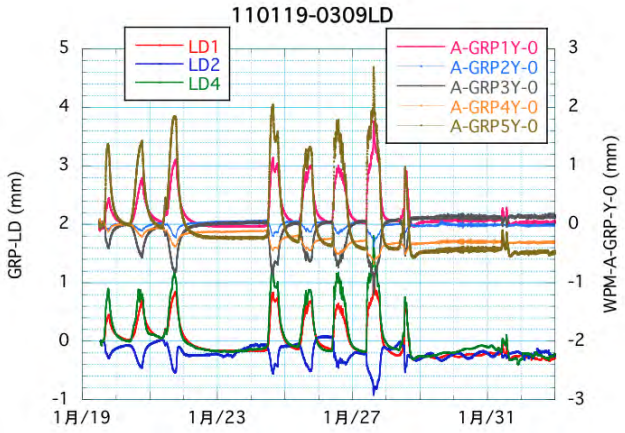

(a) Variation in GRP Y position during cool-down. LD1 to LD4 show measured Y variation by LDS. A-GRP1Y-0 to A-GRP5Y-0 show measured Y variation by WPM.

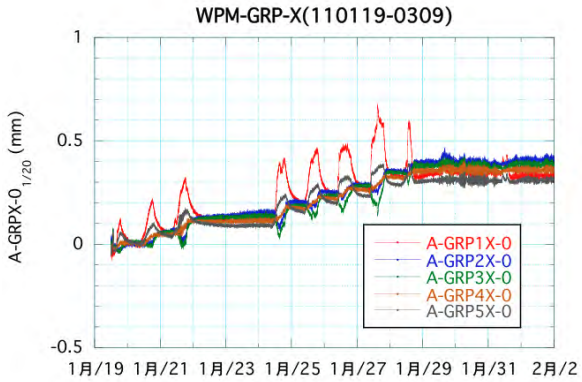

(b) Variation in GRP X position during cool-down. A-GRP1X-0 to A-GRP5X-0 show measured X variation by WPM.

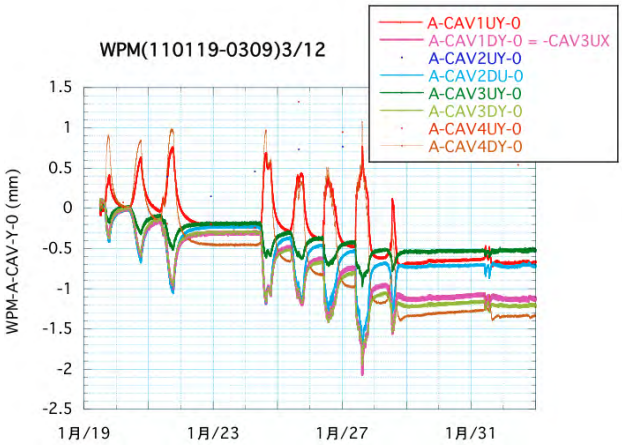

(c) Variation in cavity Y position during cool-down. A-CAV1UY-0 to A-CAV4DY-0 show measured Y variation by WPM.

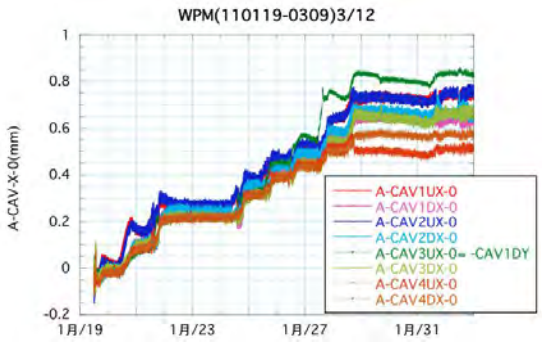

(d) Variation in cavity X position during cool-down. A-CAV1UX-0 to A-CAV4DX-0 show measured X variation by WPM.

Figure 14-6: Displacement measured by WPM and LDS during cool-down period. X axis shows month and day from 19 Jan to 2 Feb, for (a) to (d).

During the periods of 7 Feb to 11 Feb and 15 Feb to 19 Feb, module-A was kept at 2 K during the daytime. Figure 14-7 shows the WPM and LDS variations together with the change of the 2 K temperatures. The fluctuation widths of the LDS signals during these periods are about 0.2 mm; however, those of the WPM Y position installed at GRP are smaller than 0.1 mm. The fluctuation widths of the WPM Y position installed at cavity are also smaller than 0.1 mm. The reason for this difference between the LDS and WPM measured stabilities is not yet understood.

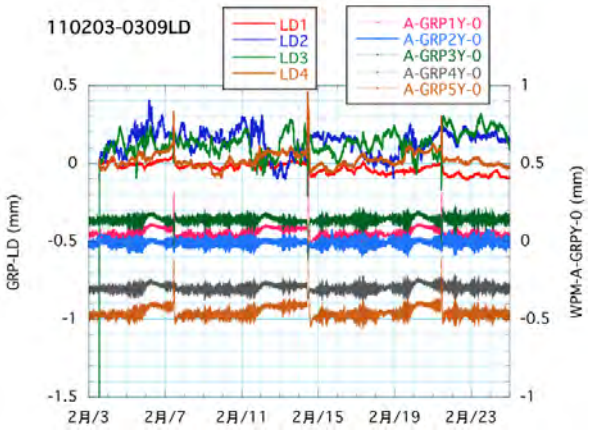

(a) Variation in GRP Y position during cooled state. LD1 to LD4 show measured Y variation by LDS. A-GRP1Y-0 to A-GRP5Y-0 show measured Y variation by WPM.

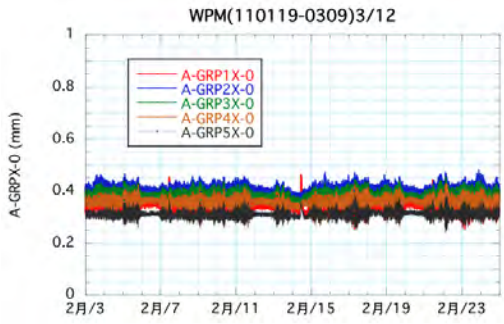

(b) Variation in GRP X position during cooled state. A-GRP1X-0 to A-GRP5X-0 show measured X variation by WPM.

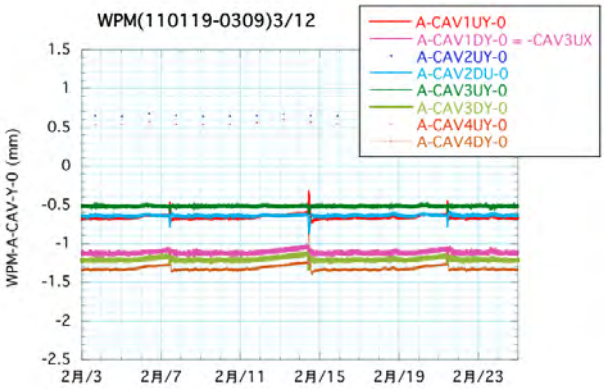

(c) Variation in cavity Y position during cooled state. A-CAV1UY-0 to A-CAV4DY-0 show measured Y variation by WPM.

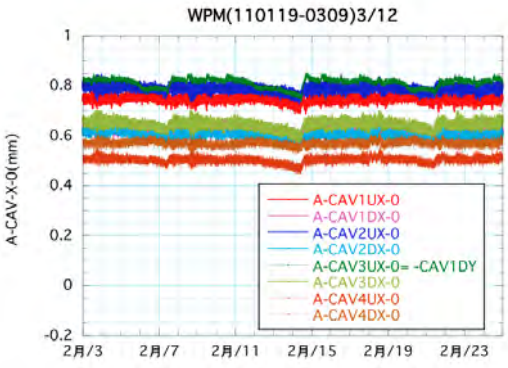

(d) Variation in cavity X position during cooled state. A-CAV1UX-0 to A-CAV4DX-0 show measured X variation by WPM.

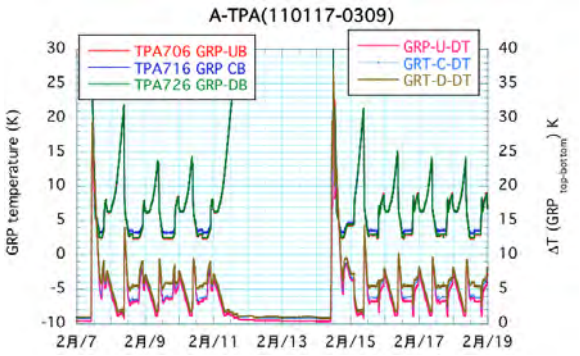

(e) Variation in GRP temperature during cooled state. Red, blue and green show GRP temperature from upstream, center and downstream of module. Pink, light blue and brown show temperature variation between top side and bottom side of GRPs. X axis shows month and day starting from 7 Feb to 19 Feb.

Figure 14-7: Displacement measured by WPM and LDS during cooled state. X axis shows month and day from 3 Feb to 23 Feb, for (a) to (d). Plot (e) shows temperature variation measurement of GRP.

14.5 Summary of LDS and WPM

(1) During the cooling down stage, rather large vertical displacements (max 2.7 mm) at the ends of the GRP were recorded by both the LDS and the WPM.

(2) The GRP displacement measured by LDS was consistent with estimated displacement. However, the GRP and cavity Y displacement measured by WPM were split to two groups and inconsistent with the estimation. The amount of GRP X displacement by WPM, which was around +0.4 mm, is smaller than the estimated value (+0.62 mm). The behavior of Cavity X displacement by WPM is roughly consistent with the estimated value (+0.75 mm). However, there are 0.4 mm variations between them.

(3) After the cavities were cooled to 2 K, the fluctuations in the GRP positions measured by WPM were less than 0.1 mm, while the fluctuations measured by the LDS were about 0.2 mm.

The reason for this discrepancy is not yet clear. However, it seems that the WPM pickup electrodes need to be modified to maintain stable operation during this type of large thermal excursion. We also found that some of the SMA connectors for the signal cables were unstable contact during the thermal excursion. These need to be upgraded in the next installation.

15 Summary

The S1-Global cryomodule experiment was planned in 2008, constructed in 2009, and performed in 2010 by an international collaboration formed by the GDE team. STF, at KEK, was the host facility for the experiment. The main goal of the experiment was to achieve the "S1" goal, that is, to operate at least one cryomodule with an average gradient of 31.5 MV/m, as required for the ILC. The gradient performance of the contributed cavities was averaged at 30.0 MV/m before installation, 27.7 MV/m for single cavity operation after installation, and 26.0 MV/m for seven cavities operating simultaneously. Another goal of the experiment was to implement the plug-compatibility concept by building one cryomodule from cavities and couplers brought together from each of the contributing laboratories. The half-sized cryomodule, i.e., module-C, was a demonstration of this, as it was built from an INFN cryostat, DESY cavities and couplers, and FNAL cavities and couplers. The connection of module-C to the KEK module-A demonstrated another aspect of plug-compatibility. The 3D CAD-based discussion in the design stage was an efficient means to realize plug-compatibility.

During the experiment, a 27% and 38% degradation of the cavity gradient was observed for TB9ACC011 and Z108, respectively. A coupler breakdown occurred for MHI-05 and the available gradient was limited to 16 MV/m. The tuner mechanics malfunctioned on the TB9ACC011 blade tuner and the MHI-09 slide-jack tuner installed at their cavity endplate. In both the cavities, we were unable to control the coarse frequency tuning, to ensure that the simultaneous operation of cavities, which is required in order to align the cavity frequency, was limited to seven, instead of eight, cavities. One of the two piezo elements in TB9ACC011 exhibited discharge problems, and it could not be used in the determination of the nominal voltage. The dynamic heat load of the STF-2 coupler measured by cavity-detuning was 4.6 W for four cavities, and for the TTF-III couplers the dynamic head load was 0.5 W.

The following list is the summary of the achievements and contributions of the teams involved in the S1-Global cryomodule test.

(1) Internationally collaborative design work by WebEx meeting and several GDE meetings lead by Norihito Ohuchi

(2) Clean-room cavity assembly/disassembly by the DESY-FNAL-KEK team lead by Tug Arkan

(3) Tuner/magnetic shield installation/dismount by the INFN-FNAL-KEK team lead by Carlo Pagani

(4) Coupler installation/dismount by the DESY-KEK team lead by Denis Kostin and Eiji Kako

(5) Cavity low power measurement by the INFN-FNAL-KEK team lead by Carlo Pagani

(6) Thermal performance measurement, using many temperature sensors, conducted by the FNAL-KEK team

(7) Successful high gradient operation of cryomodule cavities with (i) Lorentz force detuning control by piezo tuner, and (ii) precise digital LLRF control

(8) Successful demonstration of adaptive piezo control for Lorentz force detuning compensation by the FNAL team

(9) Successful operation of DRFS power scheme without a circulator by the KEK team

(10) Monitoring of the GRP and cavity movements, due to thermal contraction, using laser-sensors and wire-sensors, by the KEK team

Through the S1-Global tests, we have identified the following avenues for further study:

(1) Identify the cause of gradient degradation and then improve the cryomodule gradient performance.

(2) Identify the cause of blade-tuner and slide-jack-tuner mechanical problems and then improve the mechanical tuner reliability. (These failures are described in Chapter 11.2.)

(3) Identify the cause of the tuner piezo problems and then improve the piezo tuner reliability. (These failures are described in Chapter 11.2.)

(4) Identify the cause of the STF-2 coupler breakdown and then improve the coupler RF performance.

(5) Identify the cause of the STF-2 coupler heat load excess and then improve the coupler thermal performance.

The S1-Global program was a truly international cryomodule experiment performed through the effort of GDE members and the participating GDE laboratories. The program has demonstrated the development and assembly of a cryomodule, through an international collaboration, that performs close to the ILC specification. However, issues associated with the current cryomodule technologies that need to be solved were identified and will be addressed in future work.

16 Acknowledgement

The authors gratefully acknowledge the participating laboratory directors and collaborating personnel for their understanding and cooperation throughout this program. The continuous encouragement, appropriate advice, and strong support of the GDE director, Barry Balish, and the executive boards, including the project manager, are also acknowledged and greatly appreciated.

The program was realized and accomplished by a cooperative industry effort. The authors especially thank Zanon Inc. for the module-C production, Hitachi Co. for the module assemblies, and both the companies for their cooperation.

17 References

[2-1] http://ilcdoc.linearcollider.org/collection/GDE%20Organization

[8-1] N. Ohuchi, *et al*., "S1-Global collaborative efforts 8-cavity-cryomodule: 2 FNAL, 2 DESY, and 4 KEK," LINAC'10 Tsukuba, p. 31 (2010).
[8-2] E. Kako, *et al*., "S1-Global Module Tests at STF/KEK," in this conference, M00DA02.
[8-3] C. Pagani, *et al*., TESLA Report 2001-36.
[8-4] M. Dohlus, *et al*., "Tesla RF power coupler thermal calculations," LINAC 2004, Lubeck, p. 174 (2004).
[8-5] E. Kako, *et al*., "Advances and performance of input coupler at KEK," SRF'09, Berlin, p. 485 (2009).

[9-1] ILC Reference Design Report- Accelerator, 2007, http://www.linearcollider.org/cns/?pid=1000437
[9-2] SB2009 Proposal Document, Rel. 1.1, 2009, http://lcdev.kek.jp/SB2009/
[9-3] S. Fukuda, *et al*., "Status of RF Sources in Super-conducting RF Test Facility (STF) at KEK," PAC09, 4-8 May 2009, Vancouver, British Columbia, Canada, pp. 1032-1034 (2009).
[9-4] C. Nantista, *et al*., "An RF Waveguide Distribution System for the ILC Test Accelerator at NML," PAC'07, Albuquerque, New Mexico, USA, pp. 2442-2444 (2007).

[10-1] S. Michizono, *et al*., "Vector-sum control of superconducting RF cavities at STF," PAC'09, Vancouver, May 2009, pp. 2204-2206.
[10-2] C. Nantista and C. Adolphsen, "Klystron Cluster Scheme for ILC High Power RF Distribution," PAC'09, Vancouver, May 2009, pp. 2036-2038.
[10-3] S. Fukuda, *et al*., "Distributed RF Scheme (DRFS) - Newly Proposed HLRF Scheme for ILC," LINAC'10, Tsukuba, 2010, pp. 112-114.
[10-4] T. Miura, *et al*., "Performance of the Micro-TCA Digital Feedback Board for DRFS Test at KEK-STF," these proceedings.
[10-5] E. Negodin: Dose measurements and radiation protection measures for electronics in the XFEL tunnels http://www.xfel.eu/project/meetings/project_meetings/2009/
[10-6] Y. Yamamoto, *et al*., "Test Results of the International S1-Global Cryomodule," SRF2011, Chicago, 2011, THIOA01.

[11-1] http://ilcdoc.linearcollider.org/record/15442/files/TD_Phase_R&D_Report.pdf
[11-2] http://ilcagenda.linearcollider.org/contributionDisplay.py?sessionId=53&contribId=35&confId=2432
[11-3] S. Fukuda, LINAC10, Tsukuba, Sept 2010, MOP013.
[11-4] http://www.linearcollider.org/GDE
[11-5] C. Pagani, *et al*., TESLA Report 2001-36.
[11-6] N. Ohuchi, *et al*., EPAC08, Genoa, Italy, June 2008, MOPP144, p. 892 (2008).
[11-7] B. Aune, *et al*., Phys. Rev. ST-AB, 3(9), Sept. 2000.

[11-8] E. Kako, *et al*., LINAC10, Tsukuba, Japan, Sept 2010, TUP082.
[11-9] N. Ohuchi, *et al*., LINAC10, Tsukuba, Japan, Sept 2010, MO302.
[11-10] https://indico.desy.de/conferenceOtherViews.py?view=standard&confId=3007
[11-11] Y. Yamamoto, *et al*., PAC09, Vancouver, Canada, May 2009, TU5PFP075.
[11-12] W. Schappert, *et al*., SRF11, Chicago, U.S., Jul 2011, FRIOA01, in this conference.

[12-1] S. Michizono, *et al*., "Performance of LLRF System at S1-Global in KEK," IPAC2011, San Sebastián, Spain, MOPC157, pp. 451-453.
[12-2] C. Nantista and C. Adolphsen, "Klystron Cluster Scheme for ILC High Power RF Distribution," PAC'09, Vancouver, May 2009, pp. 2036-2038.
[12-3] STF Group, "STF Phase-1 Activity Report," KEK Report 2009-3, April 2009.
[12-4] "ILC Reference Design Report (RDR)," http://www.linearcollider.org/cms/?pid=1000437

[12-13] http://agenda.infn.it/conferenceOtherViews.py?view=standard&confId=3087

[13-1] S. Fukuda, *et al.,* "Distributed RF scheme (DRFS) – Newly proposed HLRF scheme for ILC," LINAC'10, Tsukuba, Japan (2010) pp. 112-114.
[13-2] T. Miura, *et al*., "Low-Level RF System for curl," IPAC'10, Kyoto, May 2010, TUPEA048.
[13-3] T. Miura, *et al*., "Performance of the µTCA Digital Feedback Board for DRFS Test at KEK-STF," IPAC2011, San Sebastián, Spain, MOPC155.
[13-4] S. Michizono, *et al.,* "Vector-sum Control of Superconducting RF Cavities at STF," PAC'09, Vancouver, BC, CANADA (2009) pp. 2204-2206.